CENTRO DE INVESTIGACIONES
EN OPTICA, A.C.

NOVEL PROPERTIES AND APPLICATIONS OF MECHANICALLY-INDUCED LONG-PERIOD FIBER GRATINGS IN PHOTONIC CRYSTAL FIBERS

By

Daniel Enrique Ceballos Herrera

Submitted in partial fulfillment of
the requirements for the degree of
DOCTOR OF SCIENCES (OPTICS)

PHOTONICS DIVISION,
CENTRO DE INVESTIGACIONES EN ÓPTICA, A.C.
LEÓN, GUANAJUATO, MÉXICO.
NOVEMBER 2009

Supervisor: Dr. Ismael Torres Gómez (CIO)

Examiners: Dr. Norberto Arzate Plata (CIO)
Dr. Yuri Barmenkov (CIO)
Dr. Jesús Arriaga Rodríguez (IFUAP-BUAP)
Dr. Ignacio Flores Llamas (UNAM)

El secreto de la felicidad no es hacer siempre lo que se quiere
sino querer siempre lo que se hace para ayudar a los demás

León Tolstoi

A mi Familia

Table of Contents

List of Figures

List of publications

The following publications were generated during the realization of this PhD project:

1. D. E. Ceballos-Herrera, I. Torres-Gómez, A. Martínez-Rios, G. Anzueto-Sánchez, J. A. Álvarez-Chávez, R. Selvas-Aguilar and J. J. Sánchez-Mondragón, “Ultra widely tunable long period holey fiber grating by the use of mechanical pressure”, Applied Optics, Vol. 46, No. 3, 2007.

2. D. E. Ceballos-Herrera, I. Torres-Gómez, A. Martínez-Rios, and J. J. Sánchez-Mondragón, “Higher-order core mode resonances in a mechanically induced long-period holey fiber grating”, Optical Review, Vol. 16, No. 6, 2009.

3. D. E. Ceballos-Herrera, I. Torres-Gómez, A. Martínez-Rios, and J. J. Sánchez-Mondragón, “Torsion sensing characteristics of mechanically induced long-period holey fiber gratings”, Accepted in IEEE Sensors Journal, 2009.

4. D. E. Ceballos-Herrera, I. Torres-Gómez, A. Martínez-Rios, G. Anzueto-Sanchez, and R. Selvas-Aguilar, “Simultaneous three-wavelength lasing in an Ytterbium-doped fiber laser”, Submitted to Laser Physics, 2009.

5. D. E. Ceballos-Herrera, I. Torres-Gómez, E. Mejía-Beltrán and R. Selvas-Aguilar, “Polarization insensitive mechanically induced tunable long period holey fiber grating”, Procceding of SPIE, Vol. 6422, 2007.

6. D. E. Ceballos-Herrera, I. Torres-Gómez, A. Martínez-Rios, G. Anzueto-Sanchez, J. A. Álvarez-Chávez, R. Selvas-Aguilar and J. J. Sánchez-Mondragón, “A simple, widely tunable band rejection holey fiber filter", 18th International Conference on Optical Fiber Sensor, 2006.

7. I. Torres-Gómez, A. Martínez-Rios, D. E. Ceballos-Herrera, E. Mejía-Beltrán and R. Selvas-Aguilar, "Bandpass filter with adjustable bandwidth based on press induced long period twisted holey fiber grating", Optics Letters, Vol. 33, No. 22, 2007.

8. G. Anzueto-Sanchez, A. Martínez-Rios, I. Torres-Gómez, D. E. Ceballos-Herrera, R. Selvas-Aguilar, and V. Durán-Ramirez, "Tunable Ytterbium Doped Fiber Laser Based on a Mechanically Induced Long Period Fiber Grating", Optical Review, Vol. 14, No. 2, 2007.

9. Miguel-Angel Garcia-March, Albert Ferrando, Mario Zacarés, Sarira Sahu, and Daniel E. Ceballos-Herrera, "Symmetry, winding number and topological charge of vortex solitons in discrete-symmetry media", Physical Review A, Vol. 79, 2009.

10. A. Martínez-Rios, I. Torres-Gómez, R. Selvas-Aguilar, D. E. Ceballos-Herrera, Ruth Mata-Sánchez, and G. Anzueto-Sánchez, "Linear cavity fiber Laser with 100 nm wavelength tuning range", Laser Physics, Vol. 19, No. 5, 2009.

11. A. Ferrando, Yu. P. Bliokh, K. Yu. Bliokh, Mario Zacarés, Carles Milián, and D. E. Ceballos-Herrera, "Soliplasmon excitations at metal/dielectric/Kerr structures", OSA's 93^{RD} annual meeting, Frontiers in Optics, 2009.

Acknowledgements

This section represents the opportunity to express my special gratitude towards people that help me in the realization of this work. There are many people that I would like to thank for their support, generosity and friendship over the past four years. During this time, we shared and enjoyed together many unforgettable experiences. Undoubtedly, they have done of this long walk a beautiful stage in my life.

Firstly, I would like to thank my supervisor, *Dr. Ismael Torres Gómez*, for his guidance and support in the elaboration of this project. I am most grateful, for the confidence and liberty he has given me since my first day at CIO and for his help and advices in many different aspects during all these years. It is a great satisfaction for me to be his first graduate PhD student. Thanks Ismael!.

I would also like to thank *Dr. Alejandro Martínez Rios*, for their guidance, support, and patience when I asked him for his opinions about my work. Also, I highly appreciate the support and guidance of *Dr. Albert Ferrando*, *Dr. Pedro Fernández de Cordoba* and the rest of the group InterTech during my research stay at the Universidad Politécnica de Valencia, Spain. I consider myself very lucky to have worked with them. In the same way, I would like to thank examiners, researches and students that directly or indirectly helped in the improvement of this work.

I would also like to express my warmest gratitude to *Guille*, *Laura* and all members of the academic staff of CIO for the great support they have given to me during all these years.

Also, during my PhD experience I had the opportunity to meet many wonderful people that now are my friends. *Maribel, Diana, Alejandra, Yenisey, Cinthia, Chely, Gilberto,* and *Julio*, I thank them greatly for the beautiful time that we shared, it was amazing!. In the same way, I am highly grateful with *Noé, Jorge, Cristhian, and Memo.* I thank all for their genuine friendship. I am so lucky to have met you.

My family have been a fundamental support to carry my PhD studies off. Their advices and emotional support gave me the necessary patience and serenity to conclude this work. I thank friends from Mérida and Puebla for inspiring and helping me to achieve my goals.

Finally, I would like to thank the Consejo Nacional de Ciencia y Tecnología CONACyT for the doctorate scholarship with number 183106, and all administrative staff of CIO for their help and comprehension.

I thank all those people so much for an exceptional PhD experience!

Daniel Enrique Ceballos Herrera
Centro de Investigaciones en Óptica A. C. (CIO)
December, 2009

Introduction

Optical fibers are a true representative of the remarkable advancements and speed of adoption and commercialization of technology in recent decades. Impulsed by the invention of the laser, in 1960, these waveguide have quickly spread from the scientific laboratories into the everyday life: Internet, medical diagnostics, sensors in food, transport, oil and other industries. The application of fibers allows the possibility of controlling the propagation of light through them. As a consequence, a range of accessories and fiber-based devices have been invented. In special, this work is dedicated to a widely exploited group of fiber devices called long period fiber gratings on a novel kind of fiber: the photonic crystal fiber.

In general, a long period fiber grating (LPFG) is a periodic change in the refractive index profile along the fiber with periods ranging from several tens to several hundreds of microns. The grating modifies the spectral transmission of the light in such a way that different rejection bands in the output spectrum of the fiber are generated. Due to the high sensitivity of these rejection bands on the external parameters of the fiber, LPFGs are suitable for sensing technology, biomedical diagnostics, remote sensing in oil, food and pharmaceutical industry [1].

On the other hand, photonic crystal fibers (PCFs) are a new type of optical fibers composed by a series of air-hole channels distributed in their cross-profile. These types of fibers have represented a revolution in the fiber industry due to the fact that the distribution of air holes provides engineers with new possibilities to manipulate the propagation of light through them and consequently to control and tailor its properties [2, 3]. These air channels can be set in random or in a periodic distribution causing, in both cases, the confinement of electromagnetic waves within the fiber core. Actually, an amazing variety of fibers with air-hole inclusions with different properties have been reported [4, 5].

Additionally, the performance of advanced laser processing and several mechanical methods have allowed the fabrication of LPFGs in practically any kind of fiber with complex index profile. It has allowed the adaptation of the PCF as a new medium for the LPFG fabrication. As a consequence, the different properties of PCFs have given new features to LPFGs, resulting in new possibilities in the design of novel all-fiber devices [6].

In order to fully understand and exploit the potential of LPFGs in PCFs, a theoretical and experimental study of LPFGs with a practical modeling of guided modes in PCFs have to be performed. This is the motivation of this work which is based on previous independent extensive studies of LPFGs [7, 8, 9] and PCFs [2, 3]. Specifically, we study the properties of LPFGs induced mechanically in PCFs. In this work, the chapters are organized in such a way that they follow the principal concepts mentioned above. In Chapter 1, the physical theory of long-period fiber gratings and their fabrication's mechanisms are presented in a detailed way focusing in the mechanical fabrication method. In Chapter 2, a general context about PCFs is presented including a review of the development of PCFs and the description of their principal properties. Furthermore, a description of the numerical methods used to model these kind of fibers is presented focusing principally on the Fast-Fourier-Transform (FFT) mode solver which is performed in this work. Chapter 3 describes new properties of LPFGs obtained as a result of the characterization of different configurations of LPFGs induced mechanically in PCFs. Chapter 4 shows direct applications of these new spectral properties in order to improve the performance of fiber lasers and sensors, and finally, Chapter 5 summarizes all the results obtained and suggests direction for future work.

$\boxed{1}$ Long-period fiber gratings

This Chapter presents the properties and background theory of LPFGs and the methods employed in their fabrication. All these aspects are of great importance to understand this useful fiber optic device. To explain adequately all these points, a brief review of the mathematical concepts and modal properties of fiber optics is discussed before.

1.1 Concepts of fiber optics

First, we consider a step-index fiber geometry as shown in Figure 1.1. As it can be seen, the basic fiber structure is composed by a core, a cladding and the surround of the fiber with refraction indexes n_1, n_2 and n_3 respectively. According to waveguide theory, the following condition $n_1 > n_2 > n_3$ have to be fulfilled in order to allow the propagation of electromagnetic waves by means of total internal reflection [10]. Nevertheless, this condition is not completely necessary in other fiber structures where the physical way to propagate waves is based in photonic bandgaps [11]. We first consider the propagation of waves in fibers using total internal reflection. The fiber scheme is given in both cartesian (x, y, z) and polar (r, ϕ, z) coordinates. The z axis direction runs along the optical fiber. The electromagnetic waves can propagate through the fiber only under certain conditions imposed by the waveguide. These waveguide conditions can be modified varying the structural parameters of the fiber, *i.e.* the core and cladding radius a_1 and a_2, the wavelength λ of the electromagnetic wave, and the value of the refraction index of the core, cladding and surround respectively. These parameters are usually combined to form another useful parameter called *normalized* *frequency* $V = \frac{2\pi a_1}{\lambda}\sqrt{n_1^2 - n_2^2}$. As a result, only a specific number of waves called guided modes can propagate through the fiber. These modes travel to different velocities $v = \frac{2\pi c}{\beta\lambda}$, where c is the light velocity in the vacuum, β is the *effective propagation constant* defined as $\beta = \frac{2\pi n_{eff}}{\lambda}$, and n_{eff} is the effective refraction index of the mode [10, 12]. These modes can be guided into the core or cladding as it is shown in Figure 1.1. According to the value of the V parameter, the fiber can lead the propagation of the fundamental core mode and other higher-order core modes. Specifically, if $V \leq 2.405$ only the fundamental core mode is propagated, and thus the fiber is called *single-mode fiber.* The values of n_{eff} and β for core modes obey the following conditions: $n_1 > n_{eff} > n_2$ and $\frac{2\pi n_1}{\lambda} > \beta > \frac{2\pi n_2}{\lambda}$. The values of n_{eff} and β for higher-order core modes are lower than those for the fundamental core mode. On the other hand, the cladding modes obey the following conditions: $n_2 > n_{eff} > n_3$ and $\frac{2\pi n_2}{\lambda} > \beta > \frac{2\pi n_3}{\lambda}$, and in similar way to core modes, the higher-order cladding modes have lower values of n_{eff} and β that those for the fundamental cladding mode respectively. In the cases where $n_{eff} < n_3$ and $\beta < \frac{2\pi n_3}{\lambda}$, exist a series of modes that do not propagate along the fiber and are dissipated completely in the surround. These modes are called radiated modes [10, 12].

In Figure 1.1 one can observe that core modes are highly confined into the core while the cladding modes are partially confined in the cladding with a portion of their fields in the surround. In consequence, a certain value of their energy radiates to the surround. This is the reason why the cladding modes have higher transmission loss than that for core modes during their propagation. On the other hand, the physical description of the guided modes in an optical fiber can be made by two ways, by tracing rays and solving the wave equation into the waveguide [10, 12]. To describe the propagation of modes in this work, we choose the second one.

Basically, the electromagnetic wave propagation in the fiber lies in the set of Maxwell's equations. As a first approximation, the optical fiber is assumed to consist of a linear, isotropic, homogeneous, lossless dielectric material without any sources such as currents and free charges. Defining $\boldsymbol{E}$ as the electric field vector and $\boldsymbol{D} = \epsilon\boldsymbol{E}$ as the electric

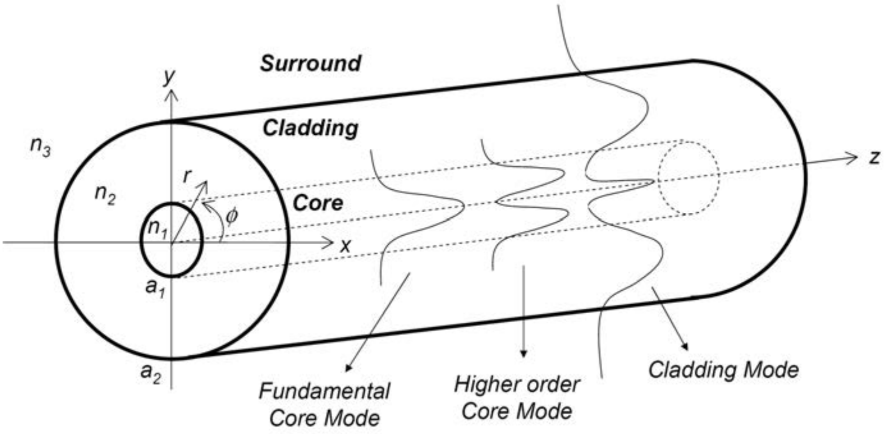

Figure 1.1: Diagram of a cross section of a step-index fiber, showing the coordinate system, the refractive indexes, and the radii of the core a_1 and cladding a_2.

displacement vector (where ϵ is the permittivity defined as $\epsilon = \epsilon_0 n^2$), as well as $\boldsymbol{H}$ the magnetic field vector and $\boldsymbol{B} = \mu \boldsymbol{H}$ the magnetic flux vector (with μ being the permeability with $\mu = \mu_0$), Maxwell's equations appear as follows [10, 12]:

$$\nabla \times \boldsymbol{E} = -\frac{\partial \boldsymbol{B}}{\partial t}, \tag{1.1a}$$

$$\nabla \times \boldsymbol{H} = \frac{\partial \boldsymbol{D}}{\partial t}, \tag{1.1b}$$

$$\nabla \cdot \boldsymbol{D} = 0, \tag{1.1c}$$

$$\nabla \cdot \boldsymbol{B} = 0, \tag{1.1d}$$

where $\boldsymbol{E} = \boldsymbol{E}(r, \phi, z, t)$ and $\boldsymbol{H} = \boldsymbol{H}(r, \phi, z, t)$ respectively. Standard wave equations can be derived from the above expressions in order to study the electromagnetic fields in optical fibers. Particularly, if the refractive index profile does not vary with distance z along the fiber, i.e. $n = n(r, \phi)$, and the electromagnetic wave is a monochromatic wave (with a frequency ω) traveling in the z-direction, the fields $\boldsymbol{E}$ and $\boldsymbol{H}$ can be written in the form:

$$\boldsymbol{E}(r,\phi,z,t)=\boldsymbol{E}(r,\phi)e^{j(\omega t-\beta z)}, \tag{1.2}$$

$$\boldsymbol{H}(r,\phi,z,t)=\boldsymbol{H}(r,\phi)e^{j(\omega t-\beta z)}. \tag{1.3}$$

In these equations, the fields have components in the r, ϕ and z axes, i.e. $\boldsymbol{E}(r,\phi)=E_r(r,\phi)\hat{r}+E_\phi(r,\phi)\hat{\phi}+E_z(r,\phi)\hat{z}$ and $\boldsymbol{H}(r,\phi)=H_r(r,\phi)\hat{r}+H_\phi(r,\phi)\hat{\phi}+H_z(r,\phi)\hat{z}$. These expressions are also valid if we change the coordinates (r,ϕ,z) to (x,y,z). Additionally, if the fiber is axially symmetric (as is usually the case), then the refractive index is only a function of the radial component $n=n(r)$. Now, if we take the curl of equation (1.1)a and substitute equation (1.1)b, we obtain:

$$\nabla\times(\nabla\times\boldsymbol{E})=\epsilon\mu\omega^2\boldsymbol{E}, \tag{1.4}$$

In a similar manner, if we take the curl of equation (1.1)b and substitute equation (1.1)a, we obtain:

$$\nabla\times(\frac{1}{\epsilon(r)}\nabla\times\boldsymbol{H})=(\frac{\omega}{c})^2\boldsymbol{H}. \tag{1.5}$$

Both equations are very important in order to analyze the wave propagation in optical fibers and other types of waveguides. They give a fully vectorial analysis of the electromagnetic waves within the fiber. Also, both equations have field solutions (called eigenvectors of the equation) with ω as the eigenvalue of the solutions. It is important to comment that the numerical solution of one of these equations is sufficient to describe the modal solutions of the waveguide. Nevertheless, the question that arises is which of them is better to solve numerically. In this case, it will depend of the requirements of the modal analysis. Generally, Equation (1.5) is chosen by the majority of researches due to that the magnetic field vector $\boldsymbol{H}$ is not modified when there are high discontinuities in the permittivity profile of the waveguide. In other words, at waveguide boundaries, the tangential components of $\boldsymbol{E}$ and $\boldsymbol{H}$ are continuous although, for their normal components, only $\boldsymbol{H}$ is continuous, while for the normal components of $\boldsymbol{E}$ the following relation must be fulfilled: $n_1 E_1^{normal} = n_2 E_2^{normal}$. This relation is deduced applying the divergence theorem to Equations (1.1)c and (1.1)d respectively [13]. Thus, $\boldsymbol{E}$ will be discontinuous at boundaries and consequently Equation (1.4) could be more difficult to solve in some cases.

If we use the following vectorial relations $\nabla \times \nabla \times \boldsymbol{E} = \nabla(\nabla \cdot \boldsymbol{E}) - \nabla^2 \boldsymbol{E}$ and $\nabla \cdot \boldsymbol{D} = \epsilon_0 \nabla \cdot n^2 \boldsymbol{E} = \epsilon_0 [\nabla n^2 \cdot \boldsymbol{E} + n^2 \nabla \cdot \boldsymbol{E}] = 0$, for equation (1.4), and $\nabla \times (n^{-2} \nabla \times \boldsymbol{H}) = (\nabla n^{-2}) \times \boldsymbol{H} + n^{-2} \nabla \times \nabla \times \boldsymbol{H}$, and $\nabla \cdot \boldsymbol{B} = \nabla \cdot \boldsymbol{H} = 0$, for equation (1.5), we can obtain the following expressions:

$$\nabla^2 \boldsymbol{E} + \nabla(\frac{\nabla n^2}{n^2} \cdot \boldsymbol{E}) + k^2 \boldsymbol{E} = 0, \tag{1.6}$$

$$\nabla^2 \boldsymbol{H} + \frac{\nabla n^2}{n^2} \times (\nabla \times \boldsymbol{H}) + k^2 \boldsymbol{H} = 0. \tag{1.7}$$

These equations are similar to Equations (1.4) and (1.5) but expressed in another way. One can see that $\nabla(\frac{\nabla n^2}{n^2} \cdot \boldsymbol{E})$ and $\frac{\nabla n^2}{n^2} \times (\nabla \times \boldsymbol{H})$ represent the vectorial terms of these equations. If we consider that the refractive index n changes slightly between the core and cladding, n can be considered constant and these terms can be neglected. Then, all components of the fields $\boldsymbol{E}$ and $\boldsymbol{H}$ will be governed by a same equation and not differences of the vectorial composition of the solutions will be obtained, in other words, we will obtain the following scalar wave equation,

$$\nabla^2 \psi + k^2 \psi = 0. \tag{1.8}$$

where ψ can be $\boldsymbol{E}$ or $\boldsymbol{H}$ respectively. This equation is generally called Helmholtz's equation

[10, 12]. In many cases, this approximation is adequate for fibers that do not present a high contrast in their transversal refraction index. In these cases the core field solutions are not highly confined in the fiber core. This restriction is also called weak guidance condition. On the other hand, if we continue in the vectorial regime, and consider that $n(r)$ does not depend of z, and write, $\nabla = \nabla_t + \frac{\partial}{\partial z}$, $\boldsymbol{E} = \boldsymbol{E}_t + E_z\hat{z}$, and $\boldsymbol{H} = \boldsymbol{H}_t + H_z\hat{z}$, we can obtain from equations (1.6) and (1.7) the following equations that govern each component of the fields [12]:

$$\nabla_t^2\boldsymbol{E}_t + \nabla_t(\frac{\nabla_t n^2}{n^2}\cdot\boldsymbol{E}_t) + k^2\boldsymbol{E}_t = \beta^2\boldsymbol{E}_t, \tag{1.9}$$

$$\nabla_t^2\boldsymbol{H}_t + \frac{\nabla_t n^2}{n^2}\times(\nabla_t\times\boldsymbol{H}_t) + k^2\boldsymbol{H}_t = \beta^2\boldsymbol{H}_t, \tag{1.10}$$

$$\nabla_t^2 E_z + i\beta\boldsymbol{E}_t\cdot\frac{\nabla_t n^2}{n^2} + k^2 E_z = \beta^2 E_z, \tag{1.11}$$

$$\nabla_t^2 H_z - (\nabla_t H_z - i\beta\boldsymbol{H}_t)\cdot\frac{\nabla_t n^2}{n^2} + k^2 H_z = \beta^2 H_z, \tag{1.12}$$

where $\boldsymbol{E}_t = E_r\hat{r} + E_\phi\hat{\phi}$ and $\boldsymbol{H}_t = H_r\hat{r} + H_\phi\hat{\phi}$. If we only put attention to Equations (1.9) and (1.10), we can observe that the field solutions of these equations (which correspond to the eigenvectors of the system) have as eigenvalue the propagation constant β. Also, the information of the transversal refraction index profile is transferred to these equations by means of the vectorial terms $\nabla_t(\frac{\nabla_t n^2}{n^2}\cdot\boldsymbol{E}_t)$ and $\frac{\nabla_t n^2}{n^2}\times(\nabla_t\times\boldsymbol{H}_t)$.

To obtain all components of $\boldsymbol{E}$ and $\boldsymbol{H}$ is not necessary to solve each one of Equations (1.9)-(1.12). It is sufficient to solve only for E_z and H_z. It is due to the fact that from Maxwell's equations we can express the transverse fields $\boldsymbol{E}_t$ and $\boldsymbol{H}_t$ in terms of E_z and H_z as follows [12],

$$\boldsymbol{E}_t = \frac{i}{k^2n^2 - \beta^2}\{\beta\nabla_t E_z - (\frac{\mu_0}{\epsilon_0})^{1/2}k\hat{z}\times\nabla_t h_z\}, \tag{1.13}$$

$$\boldsymbol{H}_t = \frac{i}{k^2n^2 - \beta^2}\{\beta\nabla_t H_z - (\frac{\mu_0}{\epsilon_0})^{1/2}kn^2\hat{z}\times\nabla_t E_z\}, \tag{1.14}$$

where $k = \frac{2\pi}{\lambda}$. These equations can be expressed in coordinates (r, ϕ, z) or (x, y, z) using $\nabla_t = \hat{r}\frac{\partial}{\partial r} + \hat{\phi}\frac{1}{r}\frac{\partial}{\partial\phi}$, and $\nabla_t = \hat{x}\frac{\partial}{\partial x} + \hat{y}\frac{\partial}{\partial y}$ respectively.

In general, it is difficult to solve analytically Equations (1.11) and (1.12) for E_z and H_z. So, we have to consider as a first approximation that the variations of n are small and all terms with ∇n^2 are ignored. Additionally, we consider also that the fiber consists of two layers: the core and an infinite cladding. Then, we only can solve the above equations for core fiber modes. For cladding fiber modes one can see Ref. [7]. Now, before to solve these equations, it is important to mention that the guided modes can also be divided according to the following classification [14]: Transversal electric modes (denominated TE modes) with $E_z = 0$, Transversal magnetic modes (denominated TM modes) with $H_z = 0$, and Hybrid modes with $E_z \neq 0$ and $H_z \neq 0$ (denominated HE or EH modes depending if $E_z > H_z$ or $H_z > E_z$ respectively). Then, using equations (1.13) and (1.14), we can obtain that TE modes have the following nonzero components: (E_ϕ, H_r, H_z), the TM modes have the nonzero components: (E_r, E_z, H_ϕ), and the Hybrid modes have all components of $\boldsymbol{E}$ and $\boldsymbol{H}$. Then, if we only solve Equation (1.12) for H_z, we can obtain with the help of Equations (1.13) and (1.14) the following field components of TE modes,

$$\boxed{\begin{array}{ll}
(0 \leq r \leq a_1) & (r > a_1) \\
E_\phi = -j\omega\mu_0\frac{a_1}{u}AJ_1\left(\frac{u}{a_1}r\right) & E_\phi = j\omega\mu_0\frac{a_1}{w}\frac{J_0(u)}{K_0(w)}AK_1\left(\frac{w}{a_1}r\right) \\
H_r = j\beta\frac{a_1}{u}AJ_1\left(\frac{u}{a_1}r\right) & H_r = -j\beta\frac{a_1}{w}\frac{J_0(u)}{K_0(w)}AK_1\left(\frac{w}{a_1}r\right) \\
H_z = AJ_0\left(\frac{u}{a_1}r\right) & H_z = \frac{J_0(u)}{K_0(w)}AK_0\left(\frac{w}{a_1}r\right)
\end{array}} \tag{1.15}$$

where $\omega = ck$, $u = a_1\sqrt{k^2n_1^2 - \beta^2}$, $w = a_1\sqrt{\beta^2 - k^2n_2^2}$ and A is a normalization constant.

These solutions fulfill the boundary conditions at $r = a_1$. In this case H_z and E_ϕ must be continuous. From these boundary conditions, we can obtain the following equation,

$$\frac{J_1(u)}{uJ_0(u)} = -\frac{K_1(w)}{wK_0(w)}. \tag{1.16}$$

In the same manner, if we solve Equation (1.11) for E_z, we can obtain for TM modes,

$$\boxed{\begin{array}{ll} (0 \leq r \leq a_1) & (r > a_1) \\ E_r = -j\beta \frac{a_1}{u} AJ_1\left(\frac{u}{a_1}r\right) & E_r = -j\beta \frac{a_1}{w} \frac{J_0(u)}{K_0(w)} AK_1\left(\frac{w}{a_1}r\right) \\ E_z = AJ_0\left(\frac{u}{a_1}r\right) & E_z = \frac{J_0(u)}{K_0(w)} AK_0\left(\frac{w}{a_1}r\right) \\ H_\phi = j\omega\epsilon_0 n_1^2 AJ_1\left(\frac{u}{a_1}r\right) & H_\phi = -j\omega\epsilon_0 n_2^2 \frac{J_0(u)}{K_0(w)} AK_1\left(\frac{w}{a_1}r\right) \end{array}} \tag{1.17}$$

These solutions also fulfill the boundary conditions at $r = a_1$. In this case, E_z and H_ϕ are continuous. From these boundary conditions we can obtain,

$$\frac{J_1(u)}{uJ_0(u)} = -\left(\frac{n_2}{n_1}\right)^2 \frac{K_1(w)}{wK_0(w)}. \tag{1.18}$$

If we solve both Equations (1.11) and (1.12) for E_z and H_z and using again Equations (1.13) and (1.14), we obtain for hybrid modes,

$$\boxed{\begin{array}{l} (0 \leq r \leq a_1) \\ E_r = -\frac{ja_1^2}{u^2}\left[A\beta \frac{u}{a_1} J_l'\left(\frac{u}{a_1}r\right) + C\omega\mu_0 \frac{l}{r} J_l\left(\frac{u}{a_1}r\right)\right] cos\,(l\theta + \psi) \\ E_\phi = -\frac{ja_1^2}{u^2}\left[-A\beta \frac{l}{r} J_l\left(\frac{u}{a_1}r\right) - C\omega\mu_0 \frac{u}{a_1} J_l'\left(\frac{u}{a_1}r\right)\right] sin\,(l\theta + \psi) \\ E_z = AJ_l\left(\frac{u}{a_1}r\right) cos\,(l\theta + \psi) \\ H_r = -\frac{ja_1^2}{u^2}\left[A\omega\epsilon_0 n_1^2 \frac{l}{r} J_l\left(\frac{u}{a_1}r\right) + C\beta \frac{u}{a_1} J_l'\left(\frac{u}{a_1}r\right)\right] sin\,(l\theta + \psi) \\ H_\phi = -\frac{ja_1^2}{u^2}\left[A\omega\epsilon_0 n_1^2 \frac{u}{a_1} J_l'\left(\frac{u}{a_1}r\right) + C\beta \frac{l}{r} J_l\left(\frac{u}{a_1}r\right)\right] cos\,(l\theta + \psi) \\ H_z = CJ_l\left(\frac{u}{a_1}r\right) sin\,(l\theta + \psi) \end{array}} \tag{1.19}$$

$$\boxed{\begin{array}{l}
(r > a_1) \\
E_r = \frac{ja_1^2}{w^2}\left[A\beta\frac{w}{a_1}K_l'\left(\frac{w}{a_1}r\right) + C\omega\mu_0\frac{l}{r}K_l\left(\frac{w}{a_1}r\right)\right]\frac{J_l(u)}{K_l(w)}cos\,(l\theta+\psi) \\
E_\phi = \frac{ja_1^2}{w^2}\left[-A\beta\frac{l}{r}K_l\left(\frac{w}{a_1}r\right) - C\omega\mu_0\frac{w}{a_1}K_l'\left(\frac{w}{a_1}r\right)\right]\frac{J_l(u)}{K_l(w)}sin\,(l\theta+\psi) \\
E_z = A\frac{J_l(u)}{K_l(w)}K_l\left(\frac{w}{a_1}r\right)cos\,(l\theta+\psi) \\
H_r = \frac{ja_1^2}{w^2}\left[A\omega\epsilon_0 n_2^2\frac{l}{r}K_l\left(\frac{w}{a_1}r\right) + C\beta\frac{w}{a_1}K_l'\left(\frac{w}{a_1}r\right)\right]\frac{J_l(u)}{K_l(w)}sin\,(l\theta+\psi) \\
H_\phi = \frac{ja_1^2}{w^2}\left[A\omega\epsilon_0 n_2^2\frac{w}{a_1}K_l'\left(\frac{w}{a_1}r\right) + C\beta\frac{l}{r}K_l\left(\frac{w}{a_1}r\right)\right]\frac{J_l(u)}{K_l(w)}cos\,(l\theta+\psi) \\
H_z = C\frac{J_l(u)}{K_l(w)}K_l\left(\frac{w}{a_1}r\right)sin\,(l\theta+\psi)
\end{array}} \tag{1.20}$$

where l is the order of the Bessel functions and C is a normalization constant respectively. These solutions fulfill the boundary conditions at $r = a_1$. E_ϕ and H_ϕ are continuous and from these conditions we can obtain the following equation,

$$\left[\frac{J_n'(u)}{uJ_n(u)} + \frac{K_n'(w)}{wK_n(w)}\right]\left[\frac{J_n'(u)}{uJ_n(u)} + \left(\frac{n_2}{n_1}\right)^2\frac{K_n'(w)}{wK_n(w)}\right] = n^2\left(\frac{1}{u^2}+\frac{1}{w^2}\right)\left[\frac{1}{u^2} + \left(\frac{n_2}{n_1}\right)^2\frac{1}{w^2}\right]. \tag{1.21}$$

Equations (1.16), (1.18) and (1.21) are very important because they govern the eigenvalues of the guided modes in a fiber. In other words, with these eigenvalue equations, we can obtain the values of the propagation constant β of the modes. The solution of these equations give as a result the curves shown in Figure 1.2, where the propagation constant β as a function of the normalized frequency V for some core modes is plotted. The first curve which correspond to lower values of the normalized frequency V represents the fundamental core mode HE_{11}. As was mentioned above, if $V \leq 2.405$ only the curve for the fundamental mode obey the eigenvalue equation for Hybrid modes and only this mode is propagated into the fiber. For values of $V > 2.405$ other curves can be obtained for higher order core modes: three almost degenerated (TE_{01}, HE_{21}, TM_{01}), other three almost degenerated (EH_{11}, HE_{31}, EH_{12}), and so on. It means that all these modes can be guided through the fiber simultaneously. As example, in Figure (1.3), it is shown the intensity distribution of the first HE_{11}, TE_{01}, and TM_{01} modes.

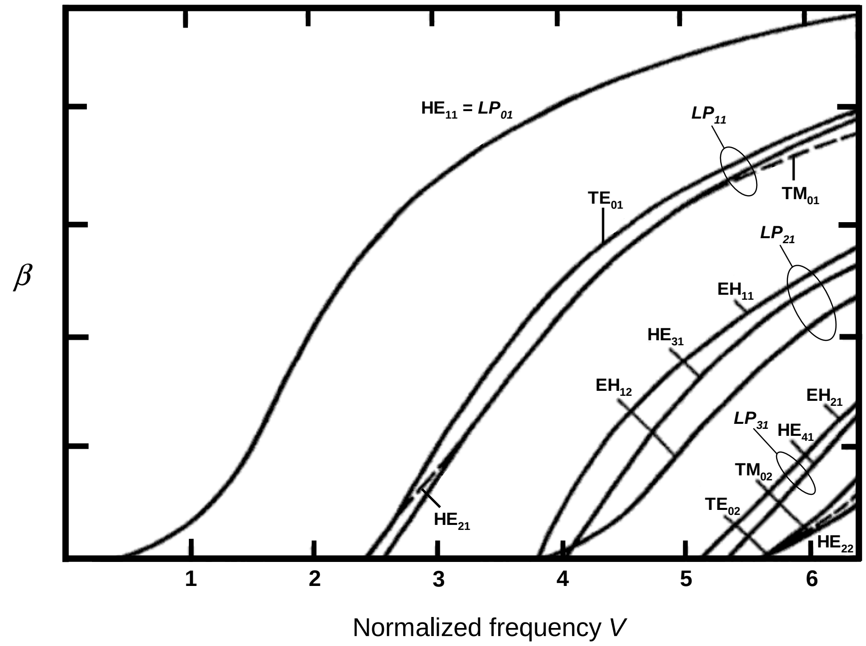

Figure 1.2: Plots of the propagation constant β as a function of normalized frequency V for some guided core modes.

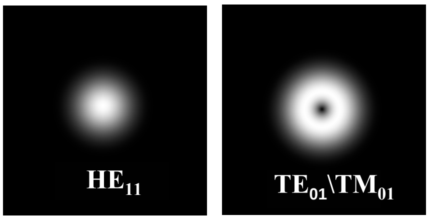

Figure 1.3: Qualitative representation of the intensity distribution of the first HE_{11}, TE_{01}, and TM_{01} modes according to Ref. [12].

In principle, if we consider that the refraction index profile of the fiber changes slightly, *i.e.* $n_1 \simeq n_2$ (as it was made at the beginning of the analytical solution of E_z and H_z), the higher-order core modes are almost degenerated, but if we apply this approximation again in Equations (1.16), (1.18) and (1.21), we can obtain the following unified eigenvalue equation:

$$\frac{J_m(u)}{uJ_{m-1}(u)} = -\frac{K_m(w)}{wK_{m-1}(w)}, \tag{1.22}$$

where $m = 1$ for TE and TM modes, $m = l + 1$ for EH modes, and $m = l - 1$ for HE modes being l an integer number with $l \geq 1$ respectively. In this case, the guided modes mentioned above are completely degenerated and form a new mode classification denominated LP guided modes. These LP modes are also indicated in Figure 1.2. In this figure we can observe that the first LP mode called fundamental mode is formed by $LP_{01} = HE_{11}$, while the higher core modes are formed by $LP_{11} = TE_{01} + TM_{01} + HE_{21}$, $LP_{21} = EH_{11} + HE_{31} + EH_{12}$, etc. In particular, LP modes only have transversal components. i.e. only have components in (r,ϕ) or (x,y) coordinates [10, 12]. The above characteristic can be deduced if one take the relative magnitude between the longitudinal and transversal components of the fields defined in Equations (1.15), (1.17), and (1.19) with the condition $n_1 \simeq n_2$. This condition allows the LP modes to travel along the fiber with transversal components of the field $\boldsymbol{E}$ or $\boldsymbol{H}$ forming always a transversal vector during its propagation. The direction of the field vector is called polarization of the field [10, 12]. Specifically, for LP modes, the polarization is linear during their propagation in an optical fiber with circular core. From this, one can infer that the LP-mode means *linearly polarized mode*.

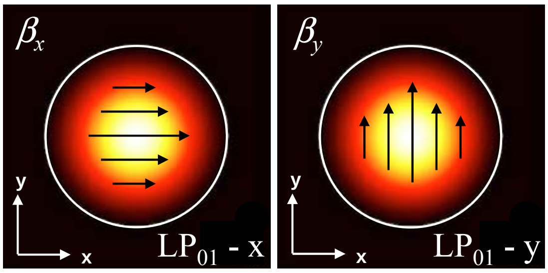

Figure 1.4: Intensity distribution and direction of the transversal components of the LP_{01} fundamental core mode.

In Figure 1.4 we can observe the intensity distribution of the electric field $\boldsymbol{E}$ for the fundamental core mode LP_{01}. As it is mentioned above, $\boldsymbol{E}$ only has transversal vectorial components in x and y directions. The vectorial components are also shown in Figure 1.4 with arrows. In theory, if the fiber core is perfectly circular and the transversal refractive index of the core is homogeneous, the propagation constant of each transversal component called β_x and β_y will be the same. In consequence the difference $\Delta\beta = \beta_x - \beta_y \simeq 0$. In the literature $\Delta\beta$ is denominated modal birefringence and it is nonzero for inhomogeneous or elliptic transversal refractive index of the core [10, 12]. Figure 1.5 shows the intensity distribution of $\boldsymbol{E}$ for the first higher-order core mode LP_{11}. In the same way, the direction of its vectorial components are shown with arrows. It is worth to mention that for LP_{11} modes, we can distinguish two groups or intensity distributions. Both groups called **1** and **2** are shown in each row of Figure 1.5. Again, if the fiber is perfectly circular, both groups will be degenerated. It is easy to observe that if we rotate the intensity distribution of group **1**, it will coincide with group **2**. Additionally, each group has a modal birefringence $\Delta\beta$ which is the same for perfect circular fiber cores.

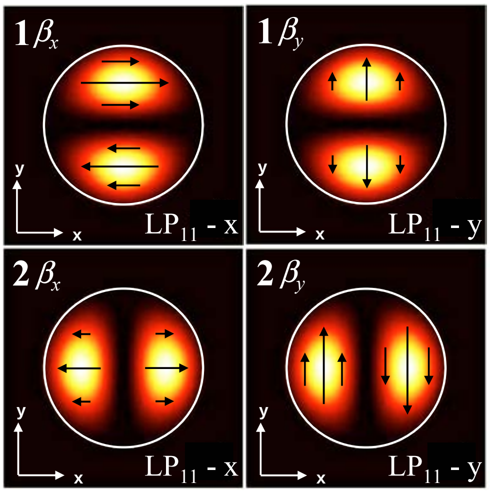

Figure 1.5: Intensity distribution and direction of the transversal components of the LP_{11} core mode.

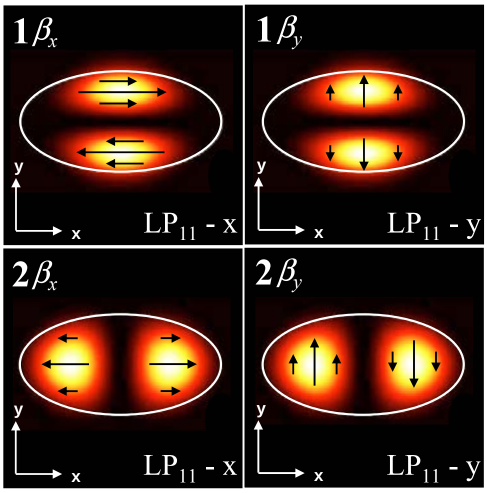

Figure 1.6: Intensity distribution and direction of the transversal components of the LP_{11} core mode in an elliptical core.

Finally, if we consider fibers with an elliptical core, there can be two orientations for the field configuration of the LP_{11} mode. This behavior can be observed in Figure 1.6, where in one can identify that there are also two different groups of intensity distributions called again groups **1** and **2**. Due to the fact that these groups are not degenerated (unlike the circular core case), the LP_{11} mode split into odd (group **1**) and even (group **2**) LP_{11} modes respectively [14, 15]. The odd and even LP_{11} modes have significantly different modal birefringence. This behavior can also be seen in other modes like the fundamental LP_{01} core mode. The elliptical core fibers that support two stable special modes, the LP_{01} and LP_{11} (even/odd) modes, are called elliptical core two-mode fibers [14]. It is worth mentioning that these characteristics described above for core modes are also applied to cladding modes but with different mathematical expressions. In order to obtain the components of the fields $\boldsymbol{E}$ and $\boldsymbol{H}$ for cladding modes, one has to solve again Equations (1.11) and (1.12) and apply the boundary conditions for a three-layer structure [7, 16].

1.2 Long-period fiber grating theory

A long-period fiber grating (LPFG) consist of a periodic perturbation of the refraction index of the fiber core that couples energy between two co-propagating modes, typically the fundamental core mode and a higher-order mode of the core or cladding respectively. The coupling between these modes must satisfy the following phase matching condition [8, 9],

$$\lambda_{res} = (n^1_{eff} - n^2_{eff})\Lambda, \tag{1.23}$$

where λ_{res} is the resonance wavelength, n^1_{eff} and n^2_{eff} are the effective indexes of the core and cladding modes, and Λ is the grating period. Generally, the value of Λ is found to be within the range of 100 μm to 1 mm. A pictorial representation of this coupling can be observed in Figure 1.7. In this figure one can observe that the fundamental core mode transfers its energy to a cladding mode with higher transmission loss. The high attenuation of the cladding modes results in the transmission spectrum of the fiber with a series of attenuation bands centered at discrete wavelengths determined by the phase matching condition. An example of a typical LPFG transmission spectra is shown in Figure 1.8. As can be seen, each attenuation band correspond to the coupling of the core mode to different cladding modes. The exact form of the spectrum, and the center wavelengths of the attenuation bands, are sensitive to the period and length of the LPFG (typically of the order of 30 mm) and to the local environment: temperature, strain, bend radius and to the refractive index of the medium surrounding the fiber [17]. Changes in these parameters can modify the period of the LPFG and/or the differential refractive index of the core and cladding modes, as a consequence, the phase matching condition is modified resulting in a change in the central wavelengths of the attenuation bands.

As it is mentioned above, the phase matching condition is an necessary requirement in the mode coupling of a LPFG. Therefore, its deduction is presented in this work. First, let us consider without loss of generality the weak guiding condition. In this case, the propagation of modes can be described using the scalar wave equation given in Equation

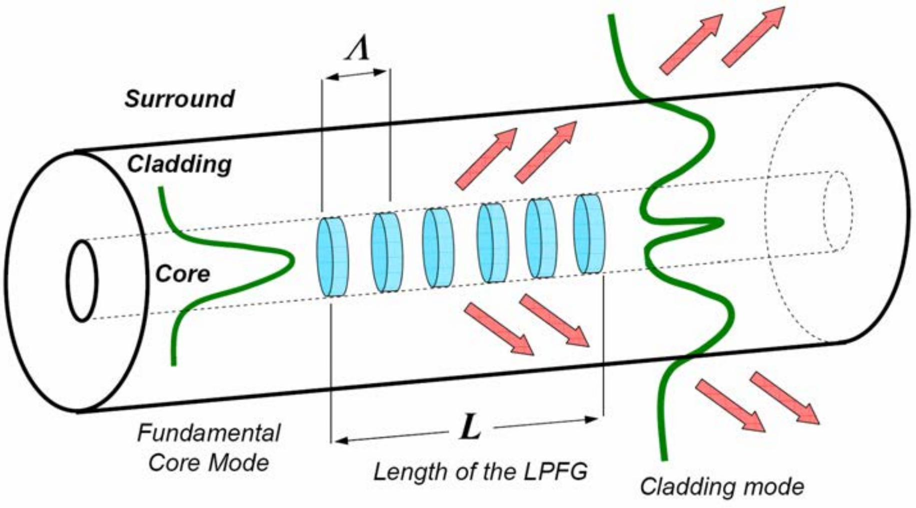

Figure 1.7: Mode coupling between the fundamental core mode and a cladding mode using a LPFG.

(1.8). Also, we consider an optical fiber with a refractive index profile $n^2(x,y)$ in which there is a periodic z-dependent perturbation given by,

$$\Delta n^2(x,y,z) = \Delta n^2(x,y)\sin(Kz), \tag{1.24}$$

where $K = \frac{2\pi}{\Lambda}$. This perturbation corresponds to the periodic index variation of the fiber core in a LPFG. If ψ_1 and ψ_2 are two modes of the fiber, then the periodic perturbation can, under certain conditions couple energy among them. Thus, we can write the total field at any value of z as,

$$\psi(x,y,z) = \psi_1 + \psi_2 = A(z)\psi_1(x,y)e^{-is_1\beta_1 z} + B(z)\psi_2(x,y)e^{-is_2\beta_2 z}, \tag{1.25}$$

where $s_1 = \pm 1$ and $s_2 = \pm 1$ respectively. If s_1 and s_2 have the same sign, we are describing two modes propagating along the same direction. If s_1 and s_2 have different signs, the modes are propagating in opposite directions. Therefore, we are interested in the first case. From Equation (1.25) we can distinguish that the amplitudes A and B depend on the

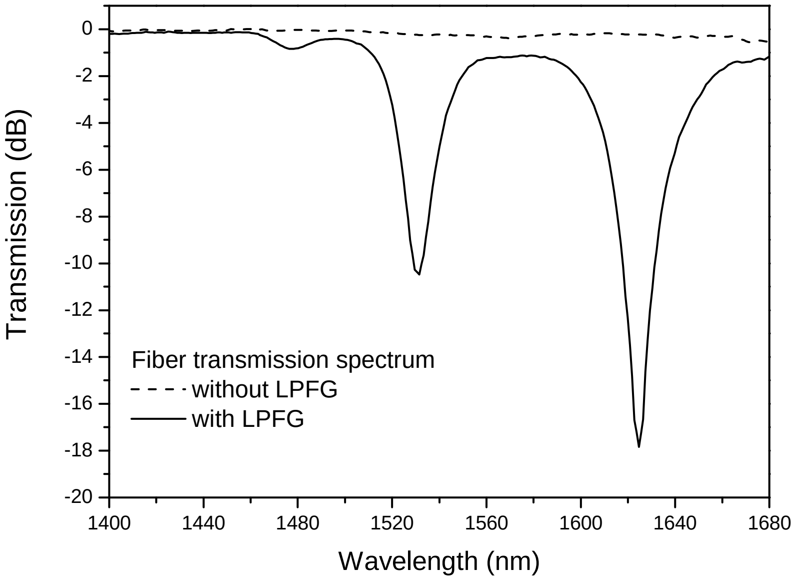

Figure 1.8: Transmission spectra of a typical LPG induced in a commercial single-mode fiber, SMF28, with a period $\Lambda = 500$ μm, and length $L = 30$ mm.

propagation length z. This characteristic can be understood if we consider that the energy of ψ_1 is transferred to ψ_2 during their propagation along the perturbed core. Then, their amplitudes have to vary in order to allow this transference. In the absence of perturbation, A and B would be constants, and the following scalar wave equations are satisfied,

$$\nabla_t^2 \psi_1 + (k^2 n^2(x,y) - \beta_1^2)\psi_1 = 0, \tag{1.26}$$

$$\nabla_t^2 \psi_2 + (k^2 n^2(x,y) - \beta_2^2)\psi_2 = 0. \tag{1.27}$$

On the other hand, the wave equation to be satisfied by the total field $\psi(x,y,z)$ is,

$$\nabla_t^2 \psi + \frac{d^2\psi}{dz^2} + k^2[n^2(x,y) + \Delta n^2(x,y)\sin(Kz)]\psi = 0, \tag{1.28}$$

where we can observe that the refractive index perturbation is added to the wave equation respectively. Substituting Equation (1.25) for ψ in Equation (1.28) and reordering terms, we obtain,

$$
\begin{aligned}
&(\nabla_t^2\psi_1 + [k^2n^2(x,y) - \beta_1^2]\psi_1)A(z)e^{-is_1\beta_1 z} + \frac{d^2A}{dz^2}\psi_1 e^{-is_1\beta_1 z}\\
&-2i\beta_1 s_1\frac{dA}{dz}\psi_1 e^{-is_1\beta_1 z} + k^2[\Delta n^2(x,y)sin(Kz)]\psi_1 e^{-is_1\beta_1 z}\\
&+(\nabla_t^2\psi_2 + [k^2n^2(x,y) - \beta_2^2]\psi_2)B(z)e^{-is_2\beta_2 z} + \frac{d^2B}{dz^2}\psi_2 e^{-is_2\beta_2 z}\\
&-2i\beta_2 s_2\frac{dB}{dz}\psi_2 e^{-is_2\beta_2 z} + k^2[\Delta n^2(x,y)sin(Kz)]\psi_2 e^{-is_2\beta_2 z} = 0.
\end{aligned} \tag{1.29}
$$

If we neglect the second derivative of A and B with respect to z (also referred to as the slowly varying envelope approximation) and using Equations (1.26) and (1.27), we get,

$$
-2i\beta_1 s_1\frac{dA}{dz}\psi_1 - 2i\beta_2 s_2\frac{dB}{dz}\psi_2 e^{-i\Delta\beta z} + k^2[\Delta n^2(x,y)\sin(Kz)][A\psi_1 + B\psi_2 e^{-i\Delta\beta z}] = 0, \tag{1.30}
$$

where $\Delta\beta = s_1\beta_1 - s_2\beta_2$. Now, let us consider the orthogonality condition for ψ_1 and ψ_2 given by [12],

$$
\int_{-\infty}^{\infty}\int_{-\infty}^{\infty}\psi_1^*(x,y)\psi_2(x,y)dxdy = 0. \tag{1.31}
$$

This condition indicates that both modes ψ_1 and ψ_2 are linearly independents. In other words, ψ_1 and ψ_2 have different propagation constants. The details of this condition can be found in Refs. [10, 12]. Then, if we multiple Equation (1.30) by ψ_1^* and integrate with respect to x and y, we can get (considering the orthogonal condition) that,

$$\frac{dA}{dz} = -i\kappa_{11}\frac{A}{s_1}\sin(Kz) - \kappa_{12}\frac{B}{s_1}\left[e^{i(\Delta\beta+K)z} - e^{i(\Delta\beta-K)z}\right], \tag{1.32}$$

where,

$$\kappa_{11} = \frac{k^2}{2\beta_1}\frac{\int\int \psi_1^*\Delta n^2\psi_1 dxdy}{\int\int \psi_1^*\psi_1 dxdy}, \tag{1.33}$$

$$\kappa_{12} = \frac{k^2}{2\beta_1}\frac{\int\int \psi_1^*\Delta n^2\psi_2 dxdy}{\int\int \psi_1^*\psi_2 dxdy}. \tag{1.34}$$

In the same manner, if we multiply Equation (1.30) by ψ_2^* and integrate, we obtain,

$$\frac{dB}{dz} = -i\kappa_{22}\frac{B}{s_2}\sin(Kz) + \kappa_{21}\frac{A}{s_2}\left[e^{-i(\Delta\beta+K)z} - e^{-i(\Delta\beta-K)z}\right], \tag{1.35}$$

with,

$$\kappa_{22} = \frac{k^2}{2\beta_2}\frac{\int\int \psi_2^*\Delta n^2\psi_2 dxdy}{\int\int \psi_2^*\psi_2 dxdy}, \tag{1.36}$$

$$\kappa_{21} = \frac{k^2}{2\beta_2}\frac{\int\int \psi_2^*\Delta n^2\psi_1 dxdy}{\int\int \psi_2^*\psi_1 dxdy}. \tag{1.37}$$

At this point, we have to analyze carefully both Equations (1.32) and (1.35). For example, if we integrate both equations over a small distance, $L = L_2 - L_1$, compared with the distance over which A and B change appreciably, we can obtain the following approximations,

$$\Delta A = i\kappa_{11}\frac{A}{s_1}\left[\frac{\cos(Kz)}{K}\right]_{L_1}^{L_2} + i\kappa_{12}\frac{B}{s_1}\left[\frac{e^{i(\Delta\beta+K)z}}{(\Delta\beta+K)}\right]_{L_1}^{L_2} - i\kappa_{12}\frac{B}{s_1}\left[\frac{e^{i(\Delta\beta-K)z}}{(\Delta\beta-K)}\right]_{L_1}^{L_2}, \tag{1.38}$$

$$\Delta B = i\kappa_{22}\frac{B}{s_2}\left[\frac{\cos(Kz)}{K}\right]_{L_1}^{L_2} + i\kappa_{21}\frac{A}{s_2}\left[\frac{e^{-i(\Delta\beta+K)z}}{(\Delta\beta+K)}\right]_{L_1}^{L_2} - i\kappa_{21}\frac{A}{s_2}\left[\frac{e^{-i(\Delta\beta-K)z}}{(\Delta\beta-K)}\right]_{L_1}^{L_2}. \quad (1.39)$$

In these equations, we can observe that if $\Delta\beta - K \simeq 0$, the contributions of the first and second terms in the right side of both equations are negligible compared with the last term, and hence, can be neglected. Thus, Equations (1.32) and (1.35) can be written as follows,

$$\frac{dA}{dz} = \kappa_{12}\frac{B}{s_1}e^{i(\Delta\beta-K)z}, \quad (1.40)$$

$$\frac{dB}{dz} = -\kappa_{21}\frac{A}{s_2}e^{-i(\Delta\beta-K)z}. \quad (1.41)$$

If we use the condition $\Delta\beta = K$, we obtain,

$$\frac{dA}{dz} = \kappa_{12}\frac{B}{s_1}, \quad (1.42)$$

$$\frac{dB}{dz} = -\kappa_{21}\frac{A}{s_2}. \quad (1.43)$$

Both Equations (1.42) and (1.43) are very important because they describe the coupling between two modes under the phase matching condition $\Delta\beta = K$, where $K = \frac{2\pi}{\Lambda}$, and $\Delta\beta = s_1\beta_1 - s_2\beta_2$ respectively. If we choose $s_1 = s_2 = 1$, we describe the coupling between two co-propagating modes. Then, equations (1.40) and (1.41) describe the mode coupling in a LPFG. The value of $\Delta\beta$ is determined as follows,

$$\Delta\beta = \frac{2\pi}{\lambda}(n_1^{eff} - n_2^{eff}). \quad (1.44)$$

Typically, the values of n_1^{eff} and n_2^{eff} in optical fibers are very close. For example, in single mode fibers, $\Delta n^{eff} = n_1^{eff} - n_2^{eff}$ has values from 0.001 to 0.01 at $\lambda = 1.5\mu m$ [10]. Then, $\Delta\beta$ has values from 0.004 up to 0.04 μm^{-1}. If we consider the phase matching condition for co-propagating modes, $\Delta\beta = \frac{2\pi}{\Lambda}$, and use the typical values of $\Delta\beta$, we can deduce that the period Λ has values in the range of 100 to 1000 μm respectively, which is characteristic in LPFGs.

On the other hand, if we chose $s_1 = 1$ and $s_2 = -1$, we describe the coupling between two modes propagating in opposite directions. Then, Equations (1.42) and (1.43) describe another type of mode coupling given in devices called fiber bragg gratings (FBGs) [8, 9]. These gratings couple energy from the fundamental core mode to a higher-order mode of the core or cladding propagating in opposite direction along the fiber. These kind of gratings share the same characteristics of LPFGs except for the following cases: first, as it was mentioned above, the energy transferred to the coupled mode is reflected, instead of being propagated in the same direction of the fundamental core mode; and second, the value of the period Λ for FBGs has values lower than 1 μm. This last characteristic can be deduced again from the phase matching condition $\Delta\beta = \beta_1 + \beta_2 = K$, with $K = \frac{2\pi}{\Lambda}$. Typically, the value of β in single mode fibers is ~ 6 μm^{-1} [10]. If we consider $\beta_1 \sim \beta_2 = \beta$, then $2\beta = \frac{2\pi}{\Lambda}$, and consequently $\Lambda \sim 0.5\mu m$, which is into the range mentioned above for FBGs respectively. For more information about FBGs, one can revise Refs. [8, 9].

On the other hand, Equations (1.40) and (1.41) for co-propagating modes correspond to the general case where the condition of phase matching is not completely fulfilled. The solution of these equations is given in the following way: considering $\kappa_{12} \simeq \kappa_{21}$ (which is valid in the weak guiding condition), differentiating Equation (1.41) with respect to z, and using Equation (1.40) to eliminate A, we can obtain,

$$\frac{d^2B}{dz^2} + i\Gamma\frac{dB}{dz} + \kappa^2 B = 0, \tag{1.45}$$

where $\Gamma = \Delta\beta - K$. The solution of Equation (1.45) is,

$$B(z) = e^{-i\Gamma z/2}\left[b_1 e^{i\gamma z} + b_2 e^{-i\gamma z}\right], \tag{1.46}$$

where $\gamma^2 = \kappa^2 + \frac{\Gamma^2}{4}$, and both b_1 and b_2 are constants. Substituting the solution $B(z)$ in Equation (1.40), we obtain,

$$A(z) = \frac{i}{\kappa} e^{i\Gamma z/2}\left[\left(\frac{\Gamma}{2} - \gamma\right) b_1 e^{i\gamma z} + \left(\frac{\Gamma}{2} + \gamma\right) b_2 e^{-i\gamma z}\right]. \tag{1.47}$$

The constants b_1 and b_2 are determined by the initial conditions at $z = 0$. These are: $A(z = 0) = 1$, and $B(z = 0) = 0$. In this way, we can obtain $b_1 = -b_2$ respectively. Then,

$$B(z) = -\frac{\kappa}{\gamma} e^{-i\Gamma z/2}\sin(\gamma z), \tag{1.48}$$

$$A(z) = e^{i\Gamma z/2}\left[cos(\gamma z) - i\frac{\Gamma}{2\gamma}\sin(\gamma z)\right]. \tag{1.49}$$

Thus, the power corresponding to modes 1 and 2 at any value of z is,

$$P_1(z) = |A(z)|^2 = cos^2(\gamma z) + \frac{\Gamma^2}{4\gamma^2}\sin^2(\gamma z), \tag{1.50}$$

$$P_2(z) = |B(z)|^2 = \frac{\kappa^2}{\gamma^2}\sin^2(\gamma z). \tag{1.51}$$

Equations (1.50) and (1.51) describe the power variation of both modes with z. From Equation (1.51) we notice that the maximum value of P_2 is $\frac{\kappa^2}{\gamma^2}$. This value is equal to unity only when $\gamma = \kappa$ (that is, $\Gamma = 0$). Then, complete power transfer is possible only if the phase matching condition is fulfilled, *i.e.* $\Gamma = 0$. Figure (1.9) gives the variation of P_2 with Γ. In this case z is chosen adequately in order to obtain the maximum value of $\sin(\gamma z)$ with $\Gamma = 0$. Then, $z = L = \frac{\pi}{2\kappa}$. In this figure we can observe how the power has a global maximum at $\Gamma = 0$ and has lower values at $\Gamma \neq 0$. Due to this characteristic, Γ is usually denominated the *detuning parameter* of the coupled modes [18]. Also, it is very interesting to observe that the value of $L = \frac{\pi}{2\kappa}$ represents the ideal length of perturbation along z to obtain the maximum coupling between both modes. Then, the length of LPFGs have to be a multiple integer of this value.

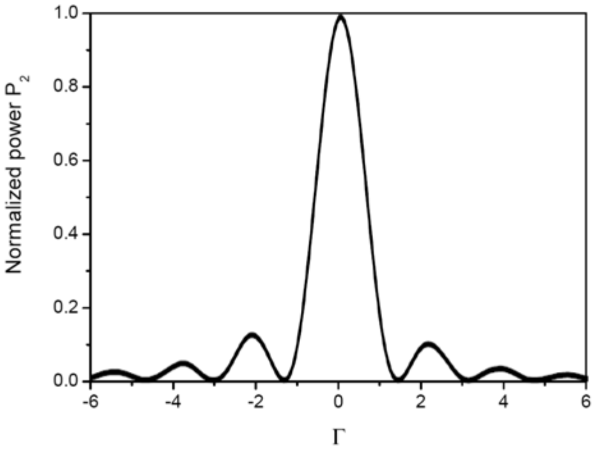

Figure 1.9: Plot of the normalized power, P_2, as a function of the detuning parameter, Γ. The length of the grating is chosen to be ideal, $L = \frac{\pi}{2\kappa}$.

On the other hand, Equation (1.51) can also be expressed in terms of λ. If we consider again that $\gamma^2 = \kappa^2 + \frac{\Gamma^2}{4}$, $\kappa = \kappa(\lambda)$, $\Gamma = \Gamma(\lambda)$, and $z = L$. Then, we have,

$$P_2(\lambda) = \frac{\kappa^2(\lambda)}{\kappa^2(\lambda) + \Gamma^2(\lambda)/4} \sin^2 \left[\sqrt{\frac{\kappa^2(\lambda) + \Gamma^2(\lambda)/4}{\kappa^2(\lambda)}} \frac{\pi}{2} \right]. \tag{1.52}$$

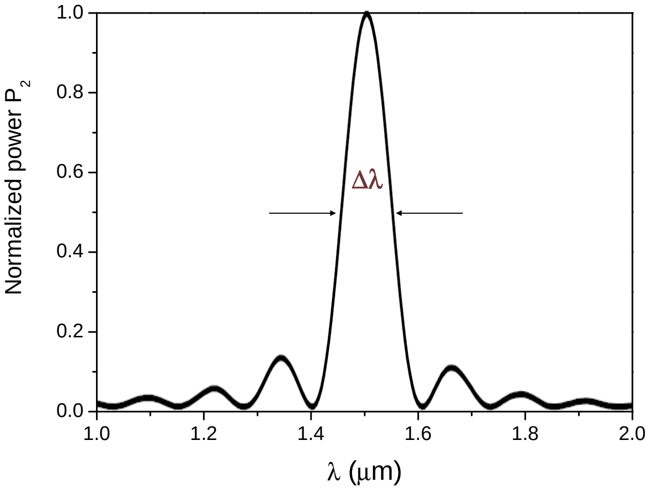

Figure 1.10: Plot of the normalized power, P_2, as a function of wavelength, λ. The length of the grating is chosen to be ideal, $L = \frac{\pi}{2\kappa}$.

Figure (1.10) shows the plot of P_2 as a function of λ. We can see that this figure has a curve with similar form than that shown in Figure (1.9). It is important to comment that the plot of P_1 as a function of λ can be obtained using Equation 1.50, and it has similar form as Figure (1.8). The importance of expressing P_2 in terms of λ is found in the fact that one can obtain the bandwidth $\Delta\lambda$ of the mode coupling as it is indicated in Figure (1.10). Generally, the bandwidth is defined as the full width at half maximum (FWHM) of the power spectrum of Equation (1.52). In this case, we have to know the maximum and the half maximum values of P_2 in order to determine $\Delta\lambda$. According to this procedure, the bandwidth can be approximated as follows [10, 18],

$$\Delta\lambda = \frac{0.8\Lambda\lambda}{L} \tag{1.53}$$

In this equation, we can observe that the bandwidth decreases with L and depends directly on the grating period Λ, and the central wavelength λ for the maximum value of P_2. This expression is also very interesting because it allows the design of LPFG spectrums modifying the L, Λ, and λ parameters respectively.

Another way to modify the LPFG spectra is changing the periodicity of the longitudinal perturbation. For example, we can add a specific kind of chirp in the periodical perturbation of the grating [8, 9]. As a result, depending on the chirp, the spectrum of Figure (1.10) can broad or can be apodized eliminating the fluctuations observed at both sides. To describe mathematically this perturbation, we have to rewrite $\Delta n(x, y, z) = \Delta n(x, y) \sin [Kz + \delta(z)]$, where $\delta(z)$ represents the phase change introduced to the grating periodicity. Then, we have to repeat the analysis performed above with this new perturbation in such a way that we can obtain the new expressions of P_1 and P_2 respectively.

On the other hand, another important parameter to analyze is the perturbation coefficient $\kappa = \kappa_{12} \simeq \kappa_{21}$, which contains the information of the fiber index perturbation as it is indicated in Equations (1.34) and (1.37). With this coefficient, one can control the depth of the attenuation bands observed in Figure (1.8) and the ideal length L of the grating. For example, let us consider a LPFG with length $L' < L$. Now, if the amplitude of the periodical perturbation in the refractive index is incremented, the depth of the attenuation bands grows up to reach a limit. At this point the grating length L' is equal to the ideal grating length $L = \frac{\pi}{2\kappa}$. Then, if we increment after this point the amplitude of the periodical perturbation, the depth of the attenuation bands is reduced; however, if we continue increasing the amplitude of the perturbation, the depth of the attenuation bands grows again up to reach the limit value. It means that L' has the following integer multiple value of L. This behavior is very common in many LPFG experiments, nevertheless it is restricted to the physical capacity of the fiber to lead higher values of the perturbation amplitude. Additionally, the coefficient κ depends on the type of coupled modes. In other words, if the LPFG couples modes with even symmetry respect to the transversal coordinates x and y of the fiber (commonly called odd modes), the coefficient κ will have higher values than those for the even modes [7, 19]. This behavior is observed in Figure (1.11), where κ is calculated for different couplings between the fundamental core mode and different higher order cladding modes specified by ν.

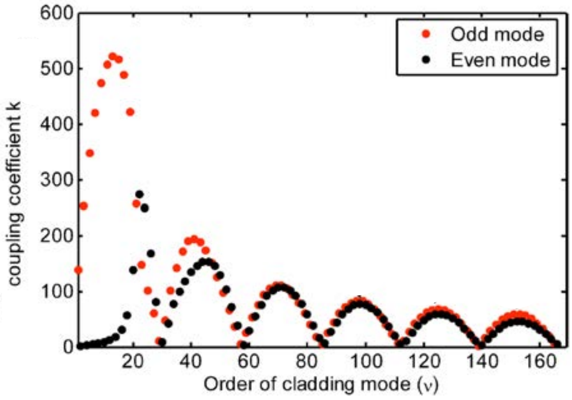

Figure 1.11: Coupling coefficient κ for different cladding modes in a typical fiber, showing odd and even modes separately [19].

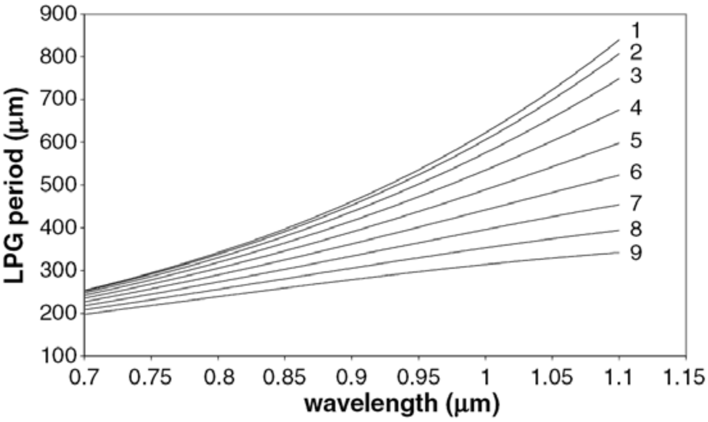

Figure 1.12: Plot of the LPFG period Λ as a function of the resonant wavelength λ for the coupling between the guided core mode and cladding modes of order 1-9 [1].

Let us consider again the phase matching condition $\Delta\beta = \frac{2\pi}{\Lambda}$, which was determined in the deduction of Equations (1.42) and (1.43). If we use Equation (1.44), we can express the phase matching condition as it is indicated in Equation (1.23). This equation is used frequently for researches to characterize the coupling of LPFGs. As an example, Figure (1.12) shows a plot of the grating period Λ as a function of λ obtained from Equation (1.23) [1]. As it can be seen, the different curves represent the coupling between the fundamental mode with different cladding modes numerated from 1 to 9 respectively. These kind of plots are amply used in the experimental results of this work.

1.3 LPFG fabrication methods

The fabrication of LPFGs implies the introduction of a periodic index modulation of the core in the optical fiber. This can be obtained by permanent modification of the refractive index of the fiber core or by physical deformation of the fiber respectively. In the following sections, a brief overview of the four most popular techniques will be described, focusing principally in the manufacture of LPFGs by mechanical methods.

1.3.1 LPFG manufacture by UV irradiation

The ultraviolet (UV) irradiation was the first method used to manufacture gratings in 1989 by Meltz *et al*, who used holographic interference between two coherent beams directed to the fiber axis [20]. Significant improvement was obtained in the manufacture of gratings with this method when Hill *et al* proposed a novel method of UV exposure through a amplitude mask placed in close proximity to the fiber [21]. Later, a further useful technique was presented in the form of a point a point periodic grating manufacture using UV irradiation [22].

The UV exposure method requires that the fiber first be made receptive to UV irradiation, in other words, the fiber must be made photosensitive prior to writing the grating. It can be obtained by doping the fiber core (usually of silica) with impurity atoms (such as germanium, boron or a combination of these elements) or by hydrogen loading exposing the fiber to high-pressure H_2 gas at elevated temperatures for a prolongated period of time so that hydrogen diffusion into the core material takes place. The later method is preferable because hydrogen loading can be achieved in standard fibers, providing a cheaper and simpler way to obtain UV photosensitivity fibers [23].

The UV inscription method for LPFGs can be made in two ways. One of them consists on the irradiation of the fiber through an amplitude mask with the desired period [9]. The amplitude mask can be made of chrome plated silica with a series of periodical slits which allows the UV transmission. The width of the slits correspond to the required grating period. First, the fiber is placed in contact with the amplitude mask so that its axis is oriented perpendicular to the slits of the plate. Then, the mask's pattern is imprinted onto the photosensitive fiber core as shown in Figure (1.13), thus yielding a grating with the same periodicity given on the mask. The inscription occurs when the UV irradiation is exposed in front of the mask where alternate bands of maximum intensity are transmitted. It causes the appearance of peaks in the refractive index modulation of the photosensitive fiber core. The exposure is repeated until the index modulation has reached a sufficient level to provide the desired attenuation depth in the LPFG transmission spectrum. As it can be observed, this technique imply a permanent modification of the refractive index of the fiber core

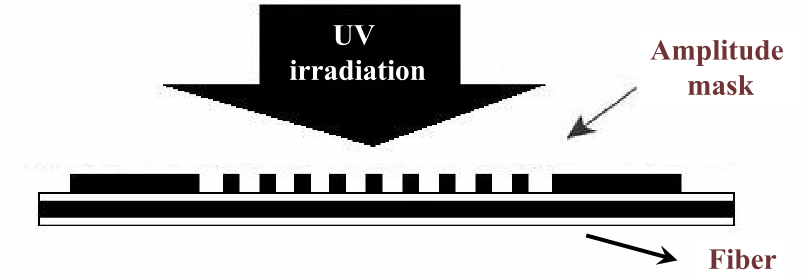

Figure 1.13: Scheme of the UV irradiation method using an amplitude mask technique for LPFG manufacture in UV photosensitive fibers.

A second way to generate gratings with UV irradiation is based on a period by period inscription. This method implies a periodic point by point modulation of the core refractive index until the desired grating length is obtained. Unlike the amplitude mask technique, the index change is induced by a single spot illumination at different points along the fiber, each one separated by the grating period which not necessarily have to be uniform, allowing in this way the fabrication of chirped gratings. In general, both techniques above described are considered expensive [24].

1.3.2 Irradiation by a carbon-dioxide laser

LPFG formation by exposure to a CO_2 laser beam was first investigated by Davis *et al* in order to determine if it is indeed necessary to use UV light for altering the core refractive index [25]. Once it appeared possible to write gratings using a CO_2 laser beam in standard fibers without the need for prior photosensitization, this became a beneficial alternative because LPFGs manufactured with this method require no pre-treatment (photosensitization, for example by hydrogen loading) or post-treatment (annealing or thermal stabilization) [26]. Furthermore, the silica has a strong absorption band corresponding to the wavelength of these laser beams, and CO_2 lasers are relatively inexpensive [27]. The versatility of this technique was revealed when LPFGs were fabricated in photonic crystal fibers by exposing periodically certain points to a CO_2 laser beam, which caused localized collapse of the holey structure due to the heat generated in the fiber [6]. As it is mentioned, this method also imply a permanent modification of the refractive index of the fiber.

Fabrication of LPFGs by CO_2 laser occurs in a point-by-point writing method that is achieved by moving the fiber along a stage and creating the index modulation at specific points as it is shown in Figure (1.14). The opening of a shutter allows the focused laser beam to illuminate the fiber at a specific pulse rate [25, 27]. The LPFG period can then be controlled by the translation of the fiber, and the grating strength is determined by the pulse duration and laser output power respectively [25]. The mechanisms responsible for the grating formation are not due to photo-excitation, in this case (since the exposure is

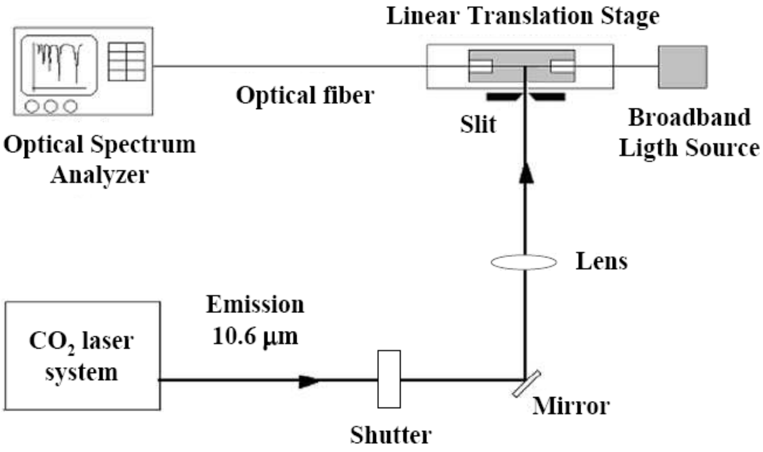

Figure 1.14: CO_2 irradiation using a point by point technique for LPFG manufacture in optical fibers.

not in the UV range), or removal of the fiber material (if no photo-ablation occurs). Then, authors of Ref. [26] suggest that the index modulation is caused by relaxation of the fiber's internal residual stresses [25, 27].

1.3.3 Exposure to electric arc discharge

The continued investigation of methods for LPFG manufacture that do not require photosensitization and UV irradiation has led the use of electric arcs from a commercial fiber fusion splice machine [28]. One advantage of this method is the simplicity of the procedure where not expensive laser equipment is needed. Furthermore, any type of fiber can be used for writing gratings in this way (including photonic crystal fibers) without prior photosensitization, since it is predominantly the local heating of silica that creates the modulation in the fiber.

The fabrication process is based on the following way: the polymer coating of the fiber is removed before fixing it to a translation stage controlled by a motor. This motor allows the fiber to move between the electrodes of a fusion splicer at predetermined intervals as it is shown in Figure 1.15. These motion in intervals stipulates the grating period [29]. An electric arc discharge is applied to the fiber situated between both electrodes, and the electric current (which determines the intensity of the discharge) and the duration of the exposure are defined by the user, or a computer respectively [28, 29]. Point by point writing occurs by advancing the fiber after each discharge has occurred, and the strength of the grating is increased to its desired level by repeating the entire process a specific number of times.

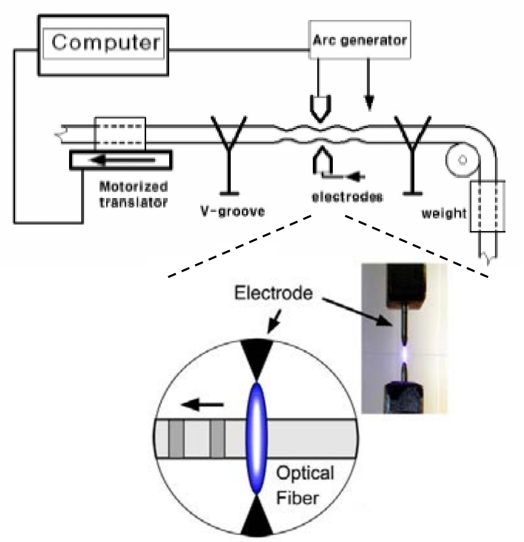

Figure 1.15: Electric arc irradiation using a point by point technique for LPFG manufacture in optical fibers.

Certain experimental setups similar to Figure 1.15 require constant tension applied along the fiber using a mass piece attached to the end of the fiber. The effect of this tension is to cause a periodic tapering where discharges have occurred, but this phenomenon plays a minor role in the grating quality and is not necessary for LPFG manufacture [30]. Adding tension to the fiber tends to increase insertion loss, but it was also found to be beneficial due to that fewer discharges are required during the LPFG manufacture [30]. This method also imply a permanent modification of the refractive index of the fiber.

1.3.4 Mechanically induced LPFGs

Because the index modulation period in a LPFG can be as large as hundreds of micrometers, it is possible to induce it mechanically, for example, by pressing the fiber between a periodically grooved plate and a flat plate as is shown in Figure (1.16). Via the photoelastic effect, the pressure points induce a periodic index modulation [31].

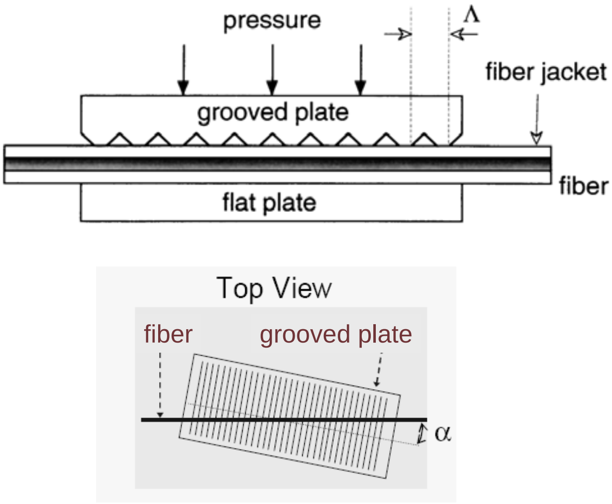

Figure 1.16: Side and Top view of a mechanically induced LPFG setup based on the photoelastic effect of the mechanical pressure on the fiber [32].

An advantageous feature of this design is that one can adjust the grating period Λ, and thus the positions of the notches, by changing the angle α between the fiber and the grooves as is shown in the top view of Figure (1.16). Similarly, the length of the fiber under pressure, which controls the line widths of the notches, can easily be changed. Finally, one can tune the depth of the notches by adjusting the pressure. When the perturbation is removed, the transmission of the fiber returns to its initial spectrum. Thus, a wide range of filter functions can be generated with the same grooved plate and fiber.

Different techniques of mechanically induced tunable LPFGs have been reported in standard fibers and microstructured fibers, where corrugated plates, strings, and springs have been used to apply periodic mechanical stress on the optical fiber in order to induce the effective index modulation to obtain the coupling of light from the fundamental mode to LP cladding modes [32, 33, 34]. One of the most relevant characteristics that share these techniques is their tunability by simple adjustment of the mechanical stress period. Under this concept, mechanically induced LPFGs offer a tuning range at least one order of magnitude wider than other methods reported in tunable permanent recorded LPFGs with similar isolation loss and linewidth [35, 36, 37].

In summary, the main advantages of mechanically induced LPFGs are the wide tuning range and bandwidth control, and that they are erasable and reconfigurable. These characteristics make mechanically induced LPFGs an attractive option when a broadly tunable nonreflecting band-rejection filter is required for applications such as the elimination of communication channels, or to remove Stokes orders in cascaded Raman-based lasers and modulators. Furthermore, they can be used as dynamic gain equalizers in fiber amplifiers or lasers [38], as well as key components in tunable and reconfigurable cascaded LPFGs in multiwavelength Raman lasers, all-fiber Mach-Zehnder interferometers, and wideband polarization-dependent loss compensators [39, 40, 41]. Additionally, mechanically induced tunable LPFGs could find applications in the fiber sensor field [42]. Then, for all these applications it would be useful to develop simple and inexpensive flexible mechanically induced tunable LPFGs.

2 Photonic crystal fibers

In following sections a description of the different classes of photonic crystal fibers and their principal properties are presented. In a similar way, a brief review of different numerical methods used for their modelling are described giving special attention to the Fast-Fourier-Transform (FFT) mode solver used in this work.

2.1 Introduction

Photonic crystal fibers (PCFs) are a new class of optical fibers, which guide light inside their microstructured cladding [43, 2]. The most common type of PCF is the microstructured fiber (MF), which consist of a pure-silica core surrounded by a periodic array of air holes that constitute the cladding. The air holes reduce the effective refractive index of the cladding allowing in this way the propagation of light in the core. The microstructure of the cladding can be varied in order to tailor and control the optical properties of the fiber [3, 44]. As a example, several microstructured fiber have been developed, such as highly nonlinear [45], highly birefringent [4], large-mode field area [46, 47] and high numerical aperture MFs [48]. On the other hand, photonic bandgap fibers (PBFs) are a special class of PCF, that confine light due to a photonic bandgap of the cladding allowing the guidance of light in the low-index core of the fiber [49, 50].

PCFs exhibit some unique features in comparison to all glass standard optical fibers. For instance, PCFs can be designed to guide light in a single transverse mode in the near-UV to near-infrared wavelength range with variable core sizes [51, 52, 53]. Besides, the arrangement and size of air holes allow the tailoring of the waveguide dispersion of PCFs. Thus, the zero-dispersion wavelength can be shifted into the visible region of the optical spectrum [52]. It is also possible to manufacture PCFs that exhibit very low absolute dispersion values over a broad wavelength range [5]. Furthermore, mechanically robust PCFs can be fabricated with extremely small core $< 1\ \mu m$ [52], thus enhancing considerably the nonlinear optical processes along the fiber [51, 45]. Large core single-mode PCFs can also be manufactured for reducing the nonlinear effects [51, 53, 5]. Moreover, high birefringence can be induced in the core to maintain the polarization of light traveling along the fiber [54, 55]. Nevertheless, propagation losses of PCFs are an order of magnitude larger than that of conventional optical fibers [56, 57].

2.2 Classes of photonic crystal fibers

Photonic crystal fibers can be classified in two categories according to their guiding principle: index-guiding microstructured fibers (MF) which guide light in the same way as standard optical fibers, and photonic bandgap fibers (PBF) where the light is confined through the bandgap effect [49, 58]. The transversal sections of these fibers are shown in Figure (2.1).

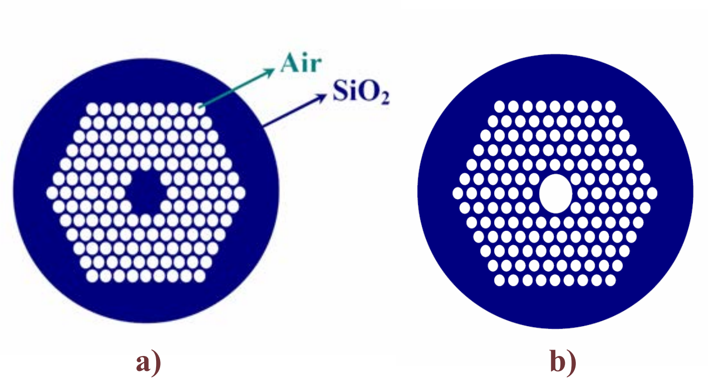

Figure 2.1: Scheme of the cross-section of a) a microstructured fiber (MF), and b) a photonic bandgap fiber (PBF) [63].

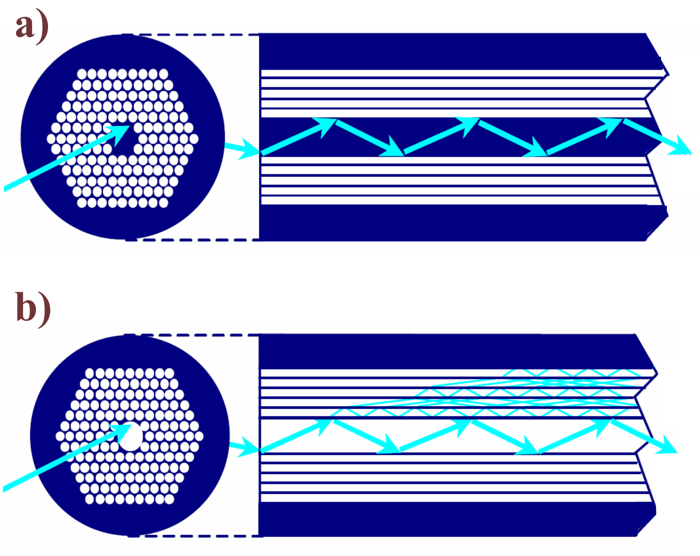

Figure 2.2: Guidance principle in a) a microstructured fiber (MF), and b) a photonic bandgap fiber (PBF) [63].

2.2.1 Microstructured fibers

The core of a microstructured fiber is of fused silica and the cladding is formed by air holes running along the entire length of the fiber. These air holes lower the effective refractive index of the cladding with respect to the core, allowing the guiding of light inside the core by total internal reflection as is indicated in Figure (2.2)a. In such fibers, often referred to as index-guiding MFs or holey fibers, a small fraction of light propagates in the air holes as evanescent fields. Microstructured fibers exhibit unique optical properties compared to standard fibers. For instance, for certain sizes and arrangements of the air holes, MFs can confine the guided light to one single mode for all wavelengths in the visible and infrared [59]. Varying the air hole size, arrangement and symmetry also makes it possible to tailor the group-delay and thereby the dispersion properties of the fiber [60]. Narrow-core MFs have been widely applied in nonlinear optics, *e.g.*, in supercontinuum generation and parametric amplification, due to their enhanced nonlinearity [61, 62, 63]. Large-core, endlessly single-mode MFs with high numerical aperture have been developed for applications in telecommunications and for high power delivery [64]. In particular, recent experiments have shown that it is possible to manufacture a large mode-area MF with an extremely uniform structure [65]. On the other hand, the structure can be made asymmetric in order to substantially increase the birefringence of the fiber. Highly asymmetric MFs have the advantage of maintaining the polarization state of light along propagation [4]. Several reports have also been published on fiber lasers and amplifiers that include a doped-core large mode-area microstructured fiber (LMA-MF) [66]. With this type of design, output powers of several hundreds of watts from MF-based fiber lasers have been demonstrated.

2.2.2 Photonic bandgap fibers

Photonic bandgap fibers (PBFs) differ from MFs by its hollow core. In such structures, the index guiding is prohibited due to the lower refractive index of the core, and, therefore, PBFs guide light by consecutive constructive interferences of reflections from the several air-silica interfaces as it can be seen in Figure (2.2)b. Such periodic air-silica cladding exhibits a bandgap for photons in the radial direction, forcing the photons to propagate inside the core [49]. The large overlap of the propagating mode with the air core considerably reduces the nonlinearity of the fiber allowing the propagation of light with extremely large power levels. These fibers are also used for sensing applications [50], and can be used for dispersion compensation [5]. Also, if we fill the central hole of the PBF with, *e.g.*, liquid crystal, we can form new types of optical components, which can be used for optical switching in communications systems [58].

2.3 Properties of index-guiding microstructured fibers

Due to that the photonic cristal fibers used in this thesis correspond to index-guiding microstructured fibers, only the fundamental properties of this type of fiber will be reviewed in the next sections.

2.3.1 Modal behavior

The number of modes supported by a MF depends strongly on the hole diameter d, the lattice pitch Λ of the periodic hole distribution, and the wavelength λ, respectively. In a similar way to standard fibers, one can use an analogy with the step index fiber model in order to define the V-parameter of MFs, known as the normalized frequency of the fiber,

$$V = \frac{2\pi r}{\lambda}\sqrt{n_1^2 - n_2^2}, \tag{2.1}$$

where n_1 and n_2 are the effective index of the core and the microstructured cladding, and r is the effective core radius. The effective core radius of the MF is commonly approximated to be 0.5 times the lattice pitch Λ [49]. The refractive index of the core corresponds to the silica, and the index of the cladding is the effective index of the space-filling mode [49]. The V-parameter relates the number of modes supported by the core fiber. In particular, for values of $V < 4.2$, only the fundamental mode will be propagated in the MF, which is often desired in telecommunication applications [67] (remember that in standard fibers the single-mode cutoff is $V \leq 2.405$). Examples of V-parameters calculated for MFs as a function of the normalized wavelength Λ/λ are illustrated in Figure (2.3) for different values of d/Λ.

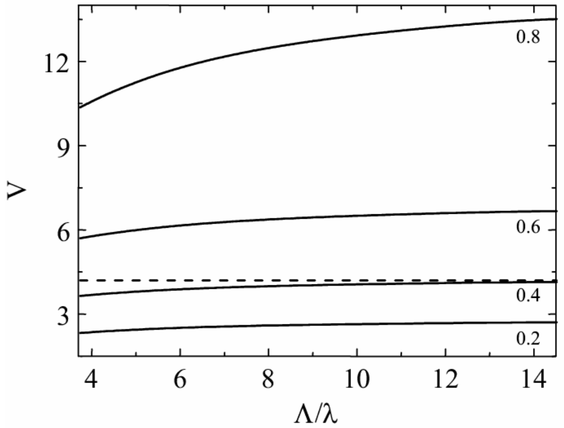

Figure 2.3: V-parameter of microstructured fibers as a function of Λ/λ for different values of d/Λ. $\Lambda = 7\ \mu m$. The dashed horizontal line indicates the first higher-order mode cutoff [62].

For MFs with a relative air-hole diameter $d/\Lambda \leq 0.4$, the V-parameter can not reach the cutoff for the first higher-order mode as it is shown in Fig. (2.3), and there is always a single-mode propagation from 400 to 1600 nm. Such MFs are commonly referred to as *endlessly single-mode fibers* [67]. Microstructured fibers with the relative air-hole diameter larger than ~ 0.4 are multimode. In this case, the distribution of the input light into the modes of the MF is determined by the input coupling conditions. Examples of simulated intensity profiles of the fundamental and higher-order modes propagating in a multimode MF ($d = 6.6$ μm, $\Lambda = 7$ μm, $d/\Lambda = 0.9$) for $\lambda = 1.5$ μm are shown in Figure (2.4).

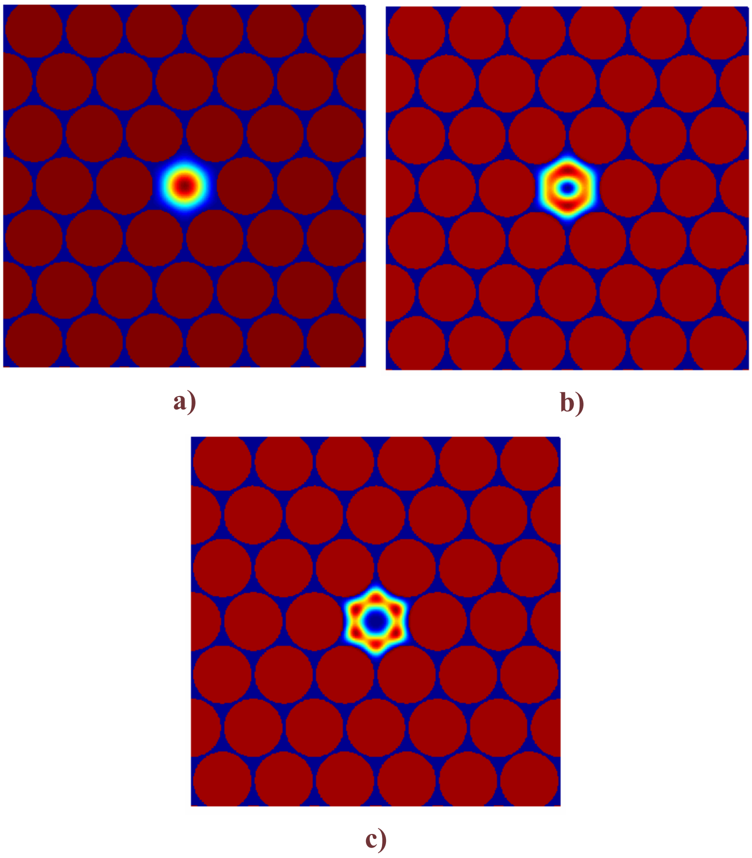

Figure 2.4: Intensity profile of the a) fundamental, and b)-c) first and second higher-order core modes of a MF with $d = 6.6$ μm and $\Lambda = 7$ μm simulated using the FFT-mode solver developed in this work. $\lambda = 1.5$ μm.

2.3.2 Dispersion

The frequency dependence of the refractive index of silica, *i.e.*, the dependence of the propagation velocity on frequency, is commonly referred to as material dispersion. The difference in the refractive index between the core and cladding induces another type of dispersion known as waveguide dispersion. The total dispersion of the fiber is the sum of the material and waveguide dispersion [67]. The effects of dispersion on pulse propagation in optical fibers are typically analyzed by expanding the propagation constant β into a power series around the carrier frequency ω_0 of the pulse:

$$\beta(\omega) = \sum_{m=1}^{+\infty} \frac{\beta_m (\omega - \omega_0)^m}{m!}, \tag{2.2}$$

where $\beta_m = \left[\frac{d^m\beta}{d\omega^m}\right]_{\omega=\omega_0}$. In Equation (2.2) the coefficient β_1 indicates the group delay (GD) and its inverse β_1^{-1} the group velocity (GV) of the pulse, i.e., the propagation speed of the pulse envelope inside the fiber. The group-velocity dispersion (GVD) parameter β_2 expresses that different frequency components of the pulse propagate at different speeds. This effect is responsible for the broadening of the time intensity profile of a pulse during its propagation along the fiber. Depending on its sign the GVD in optical fibers can be divided into two categories: it is called normal when $\beta_2 > 0$, and anomalous when $\beta_2 < 0$. The wavelength at which $\beta_2 = 0$ is referred to as the zero dispersion wavelength λ_{ZD} ($\lambda_{ZD} \approx 1.3\ \mu m$ for conventional optical fibers). In the anomalous dispersion region, shorter wavelengths travel faster than longer wavelengths, and viceversa in the region of normal dispersion. Another common parameter used to describe the effects of dispersion in optical fibers is the dispersion parameter D defined as,

$$D = -\left(\frac{2\pi c}{\lambda^2}\right)\beta_2, \tag{2.3}$$

where λ is the wavelength and c the speed of light in vacuum. The value of D is often given in units of $ps/(nm \cdot km)$.

In MFs, varying the values of d and Λ of the fiber, one can tailor the waveguide dispersion in a wide range in such way that one can obtain different flattened behaviors of the dispersion parameter D [5]. As a example, Figure (2.5) shows the ultra flattened dispersion behavior for three different PCF configurations near the communication window with: positive dispersion ($a = 0.4\ \mu m$ and $\Lambda = 3.12\ \mu m$); nearly-zero dispersion ($a = 0.316\ \mu m$ and $\Lambda = 2.62\ \mu m$); and negative dispersion ($a = 0.27\ \mu m$ and $\Lambda = 2.19\ \mu m$).

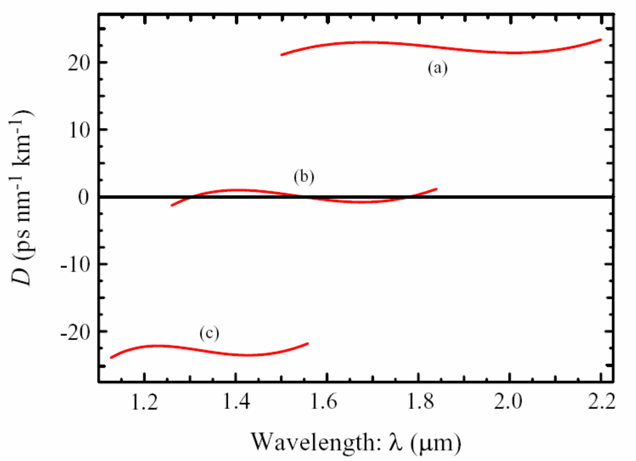

Figure 2.5: Ultra flattened dispersion behavior with: a) positive dispersion, b) nearly-zero dispersion, and c) negative dispersion [5].

2.3.3 Attenuation

The wavelength attenuation range of MFs is limited, in similar way to standard fibers, by both the intrinsic material losses and micro/macro-bending losses of the fiber. The main loss mechanisms in MFs are originated from scattering and absorption [64]. Rayleigh scattering is the main loss mechanism in the wavelength range of 500-1600 nm, whereas below 500 nm the ultraviolet absorption of silica becomes dominant. At wavelengths above 1600 nm, the transmission of the fiber is limited by the strong infrared absorption of silica. Additionally, a strong absorption peak can be located at around 1400 nm resulting from vibrational resonance of the OH-molecules that remain in the fiber after the manufacturing process.

In addition to scattering and absorption, the transmission bandwidth of MFs is also limited by micro-and macro-bending losses. Macro-bending losses in MFs are induced by bending of the fiber to small diameters [68]. In addition, microdeformation induced losses are caused by scattering from interfaces of small irregularities of the fiber or by residual stress of the coating [69]. These two loss mechanisms severely limit the bandwidth to a few hundred nanometers for fibers with small values of the relative air hole diameter.

In Mfs, it is necessary to consider another contribution to the losses, that is the leakage or confinement losses. these are due to the finite number of air holes in the fiber cross-section. The ratio between the air hole diameter d and the lattice pitch Λ must be designed to be large enough to confine light into the core and to reduce the confinement losses. Also, It has been demonstrated a strong dependence of the confinement losses on the number of the air hole rings. In particular, leakage losses can be significantly reduced by increasing the ring number in the microstructured profile [11].

2.3.4 Nonlinearities

The nonlinearity of the fiber is inversely proportional to the effective area of the mode. Therefore, nonlinear MFs have very narrow cores, and thus, small values of the mode field diameter (MFD). The MFD of MFs is strongly dependent on the relative air-hole diameter as it is shown in Figure (2.6) for a fundamental mode of a triangular lattice of circular holes at $\lambda = 1500\ nm$ [70]. The tendency of the MFD to increase for small values of Λ and d/Λ can be explained if we consider that a portion of the mode field can radiate through the silica bridges in the cladding microstructure. For this reason, most fibers designed to have small MFD have very high values of d/Λ. In particular, these fibers are multimode, but with careful coupling of the pump light into the fiber single-mode guidance may be obtained for short lengths of fiber.

Fibers with a core diameter ranging from 1 to 50 μm have been demonstrated [51, 45], and contrary to conventional optical fibers, MFs offer the possibility of scaling the nonlinearities experienced by the propagating mode [20]. Additionally, the area of the propagating mode determined by the MFD parameter also depends on the wavelength. This behavior can be described in Figure (2.7) where a typical dependence of the effective mode area on the wavelength for a 1 μm core MF is shown.

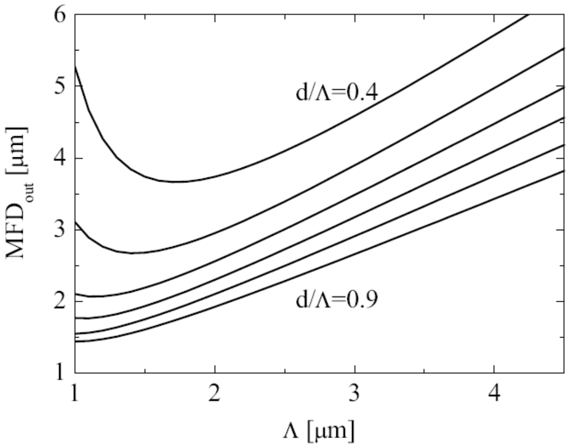

Figure 2.6: Plot of MFD as function of the pitch for MFs with a triangular array of circular holes for different values of d/Λ. $\lambda = 1.5$ μm. [62]

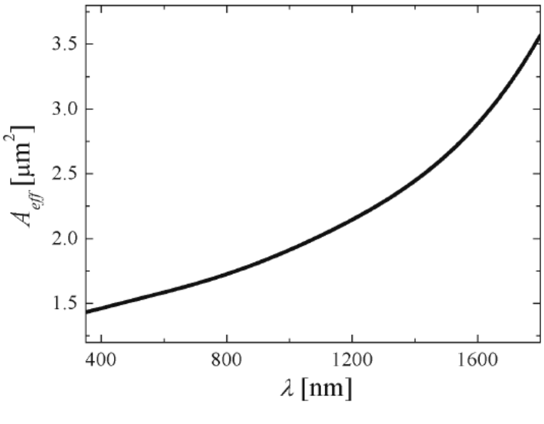

Figure 2.7: Effective mode area as a function of wavelength for a 1 μm core MF. $\Lambda = 1.22$ μm [63].

2.4 Modeling methods

The simple structure of standard fibers allows the analytical solutions of the propagating field by solving a simple eigenvalue equation such as it is described in Chapter 1. The microstructured cladding of PCFs complicates the analysis significantly. The large refractive index contrast and strong contribution of the cladding to the waveguide properties difficult the obtention of an analytical expression for the propagating mode field. Therefore, in most cases, the mode field and properties of PCFs are analyzed through numerical simulations.

In order to make calculations of the microstructured fibers, one must be able to calculate the characteristics of the guided core modes and cladding modes. Many methods have been developed in order to calculate the field distribution of the core and cladding modes, the propagation constant β, and the effective area A_{eff}. Between them, one can find the effective index method [49, 71] where the microstructured fiber is treated as a step index fiber; the localized function method [72] where the electromagnetic field is expanded in localized basis functions such as Hermite-Gaussian functions; the plane wave method [73] which is similar to the previous method with wave planes as basis functions; the multipole method [74] where the field solution is obtained from the boundary conditions on the hole surfaces; the finite element method [75] where a complex and reliable discretization is applied, and the FFT-mode solver [76, 77] which solves the wave equation by moving the fields from the spatial domain to the spectral domain via the FFT algorithm. In the following sections, these numerical methods are briefly described , focusing principally in the FFT-mode solver which is developed in this thesis. As a first step, the principal characteristics of these methods are given in Table (2.1).

2.4.1 Effective index method

In the effective-index method, index-guiding MFs are modeled as step-index fibers as it is shown in Figure (2.8). In this case, the refractive index of the equivalent step-index core

Table 2.1: Characteristics of various methods employed for modeling MFs. The information is based on Refs. [65,76]. MFD: mode-field diameter, β: propagation constant, A_{eff}: effective area, λ: wavelength.

Method	Modeled properties	Model accuracy	Limitations	Computational effort
Effective index	MFD, β	Inaccurate at longer λ	Polarization analysis impossible	Low
Localized function expansion	MFD, β, A_{eff}	Accurate	Relatively complex	Almost Intensive
Plane wave expansion	MFD, β, A_{eff}	Fair	Infinite cladding assumption	Intensive
Multipole expansion	MFD, β, A_{eff}	Reliable	Symmetric structures	Intensive
Finite Element	MFD, β, A_{eff}	Reliable	Relatively complex	Very Intensive
FFT mode solver	MFD, β, A_{eff}	Fair	Infinite cladding assumption	Intensive

fiber is composed of pure silica, and the index of the cladding is determined from the effective index of the so-called space-filling modes [49]. The index of the space filling mode is found by solving the mode that propagates if the defect is removed, *i.e.*, if the microstructured cladding is assumed to be continuous and infinite. Knowing the propagation constant β_{SFM} associated with the space-filling mode, the effective refractive index of the cladding of the equivalent fiber can be deduced from,

$$n_{eff}(\omega) = \frac{\beta_{SFM}(\omega)}{k}, \tag{2.4}$$

where $k = \omega/c$, and ω is the angular frequency of the wave in free space. The MF can then be treated as an ordinary step-index fiber. In general, the core radii of the equivalent fiber is considered 0.5Λ [49, 71]. It is important to mention that the effective index method is fairly accurate only when the fundamental mode is well confined inside the core of the fiber. Nevertheless, the method permits to obtain a quick estimation of the waveguiding properties of the fiber.

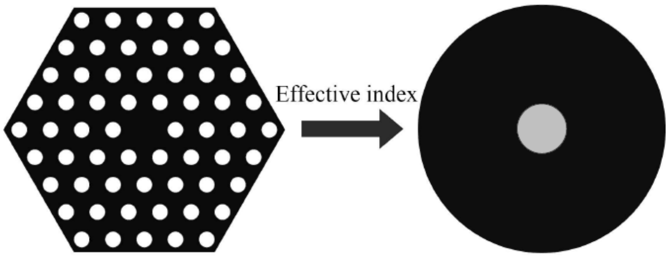

Figure 2.8: A microstructured fiber with air holes on a triangular cladding structure, and a solid core-region created by the omission of the central air hole. It resembles a step-index fiber with a wavelength dependent cladding index [69].

2.4.2 Localized function method

The most accurate way of simulating light field distribution in a waveguide is to directly apply Maxwell's equations. In order to simplify the calculations, the structure or the field is often expanded into a sum of periodic functions, for which Maxwell's equations are solved. The localized functions expansion method developed for analyzing PCFs consists in expanding the electromagnetic field and the structure of the fiber into a specific number of Hermite polynomials [72, 78]. For such field, the Maxwell's equations reduce to an algebraic eigenvalue problem, which can be solved analytically by standard algorithms. The accuracy of the technique scales with the accuracy of the description of the refractive index profile. For this purpose, it may be necessary to use a large number of polynomials, which drastically increases the computational demands, particularly for larger and more complex structures.

2.4.3 Plane wave method

On the other hand, the plane-wave expansion method, which is widely used to simulate photonic crystal structures, consists in solving the vectorial wave equation in the reciprocal space of the periodic cladding structure. Basically, in this method the electromagnetic field is expanded using plane waves according to the Bloch's theorem [73, 78]. Also, the complex periodic permittivity (dielectric constant) is expanded using plane waves. In order to treat a spatial defect such as a core region, a super periodicity including the defect is introduced where the defect is also periodically repeated. This supercell approximation can accurately determine the properties of the core region if the supercell is large enough to ensure that neighboring defects are uncoupled. The modal fields and their propagation constants may be found by solving a matrix eigenvalue problem that is derived from a variational method. Additionally, the plane wave expansion method can be applied not only to index-guiding MFs but also to PBFs.

2.4.4 Multipole method

In the multipole expansion method, the electric field is expressed as a sum of Fourier expansions around the individual holes of the structure [74, 78]. The actual field is obtained from the boundary conditions on the hole surfaces. The mathematical solution of the problem is then found by solving a set of matrix equations, which limits the type of structures that can be simulated. Without symmetry, the computation time approaches infinity. Nevertheless, for symmetrical structures, the method is reasonably fast for a small number in terms of the Fourier-expansions. If more terms are needed, the method becomes computationally intensive.

2.4.5 The Finite element method

In the finite element method (FEM) [75, 78], instead of solving directly the wave equation, an alternative functional equation obtained with variational methods is analyzed. In this method, the fiber cross section is divided into the so-called elements, an equivalent discretized model for each element is constructed, and then all the element contributions to the whole fiber cross section are assembled, resulting in a matrix eigenvalue problem with nodal variables as unknowns. In contrast to the basis-function expansion methods described above, the FEM takes the expansion coefficients as unknowns. As a result, the matrices derived from the FEM and the basis-function expansion approach become sparse and dense respectively.

2.4.6 FFT-mode solver

In this method, the wave equation is solved by moving the fields from the spatial domain to the spectral domain via the FFT algorithm [76, 77]. To describe this method, we first consider the vector wave equation that governs the propagation of the transverse components of the electric or magnetic fields given previously in Equations (1.9) and (1.10). If we analyze only the trasnversal electric field $\boldsymbol{E}_t$, one can identify that equation (1.9) is divided in two equations for each component E_x and E_y respectively. Thus, these equations can be written as follows,

$$\begin{cases} \frac{\partial^2 E_x}{\partial y^2} + \frac{\partial}{\partial x}\left[\frac{1}{n^2}\frac{\partial}{\partial x}(n^2 E_x)\right] + k^2 n^2 E_x + \frac{\partial}{\partial x}\left[\frac{1}{n^2}\frac{\partial}{\partial y}(n^2 E_y)\right] - \frac{\partial^2 E_y}{\partial y \partial x} = \beta^2 E_x \\ \frac{\partial^2 E_y}{\partial x^2} + \frac{\partial}{\partial y}\left[\frac{1}{n^2}\frac{\partial}{\partial y}(n^2 E_y)\right] + k^2 n^2 E_y + \frac{\partial}{\partial y}\left[\frac{1}{n^2}\frac{\partial}{\partial x}(n^2 E_x)\right] - \frac{\partial^2 E_x}{\partial x \partial y} = \beta^2 E_y \end{cases} \tag{2.5}$$

where k is the free space propagation constant, $n(x, y)$ is the transversal refractive index profile of the fiber, and $E_x(x, y)$ and $E_y(x, y)$ are the transversal field components. Both equations given in (2.5) are coupled and can be expressed as follows,

$$\begin{bmatrix} L_{xx} & L_{xy} \\ L_{yx} & L_{yy} \end{bmatrix} \cdot \begin{Bmatrix} E_x \\ E_y \end{Bmatrix} = \beta^2 \begin{Bmatrix} E_x \\ E_y \end{Bmatrix}, \tag{2.6}$$

where L_{pp} and L_{pq} are linear operators defined as,

$$L_{pp} E_p = \frac{\partial}{\partial p}\left[\frac{1}{n^2}\frac{\partial}{\partial p}(n^2 E_p)\right] + \frac{\partial^2 E_p}{\partial q^2} + k^2 n^2 E_p, \tag{2.7}$$

$$L_{pq}E_p = \frac{\partial}{\partial p}\left[\frac{1}{n^2}\frac{\partial}{\partial q}(n^2E_q)\right] + \frac{\partial}{\partial q}\left[\frac{\partial}{\partial p}(E_p)\right]. \tag{2.8}$$

In these equations, $p = x, y$ and $q = x, y$ respectively. Equation (2.6) represents the matrix eigenvalue equation for E_x and E_y. Now, Equation (2.6) is discretized in the following way: first, both E_x and E_y components are expanded into a two-dimensional Fourier series,

$$E_x(x, y) = \sum_{m=-N_x/2}^{N_x/2}\sum_{n=-N_y/2}^{N_y/2} c^x_{mn} e^{j(m\frac{2\pi}{X_0}x+n\frac{2\pi}{Y_0}y)}, \tag{2.9}$$

$$E_y(x, y) = \sum_{m=-N_x/2}^{N_x/2}\sum_{n=-N_y/2}^{N_y/2} c^y_{mn} e^{j(m\frac{2\pi}{X_0}x+n\frac{2\pi}{Y_0}y)}, \tag{2.10}$$

where c^x_{mn} and c^y_{mn} are their respective Fourier series coefficients, N_x and N_y are the number of harmonics in each direction, and (X_0,Y_0) is the size of the computational window. At this point, we can follow two ways to solve Equation (2.6). The first one is introducing the Fourier series expansion given in equations (2.9) and (2.10) into equation (2.6) and then, apply the Galerkin method [76]. In this way, we can obtain the following equation system,

$$\begin{bmatrix} A_{xx} & A_{xy} \\ A_{yx} & A_{yy} \end{bmatrix} \cdot \begin{Bmatrix} c^x_{mn} \\ c^y_{mn} \end{Bmatrix} = \beta^2 \begin{Bmatrix} c^x_{mn} \\ c^y_{mn} \end{Bmatrix}, \tag{2.11}$$

At this point c^x_{mn} and c^y_{mn} are unknown. As it can be seen, each of the coefficient vectors c^x_{mn} and c^y_{mn} have $(m \times n)$ elements. If we consider all possible values that m and n can have according to Equations (2.9) and (2.10), we can deduce that the size of each vector coefficient c^x_{mn} and c^y_{mn} is $N = (N_x + 1) \times (N_y + 1)$. Additionally, in Equation (2.11), new operators A_{xx}, A_{xy}, A_{yx}, and A_{yy} have been defined. These operators are dense square matrices that result from the Galerkin method [76]. To solve this equation, first one have to calculate the new operators A_{pq} which is usually not an easy task, and then diagonalize numerically the matrix of the left side of Equation (2.11) by any standard routine. In this way, one can obtain the eigenvalues β with their corresponding eigenvectors.

Nevertheless, there is a second way to solve Equation (2.6) which is used in this work. It consists in the discretization of the field components E_x and E_y in the coordinates (x, y) in such a way that it coincides with the discretization of the Fourier expansion realized in Equations (2.9) and (2.10). Then, we multiply the operator matrix and the **E** field vector found in the left side of Equation (2.6), as is indicated in equations (2.7) and (2.8) respectively, in such a way that the following properties are applied:

- For the terms, where there is a derivative, $\frac{\partial E_p}{\partial p}$ or $\frac{\partial E_p}{\partial q}$, the Fourier transform of E_p is applied by means of the Fast-Fourier-Transform (FFT) algorithm, and then, the result is multiplied with the derivative in the spectral domain given by $j\omega_p$ or $j\omega_q$. Therefore, once this product is obtained, an inverse Fast-Fourier-Transform (IFFT) is applied in order to return to the space of coordinates (x, y).
- For the terms where there is a derivative $\frac{\partial}{\partial i}(n^2 E_i)$, a FFT transform is applied to the product $n^2 E_i$ and the same procedure is done.

Then, the resulting matrix of the product in the left side of Equation (2.6) is diagonalized, and the eigenvalues β with their corresponding eigenvectors are obtained.

In summary, with the latter option, the derivatives and products by a function are directly computed either in the frequency and in the spactial domain, in which they are diagonal operators. We move efficiently from one domain to the other via the FFT algorithm. Following this strategy, two benefits are already achieved. First, memory requirements are drastically reduced, since it is not necessary to explicitly calculate the dense operator given by the application of the Galerkin method. Second, computation time is reduced because, in the iterative diagonalization solver, the matrix-vector products are efficiently evaluated with the help of the FFT algorithm. This fact allows an increment in the number of harmonics N_x and N_y that can be used in the simulation [77].

2.5 FFT-mode solver implementation in PCFs

As it was mentioned above, the FFT-mode solver is the numerical method used in this work. This method is choosen due to its flexibility to be applied in different transversal structures of the microstructured cladding, i.e. in periodic or aperiodic distribution of holes using either circular or elliptic air holes respectively. Additionally, the implementation of this method is easier than others. Nevertheless, in the FFT-mode solver the numerical error for the calculated effective index n_{eff} of each mode is around $1x10^{-6}$ which is 1 magnitude order higher than that shown in other methods. This is an important characteristic to consider, because a high precision is required in order to distinguish the degenerated modes that are guided in PCFs [79]. For example, in the case of PCFs with circular air holes and a perfect hexagonal arrangement of holes, the degenerated solutions of the fundamental mode have effective index differences around $1x10^{-7}$, while for higher order modes this difference is $1x10^{-6}$. However if the PCF shows a slight imperfection in its hexagonal structure, which is frequently observed in manufactured PCFs with non exactly circular holes, the effective index differences of the almost degenerated modes increases up to $1x10^{-6}$. In some specific cases, the FFT-mode solver can reach precisions around $1x10^{-7}$ only if the discretization number of the E field is highly increased. In particular, for the analysis of mode couplings in LPFGs, the precision of $1x10^{-6}$ in the effective index value is sufficient in this work.

According to the phase matching condition given in Equation (1.23) to simulate the mode coupling in LPFGs, it is necessary to calculate the effective index of the modes in the PCF. These modes are guided linearly in the fiber according to Equations (1.9) and (1.10). Additionally, the fiber can also guide modes in the nonlinear regime which corresponds to the case where the refractive index of the fiber core responds in nonlinear way with the intensity of the incident wave. In this case, the refractive index n of Equations (1.9) and (1.10) depends on the calculated field. These equations can be solved in the nonlinear regime using an iterative self-consistent technique combined with a linear method similar to those described in Section 2.4 [80]. One method suggested to calculate these nonlinear modes is the FFT-mode solver. In this case, the nonlinear guided modes are not degenerated and no problem with respect to the method precision is presented. Initially, the calculation of nonlinear guided modes in PCFs was performed using the scalar wave Equation (1.8) which has allowed the study of spatial solitons and higher-order vortex properties in PCFs [81, 82]. Nevertheless, a vectorial calculation is required in order to describe completely the nonlinear modes in PCFs, where vectorial terms are important. Until now, only two methods have been modified to incorporate calculations of nonlinear modes in vectorial way: the Finite element method [83], and the FFT-mode solver performed in this work. Examples of the implementation of the FFT-mode solver in the linear and nonlinear regime are presented in the following sections.

2.5.1 Linear regime

In this section, the numerical mode solution of three different PCFs using the FFT-mode solver is presented. The PCFs used in this work are shown in Figure (2.9). The holey fiber called 1 is a polarization-maintaining holey fiber (commercialized by Blaze photonics) with $d = 2.2\ \mu m$, $\Lambda = 4.5\ \mu m$ ($d/\Lambda = 0.488$), and two holes with $d = 4.2\ \mu m$; the holey fiber called 2 is a microstructured fiber fabricated by Dr. Ismael Torres in Virginia Tech with $d = 5\ \mu m$ and $\Lambda = 11\ \mu m$ ($d/\Lambda = 0.45$), and the holey fiber called 3 is a microstructured fiber (commercialized by Crystal Fiber) with $d = 3.4\ \mu m$ and $\Lambda = 6.8\ \mu m$ ($d/\Lambda = 0.5$). One can observe that holey fiber 1 shows an elliptical core, while the holey fiber 2 shows an asymmetric cladding structure. The holey fiber 3, on the other hand, shows an almost hexagonal structure of its air holes in the cladding.

According to Section 3.2.1, for $d/\Lambda < 0.4$, the PCF has a monomodal behavior. Then, the holey fibers used in this work are multimode and lead to the propagation of the fundamental LP_{01} core mode and higher-order LP core modes. The implementation of the FFT-mode solver to each holey fiber shown in Figure (2.9) gives as a result the intensity distributions of the fundamental core mode LP_{01}, and the even and odd LP_{11} core modes shown in Figures (2.10), (2.11), and (2.12) respectively. These intensity distributions are composed by two components E_x and E_y. From these figures, one can observe that the behavior of the LP_{11} modes is similar to those of in standard step-index fibers with elliptical core as it is mentioned at the end of Section 1.1. It is also very interesting to observe that the elliptical form of the fundamental core mode is less evident from fiber 1 to 3. It is due to the shape of their effective fiber cores respectively.

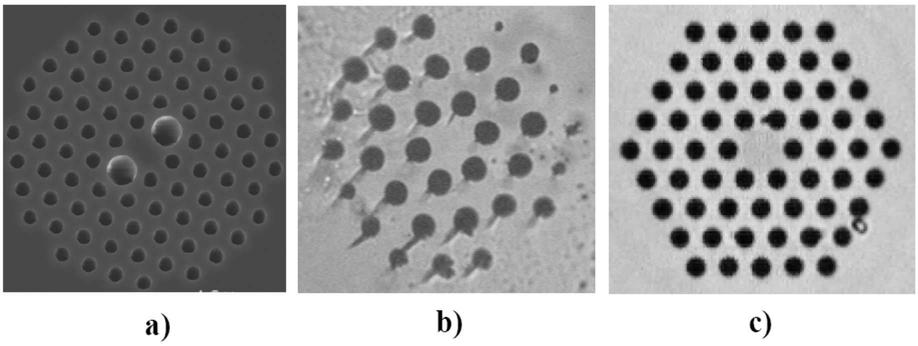

Figure 2.9: Transversal structure of the refractive index profile of three microstructured fibers called holey fiber: a) 1, b) 2, and c) 3 respectively.

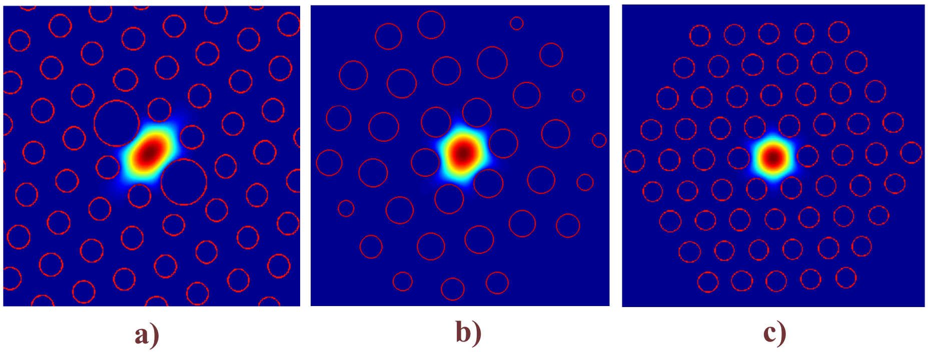

Figure 2.10: Calculated intensity distributions of the fundamental LP_{01} core mode for holey fibers shown in Figure 2.9, a) 1, b) 2, and c) 3 respectively.

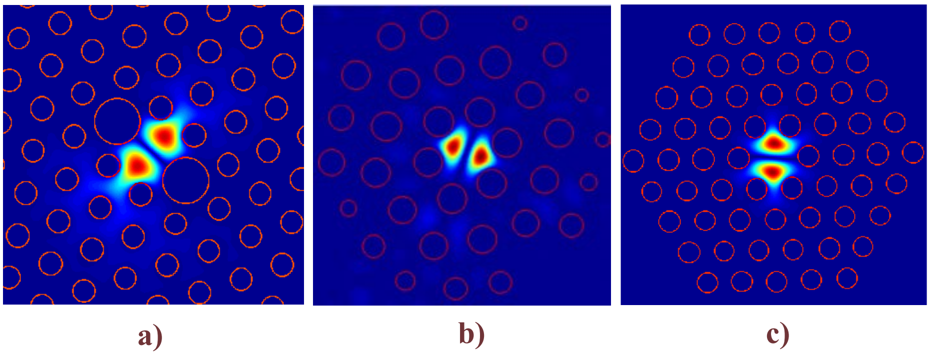

Figure 2.11: Calculated intensity distributions of the higher-order even LP_{11} core mode for holey fibers shown in Figure 2.9, a) 1, b) 2, and c) 3 respectively.

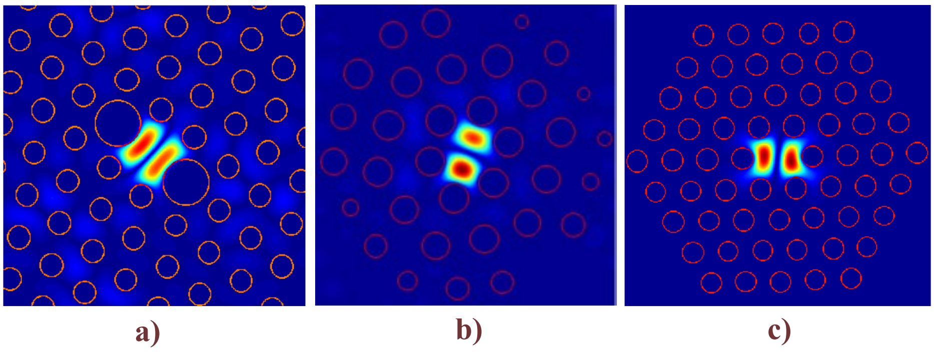

Figure 2.12: Calculated intensity distributions of the higher-order odd LP_{11} core mode for holey fibers shown in Figure 2.9, a) 1, b) 2, and c) 3 respectively.

The corresponding effective index values of the LP core modes for each holey fiber analyzed in this section is shown in Figure (2.13). As it can be seen, the effective index curves that correspond to the even and odd LP_{11} core modes are more separated as the shape of the fiber core is more elliptic. For holey fiber 3 (which shows an almost perfect hexagonal structure), these curves are very close. It means that the core of holey fiber 3 can be interpreted as circular, and consequently, the even and odd LP_{11} core modes are almost degenerated. Also, it is worth mentioning that each curve observed in Figure (2.13) is composed by the superposition of two curves which represent the effective index of both components E_x and E_y of each LP mode respectively.

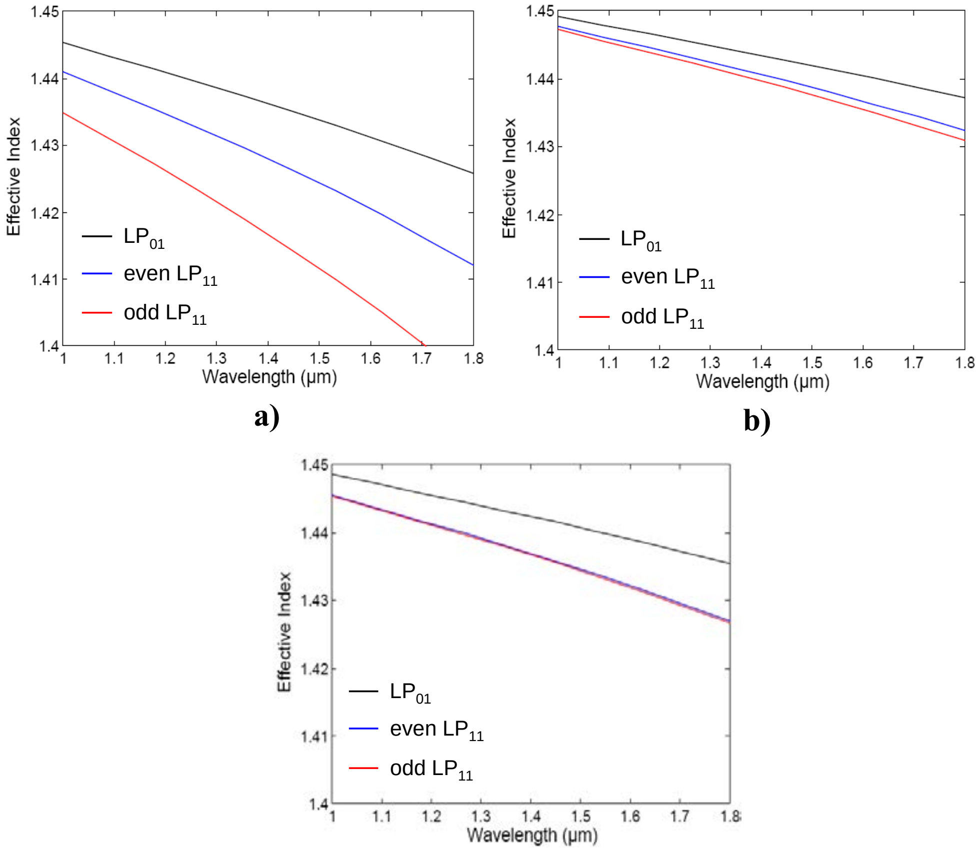

a)

b)

c)

Figure 2.13: Effective index curves of the fundamental LP_{01} core mode, and the even and odd LP_{11} higher order modes for holey fibers: a) 1, b) 2, and c) 3.

If we consider again the phase matching condition given in Equation (1.23), one can obtain the LPFG resonances for each holey fiber by means of their corresponding effective index curves given in Figure (2.13). In these cases, only two resonances that correspond to couplings between the LP_{01} core mode and the even and odd LP_{11} core mode can be obtained. The results are shown in Figure (2.14) respectively. It is also worth mentioning that the mechanically induced LPFGs manufactured in this work have grating periods $\Lambda > 450\ \mu m$. Then, according to Figure (2.14), we only can access to mode couplings of holey fibers 2 and 3. The behavior of these couplings will be characterized in Chapter 3.

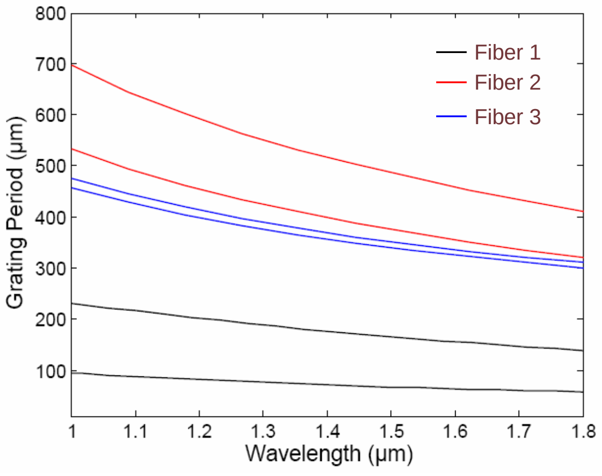

Figure 2.14: Plot of the grating period, Λ, as a function of resonance wavelength λ (LPFG resonances) for holey fibers 1, 2 and 3 shown in Figure 2.9.

2.5.2 Nonlinear regime

As it was mentioned above, the PCFs can guide nonlinear spatial modes. It occurs when the refractive index of the fiber core responds in nonlinear way respect to the intensity of the incident wave. In particular, we analyze the third order nonlinearity of the refractive index (usually called Kerr nonlinearity) which is given as follows [81],

$$n = n_0 + \gamma(|E_x|^2 + |E_y|^2), \tag{2.12}$$

where n_0 is the linear refractive index of the core, and γ is the nonlinear coefficient. To calculate the nonlinear modes, we have to use an iterative self-consistent algorithm [80] which is described as follows: first, we choose an initial $\boldsymbol{E}$ field to construct the nonlinear refractive index n_{NL}, and then we solve Equation (2.5) using n_{NL} by means of the FFT-mode solver. After that, a group of solutions is found. At this point, we choose the most adequate solution to be used as a new initial $\boldsymbol{E}$ field. Once the correct partial solution is chosen, it is substituted again in Equation (2.12) to obtain a new expression of n_{NL}, and the process described above is repeated. The iterative algorithm stops when the new obtained partial solution does not change with respect to the previous one. The critical point in this methodology is to select the correct partial solution in each step of the iterative method. It is due to the fact that after each diagonalization of the FFT-mode solver, there is a group of mode solutions that obey different symmetries (for example, the fundamental spatial soliton and the higher-order vortex solitons). Then, if we want to analyze only a specific mode, we have to choose between these partial solutions adequately. In this case, we always choose a mode with the highest effective index which corresponds to the spatial fundamental soliton respectively. The results are shown in Figure (2.15), where one can observe the intensity distributions of each component E_x and E_y of the spatial fundamental soliton.

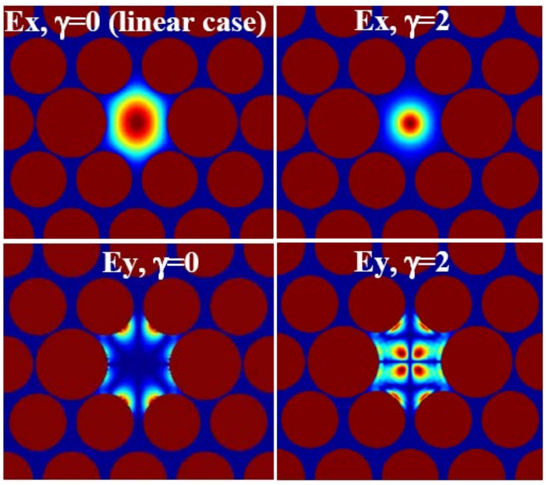

Figure 2.15: Intensity distributions of the components E_x and E_y for a fundamental core mode in the lineal case with $\gamma = 0$, and for a spatial fundamental soliton in the nonlinear case with ($\gamma = 2$). The PCF parameters are: $d = 6$ μm, $\Lambda = 7$ μm, and $\lambda = 1.5$ μm. The calculations were obtained by using the FFT-mode solver performed in this work.

Up to now, the nonlinear modal solutions in PCFs have been calculated using the scalar wave equation in a self-consistent algorithm [81, 82]. Nevertheless, this scalar approximation should not be used in PCFs where the vectorial terms of equation (2.5) are not negligible. This characteristic can be observed in Figure (2.16) where a comparison of the effective index calculation of the spatial fundamental soliton in vectorial and scalar regime is plotted. On the other hand, it is worth mentioning that the nonlinear modal solutions in waveguides could no be stable [80]. Then, to prove the stability of the nonlinear solutions above calculated, we have to analyze its propagation along the PCF by perturbation methods, although this analysis will be performed in future works.

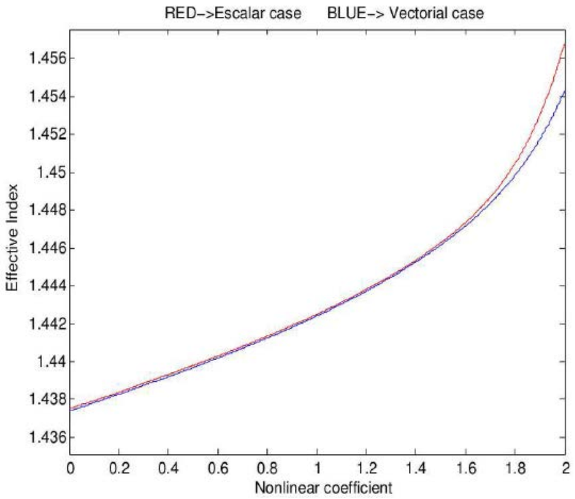

Figure 2.16: Effective index of the spatial fundamental soliton as a function of the nonlinear coefficient γ in a PCF calculated in the scalar and vectorial regime for different nonlinear coefficients γ.

3 Characterization of LPFGs in PCFs

In this Chapter, a series of experiments and results are described by means of three works. These works were done in order to characterize the response of LPFGs induced mechanically in PCFs. The PCFs used in these works were described in Chapter 2.

3.1 Widely tunable LPFG in a PCF

In this section, a novel widely tunable long-period holey-fiber grating obtained by the use of mechanical pressure is presented. The experimental results show a tuning range of the LPFG attenuation bands over 600 nm, with depth notches of 12 dB, and adjustable bandwidth from 10 to 40 nm. These characteristics and its simple implementation make it an attractive widely tunable mechanically induced long-period holey-fiber grating with potential applications in optical fiber communications, tunable fiber lasers, and all-fiber devices.

3.1.1 Experiment and results

In this proposal, the mechanically-induced tunable long-period holey-fiber grating (LPHFG) is obtained by pressing an adjustable half-semicircular section of a single-mode holey fiber that lies on a radial corrugated grooved plate (CGP) with the use of a flat plate as it is shown in Figure (3.1)a. This simple radial design permits to select the period (Λ) by adjusting the bending radius R. Thus a continuous tunability of the long-period holey-fiber grating from near-infrared to visible is obtained. Figure (3.1)b shows a photograph of the transversal section of the fiber used in this experiment which correspond to holey fiber 2 analyzed in Section 2.5.1. This fiber has a 11 μm core and 125μm cladding diameter with 5μm hole diameter and lattice pitch of 11μm.

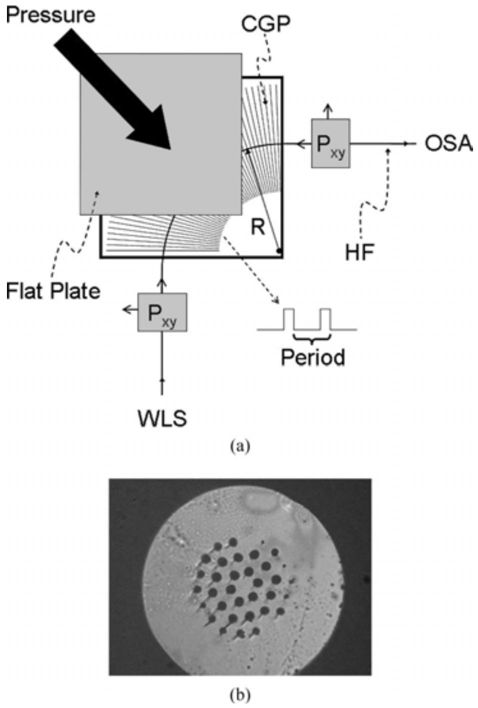

Figure 3.1: (a) Scheme of the experimental mechanically induced LPHFG setup. (b) Cross-sectional image of the holey fiber 2.

The novel corrugated metallic plate was fabricated with a radial step grooved pattern, which contains 60 step grooves, and each one has 360 μm diameter and 900 μm depth. The CGP design allows one to change continuously the period (Λ) by adjusting the bending radius R, according to the expression $\Lambda = (\pi/120)R$. For this particular design, the period Λ varies from 393 to 1308 μm. The dimensions of the CGP and the cover flat plate are 50 mm long and 50 mm wide, and the half-semicircular grooved sector in the corrugated plate has internal and external radii of 15 mm and 50 mm, respectively.

For the spectral characterization of the LPHFG, a signal from an unpolarized white light source (WLS) was launched into one end of the HF through a fiber connector (FC), while the other end was coupled to the optical spectral analyzer (OSA). Then, the fiber was laid in half semicircular form on the grooved plate employing two x-y translation stages (P_{XY}), and a simple manual press system was used to push the cover flat plate on the CGP. The transmission spectra of the long-period holey-fiber grating for different values of the grating period Λ is plotted in Figure (3.2)a-c, where we can observe a tunable range, of at least 600 nm, from 970 to 1580 nm and depth notches from 12 to 16 dB. In all cases, the out-of-band loss was less than 0.75 dB. The entire transmission spectrum was separated in three sections. In Figure (3.2)b, one can observe an absorption band at $\lambda = 1382$ nm that corresponds to the absorption of remnant water in the holey fiber. Figure (3.2)d shows the central resonance wavelength of the LPHFG as a function of the period, where we can observe the typical red-shift of the resonance wavelength as the period grating is increased. We have found from the experimental data that the dependence of the center wavelength on the grating period can be approximately fitted by a third-order polynomial, i.e., $\lambda_{center} = \sum_{i=1}^{4} c_i \Lambda^{i-1}$, where Λ is the grating period and the coefficients c_i are given by $c_1 = 4095.08$, $c_2 = 7870.59$, $c_3 = 4082.77$, and $c_4 = 1149.82$. On other hand, we did not find any limitation in the bending radius to reach the L communication band. In this region, a bending radius of 16 mm was necessary to have a resonance peak at 1591 nm, which is larger than the critical bending radius for holey fibers [68].

The bandwidth ($\Delta\lambda_0$) of the LPHFG keeps approximately constant in the tuning range, as it can be observed in Figure (3.2)a-c; however, the bandwidth control of the LPHFG can be realized by changing the number of the periods (N) in the grating according to $\Delta\lambda_0/\lambda = 0.8/N$. Figure (3.3)a illustrates the transmission spectra bandwidth variation for different numbers of periods at $\lambda = 1288.2$ nm and $\Lambda = 0.514$ mm. In this figure one can observe a wider bandwidth when we decrease the number of periods, which is accompanied by a reduction in the notch depth. Figure (3.3)b shows the behavior of the bandwidth as a function of the number of periods. The notch depth depends directly on the pressure

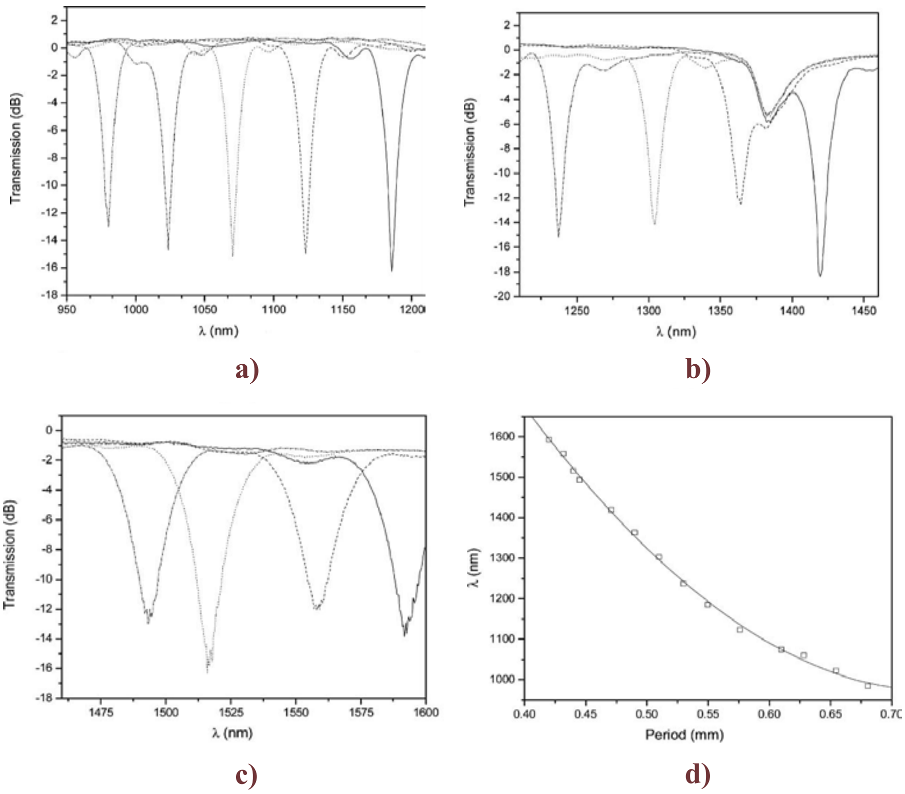

Figure 3.2: (a-c) Transmitted spectra of the LPHFG for different periods. (d) Central peak shift with period variation.

exerted over the fiber by the flat plate; however, if the pressure is increased excessively, we observe a reduction of the notch depth. Also the bandwidth of the LPHFG can be adjusted by introducing a chirp in the periodic perturbation of the LPHFG. For $N = 40$ and a small monotonically variation in the period, the bandwidth was almost constant, but for a linear change of 12 μm, we found that the bandwidth could increase from 15 to 20 nm, although the depth of the attenuation band decreased to 8 dB. Finally, it was not possible to test the polarization dependence of the proposed LPHFG. However, since the pressure in one direction induces asymmetrical stress and deformation on the fiber structure, which results in induced linear birefringence, we can predict that the change in input polarization states in the mechanically induced LPHFG indeed results in distinctive resonance wavelength for each eigenpolarization state, as reported by D. Lee et al. [84].

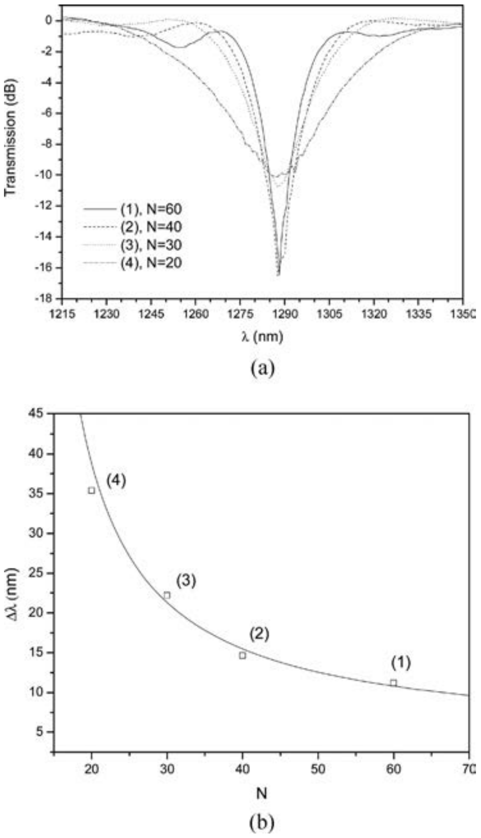

Figure 3.3: (a) Transmitted spectra notch as a function of the number of the periods in the grating ($N = 20, 30, 40, 60$ and $\Lambda = 0.514$ mm). (b) Bandwidth notch at $\lambda = 1288$ nm and with $\Lambda = 0.514$ mm.

3.1.2 Discussion

According to these results, the proposed long-period holey-fiber grating offers a wide tunable range from visible to near-infrared with simple selective resonance wavelength center and bandwidth control. Mechanical tests on the fatigue of the holey fiber were not realized. But the experimental results showed that the same fiber can be used under many repetitive cycles of pressure without loss of mechanical fiber integrity. Also, the engraved gratings preserve their transmission spectra for days. One technical drawback of this mechanically induced

LPHFG, for several specific applications, is its tunability in real time, since it is limited by the response time of the mechanical system involved in the bending fiber adjustment and the pressing rig. Nevertheless, in spite of these limitations, the proposal configuration promises to be very useful for diverse applications in the development of all-fiber devices.

3.1.3 Conclusions

In summary, a simple ultra-widely tunable long-period holey-fiber grating induced by a mechanical method was proposed. The long-period holey-fiber grating shows a continuous tuning range over 600 nm with simple selective center wavelength, and more than 12 dB depth notches, with less than 0.75 dB out-of-band loss. Additionally, the configuration offers to be erasable and reconfigurable in the fiber and low-cost implementation.

3.2 Higher-order core mode resonances in LPFGs

As it was mentioned above, an important element to consider in a mechanically induced LPFG is the type of optical fiber used. In this matter, holey fibers have been demonstrated to be an adequate medium to implement LPFGs [85, 86, 87]. One of the principal features observed in holey fibers is that when they show a perfect hexagonal arrangement of holes, the first higher order core modes TM_{01}, TE_{01}, and HE_{21} are degenerated and resemble the LP_{11} core modes observed in standard communications fibers [88, 79]. Nevertheless, any slight disorder in the inner air hole lattice can make them split into the odd- and even-LP_{11} modes [89, 90]. These modal changes can modify the behavior of the resonances in a mechanical LPFG. As a result, multiple peaks can appear or disappear in the spectral transmission of the grating modifying its resonance wavelength range. The control of these spectral characteristics is of great importance in the design of all holey-fiber devices based on mechanical LPFGs. In this case, a characterization of the higher-order LP_{11} core mode resonances in these kind of gratings is required, principally in holey fibers that do not show a perfect arrangement of holes, which is the case of the great majority of microstructure fibers.

In this section, the higher-order core modes resonances in a mechanically induced long-period holey fiber grating (LPHFG) are characterized. Calculations based on a Fast-Fourier Transform (FFT) mode solver indicate that the resonances obtained in this work correspond to the odd- and even-LP_{11} higher-order core modes. On the other hand, the experimental results show that the resonances of these modes have a strong fiber-orientation dependency, which can be used to modulate the amplitude of the odd- and even-LP_{11} resonances according to the initial orientation of the holey fiber on the mechanical LPFG. In addition, an analysis of the twist response of both mode resonances is realized. Finally, the results obtained in this work can be generalized to other holey fibers that allow the coupling of the odd- and even-LP_{11} core modes in mechanically induced LPFGs.

3.2.1 Experiment and results

The experimental configuration shown in Figure (3.4) was used to produce the LPHFG. The grating was formed by pressing a section of a holey fiber between two corrugated grooved plates (CGPs). The dimensions of both grooved plates were 70 mm long and 24 mm wide and each one had a square groove pattern with 460 mm of period (Λ). The holey fiber was placed between the CGPs by two rotational holders H1 and H2. Both holders can be turned clockwise or anticlockwise, and their separation (L_{τ}) was 22.5 mm. When both holders are simultaneously turned in the same direction the holey fiber is rotated by an angle (θ) from a relative initial position with respect to the lateral stress axis generated by the CGPs. Additionally, the holey fiber can be twisted an angle (τ) if holder H1 is fixed and holder H2 is turned in a clockwise or counterclockwise direction, whereas the resonance wavelengths can be tuned changing the period (Λ) of the LPHFG by adjusting the angle (α) of the z-axis of the CGP with respect to the fiber axis as it is shown in Figure (3.4). A white light source (WLS) and an optical spectral analyzer (OSA) were used for the spectral measurements.

The inset in Figure (3.4) shows a photograph of the studied holey fiber which is the same as that used in the experiment described previously in Section 3.1. It is important to note that this fiber shows an imperfect hexagonal cladding structure.

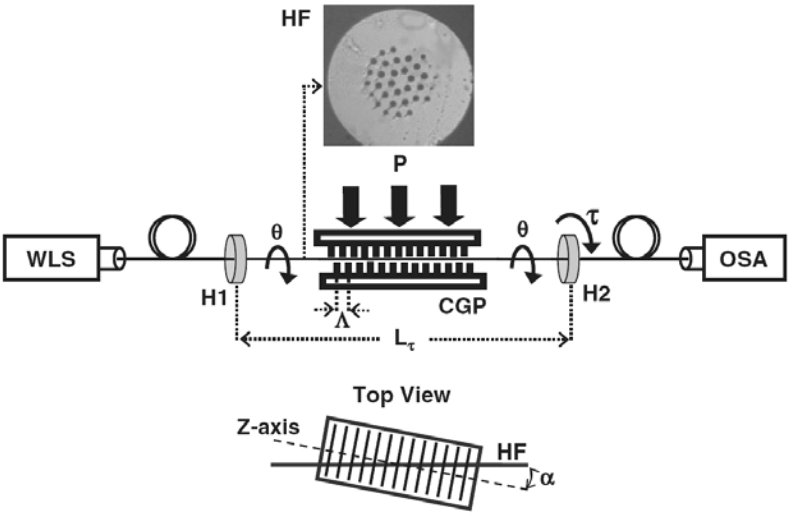

Figure 3.4: Scheme of the experimental mechanically induced long-period fiber grating setup.

In the experiment, we adjusted the period of the grating to 482 μm. Two rejection bands were obtained at 1121 and 1527 nm as it is shown in Figure (3.5). In this part, the holey fiber was rotated at different angles and, for each selected angle, it was pressed between both corrugated grooved plates. As it can be seen, both rejection bands depend strongly on the rotation angle of the fiber. In this experimental stage, we chose the initial position ($\theta = 0^0$) wherein only the rejection band at 1527 nm is observed. To analyze the tuning of the LPHFG, both rejection bands are plotted in Figure (3.6) for different values of Λ maintaining $\theta = 45^0$. In this case we always observed simultaneously both rejection bands over a tuning range of 100 nm, meaning that the grating period does not affect the behavior of the two mode couplings in the LPHFG.

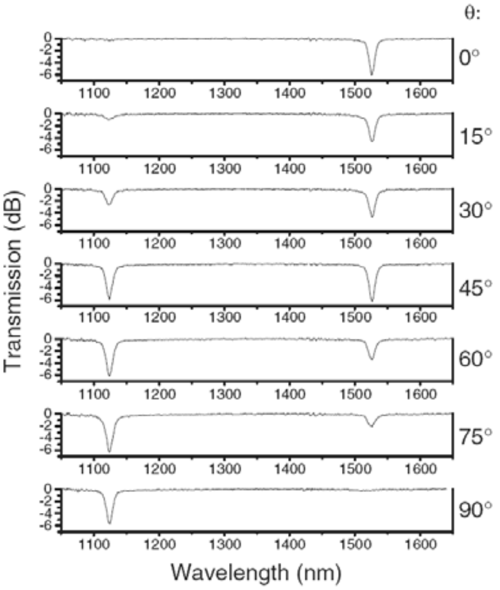

Figure 3.5: Transmission spectra of the LPHFG for different rotation angles θ at $\Lambda = 482\ \mu m$.

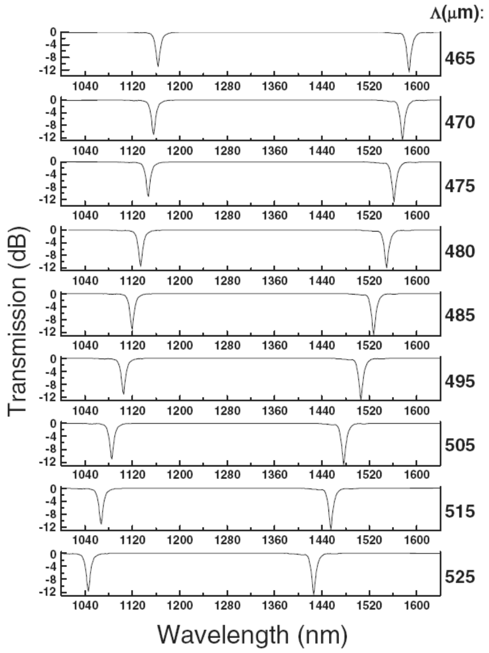

Figure 3.6: Tuning of the LPHFG rejection bands by adjusting the period Λ at $\theta = 45^0$.

To describe the modes associated with both rejection bands, a numerical simulation was performed. Figure (3.7) shows the resonance curves of the LPHFG obtained by simulation based on a FFT-mode solver [76, 77]. The solid lines are the theoretical resonant wavelength behaviors for the odd- and even-LP_{11} core modes according to the calculation of the effective index of the modes, while the circles are experimental data that correspond to the resonance wavelength tuning of each rejection band shown in Figure (3.6). According to these results, the modal coupling of the LP_{01} fundamental mode with the odd- and even-LP_{11} core modes of the holey fiber correspond to both rejection bands obtained at 1121 and 1527 nm, respectively. As it is mentioned above, the even- and odd-LP_{11} modes can be guided in holey fibers with low hexagonal symmetry. Figure (3.8) depicts the electric field and intensity distributions of the LP_{01} mode and the LP_{11} modes. In this figure, each LP mode has two eigen-polarization states and a birefringence with a numerical error of 1×10^{-6}. Additionally, one can observe that the LP_{11} modes have a set of symmetrical axes called optical eigen-axes [89] which are indicated by dashed lines in Figures (3.8)b and (3.8)c. The presence of these eigen-axes explains the behavior of the two rejection bands shown in Figure (3.5). According to this figure, we can obtain only one or simultaneously both rejection bands if the eigen-axes are or are not aligned with the pressing direction of the grooved plates.

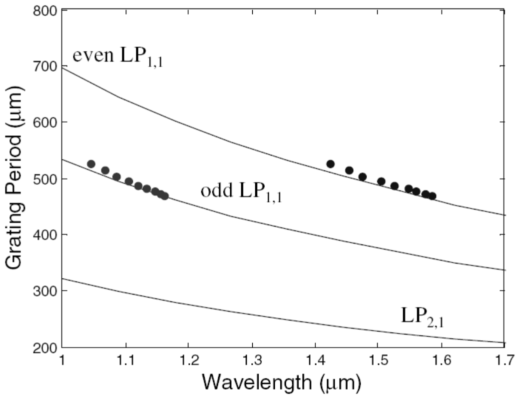

Figure 3.7: Calculated and measured resonant wavelengths of the mode coupling between the fundamental LP_{01} mode and odd-LP_{11} or even-LP_{11} core modes. Solid lines correspond to calculated curves and circles indicate measured data.

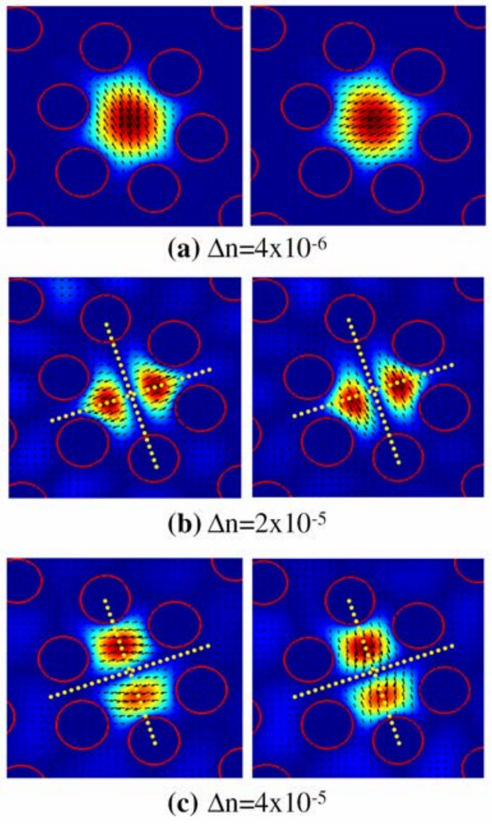

(a) $\Delta n=4x10^{-6}$

(b) $\Delta n=2x10^{-5}$

(c) $\Delta n=4x10^{-5}$

Figure 3.8: Calculated electric field distributions and birefringence Δn of (a) the LP_{01}, (b) the even-LP_{11}, and (c) the odd-LP_{11} core modes. Dashed lines indicate the eigen-axes of the LP_{11} modes.

Once the modal characterization of both rejection bands was realized, the twist effect in the spectral transmission of the LPHFG was analyzed. In this case, the holey fiber was first placed at $\theta = 0^0$ in such way that only the resonant peak at 1527 nm is obtained as is indicated in Figure (3.5) with $\theta = 0^0$. Then, the holey fiber was clockwise twisted along 22.5 cm length and was pressed between both corrugated grooved plates. This process was repeated for different values of twist: τ = 1, 5, and 9 turns. The result is the spectral transmission illustrated in Figure (3.9). One can observe that under twist both rejection bands at 1121 and 1527 nm are always obtained. These results indicate that the effect of the fiber rotation angle is reduced. This behavior is due to the fact that when the holey fiber is under twist there is not a preferential orientation of the fiber with respect to the pressure direction of both grooved plates. Also, one can observe that, after $\tau = 1$ turn, both rejection bands split into two shifted peaks that move symmetrically further apart as the twist is increased. This result does not depend on whether the fiber is twisted in a clockwise or counterclockwise direction. For higher values of twist no further measurements were made since the fiber was usually broken. Additionally, the pressure between the corrugated plates did not affect the splitting observed in Figure (3.9). The coupling strength was reduced or increased when a lower or higher pressure was applied and the rejection bands only decreased or increased in depth. Therefore, the twist is the origin of the splitting.

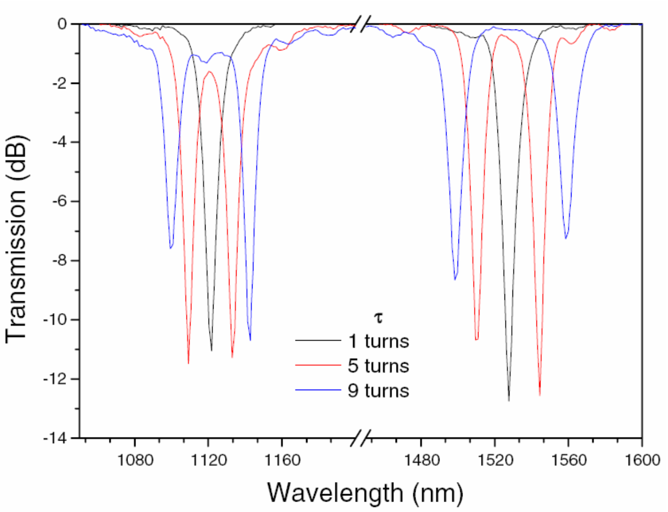

Figure 3.9: Splitting evolution for both rejection bands centered at 1121 and 1527 nm with $\tau = 1$, 2, and 3 turns per 22.5 cm.

Figure (3.10) shows the resonance wavelength evolution under twist from $\tau = 0$ to 9 turns for each rejection band observed in Figure (3.5) with $\theta = 45^0$. One can observe that with a twisting angle between 0 and 1 turn both rejection bands are obtained practically without change, and after 1 turn each band is split into two resonant peaks. For values of twist lower than 1 turn, not splitting of the resonant peaks is observed within the resolution of the OSA. In this case, the twist perturbation is not sufficient to clearly split each rejection band. These results change slightly for different values of θ. The upper and lower resonance wavelengths of the split resonance peak at 1527 *nm* show wavelength shift rates of 3.8 and -3.3 *nm/turn*. On the other hand, wavelength shift rates of 2.4 and -2.6 *nm/turn* were obtained for the split resonance peak at 1121 *nm*. These wavelength shift rates were calculated by linear regression of the data points shown in Figure (3.10). In this figure one can observe that the wavelength shift of both peaks of the split rejection band at 1527 *nm* show higher shift values that those in the split rejection band at 1121 *nm*. These differences are attributed principally to the fact that the odd- and even-LP_{11} modes associated with both split resonant peaks have different field distribution in the transverse direction of the holey fiber and they respond in different forms with respect to the twist perturbation.

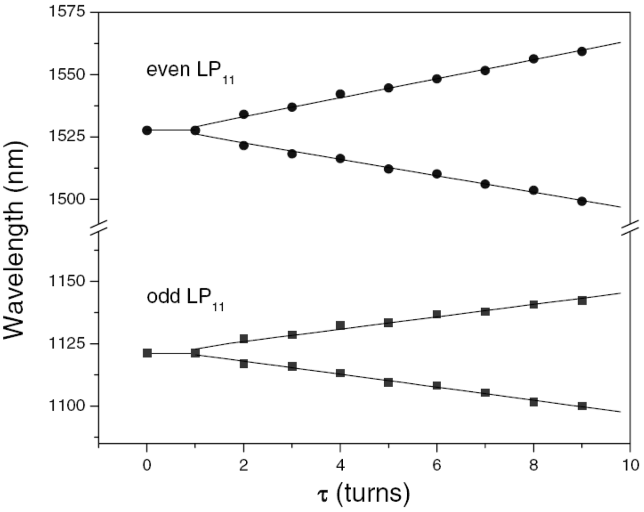

Figure 3.10: Wavelength shift of each resonant peak of the LPHFG under twist. Solid circles indicate measured data and solid lines are linear fitting.

Finally, to characterize the polarization response of the grating peaks, the rejection band of the LPHFG tuned at 1555 *nm* that corresponds to the even-LP_{11} mode resonance was analyzed. In this part, the white light source in the setup of Figure (3.4) was changed by a polarized light source. A polarimeter-synthesizer that works in the $1500 - 1600$ *nm* wavelength range was used. The spectral transmission of the LPHFG for both vertical and horizontal polarized inputs is shown in Figure (3.11)a, where one can observe that due to

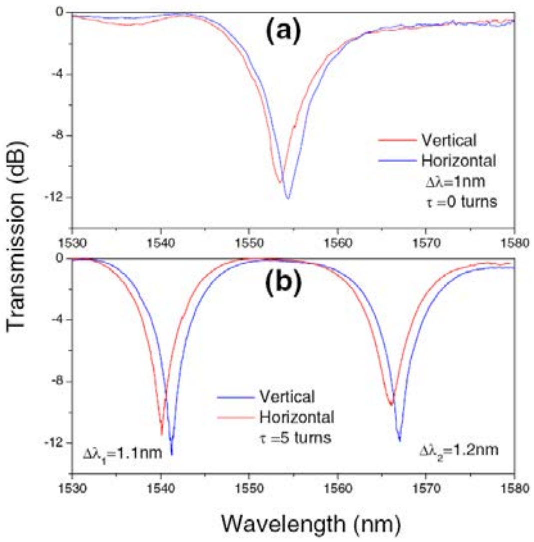

Figure 3.11: Polarization response of the even-LP_{11} resonance: (a) without twist, and (b) under twist.

the polarization dependence of the grating without twist, the localization of the resonant peak is changed 1 *nm*. Also, the polarization response of the rejection band under twist was measured. In this case, the holey fiber was twisted 5 turns in 22.5 *cm* length. In Figure (3.11)b, it can be observed that the localization of the two peaks of the split rejection band is changed 1 and 1.2 *nm*, respectively. These values are modified slightly for different values of twist. According to the birefringence of the LP modes obtained by simulation, we can expect wavelength shift values between 3 and 6 nm. These results do not agree with the measurements. In this case, the circular birefringence induced by twist and the linear birefringence caused by the directional mechanical pressure have to be considered.

3.2.2 Discussion

The analysis of higher-order core mode resonances in a LPHFG induced mechanically in an asymmetric holey fiber was presented. These higher-order core mode resonances are similar to those obtained in LPHFGs inscribed with electric arc [87]. The mode resonances obtained in this work correspond to the odd- and even-LP_{11} core modes. According to simulations based on a FFT-mode solver, these core modes can be propagated in the imperfect hexagonal structure of the holey fiber used in the experiment. One principal feature of these modes is that they show two perpendicular optical eigen-axes as it is indicated in Figure (3.8). These eigen-axes modify the resonance behavior of the LPHFG according to the rotation angle of the holey fiber with respect to the lateral stress axis. In this case, only one rejection band corresponding to the odd- or even-LP_{11} mode can be obtained if the eigen-axes of the odd- or even-LP_{11} mode is aligned with the pressure direction of the grooved plates, respectively. On the other hand, if the holey fiber is rotated 45 degrees from the above position, both mode resonances with similar depth can be obtained simultaneously. This behavior is attributed to the fact that the effective pressure of the grooved plates is distributed equally in both eigen-axes of the LP_{11} core modes. These characteristics are of great utility in the alignment of fiber devices; for example, the odd- and even-LP_{11} core modes can also propagate in polarization-maintaining holey fibers (PMHFs). In these fibers it is very important to know the direction of the birefringence axes. These axes can be associated with the eigen-axes of the odd- and even-LP_{11} modes. In this way, if one uses a mechanical LPHFG with an adequate grating period, one can determine according to the presence of the odd- or even-LP_{11} mode resonances whether the axes are aligned or not with respect to the pressure direction of both grooved plates. This scheme to determine the orientation of the birefringence axes of a holey fiber using a mechanical LPHFG is of great interest due to the simplicity and low cost of the device.

Additionally, it has been found that when the holey fiber is twisted slightly prior pressure application in the LPHFG, the odd- and even- LP_{11} mode resonances were obtained simultaneously. This behavior is attributed to the fact that when the holey fiber is twisted, there is not a preferential orientation of the fiber with respect to the pressure direction of the two grooved plates. In this way, the fiber rotation angle dependency of the LP_{11} mode resonances is reduced. However, for large values of twist, both LP_{11} mode resonances split in two peaks that move symmetrically further apart as the twist is increased. Also, the polarization response of the even-LP_{11} mode resonance under twist has been measured. The results show that both peaks of the split rejection band are shifted in the same direction for vertical and horizontal polarized inputs maintaining the splitting of the mode resonance. It is worth to mention that the splitting observed in both rejection bands shows a near linear behavior within a wide range of twist and it does not depend on the induced pressure. These splitting characteristics of the odd- and even-LP_{11} core mode resonances are of great interest in the design of band-pass filters with high tunability [91]. With these devices, one can modify the gain spectrum of an Ytterbium doped fiber in order to improve the generation of three-wavelength Raman fiber lasers. Additionally, these characteristics can be used to sense twist deformations in material structures based on LPHFGs induced mechanically in holey fibers [92].

3.2.3 Conclusions

A theoretical and experimental study of higher-order LP_{11} core mode resonances in a mechanically-induced long-period holey-fiber grating is presented. It has been found that these resonances depend strongly on the fiber rotation angle with respect to the lateral press-direction of the mechanical LPHFG. This dependency disappears when the holey fiber is slightly twisted because the effective pressure of the grooved plates is distributed in both directions of the eigen-axes of the odd- and even-LP_{11} modes. However, for large values of twist a splitting of both mode resonances is presented. This splitting is nearly linear within a wide twist range and does not depend on the twist direction or the initial orientation of the holey fiber. The splitting of both rejection bands is generated by removal of modal degeneracy. Also, higher values of splitting are obtained for the odd-LP_{11} mode resonance. These results are of great importance in the design of new all-fiber optical devices that involve couplings of odd- and even-LP_{11} core modes in asymmetric holey fibers.

3.3 Torsion sensing characteristics in LPFGs

As it was described in section 3.2, the twist effect in LPFGs inscribed in holey fibers could offer novel transmission characteristics such as the splitting of rejection bands. Nevertheless, a complete characterization of this novel spectral behavior in different holey fibers is required in order to improve their structural design for sensing applications based in long-period holey-fiber gratings.

In this section, the spectral transmission of a long-period holey-fiber grating induced mechanically in two different holey fibers is characterized. In the experiment, the twist sensitivity and tuning of the grating as well as its polarization response were analyzed. The holey fibers used in the experiment present different quality cladding structures; one with high uniform lattice in the cladding and another one with an asymmetrical lattice. In both cases, the results show that the rejection bands of the grating split when each holey fiber is twisted prior pressure application and the splitting observed grows linearly with the increment of the twist. Additionally, the results show that the shift sensitivity in the splitting depends directly of the holey-fiber structure.

3.3.1 Experiment and results

Two long-period holey-fiber gratings (LPHFGs) were formed using two different holey fibers. The LPHFG was induced similarly as it was described in Section 3.2.1 by pressing a section of holey fiber (HF) between two corrugated grooved plates (CGPs). In the same way, the dimensions of both grooved plates were 70 mm long and 24 mm wide and each one had a square groove pattern with 460 mm of period (Λ). The holey fiber was placed between the CGP by a fixed and rotational holder. In this way, the fiber can be twisted when the rotational holder is turned by an angle (θ). The separation between both holders is 22.5 cm. The resonance wavelengths can be tuned by adjusting the angle (α) of the fiber with respect to the z-axis of the CGP as it is shown in the top view of Figure (3.12). A white light source (WLS) and an optical spectral analyzer (OSA) were used for the spectral measurements. Additionally, a linear polarizing plate and the fluorescence of an ytterbium fiber laser (YFL) were included for the polarization spectra measurements. The photos in Figure (3.12) show the transversal structures of both holey fibers used in the experiment. The holey fiber called 2 is the same fiber used in Section 3.1 and 3.2 with a core/cladding diameter of 11/125 μm, with 5 μm hole diameter and lattice pitch of 11 μm. This fiber shows an asymmetry in its cladding structure. The holey fiber called 3 is a commercial holey fiber F-SM10 that has a core/cladding diameter of 10/125 μm, with 3.5 μm hole diameter and lattice pitch of 3 μm and shows an almost perfect hexagonal arrangement of holes without asymmetry in its cladding.

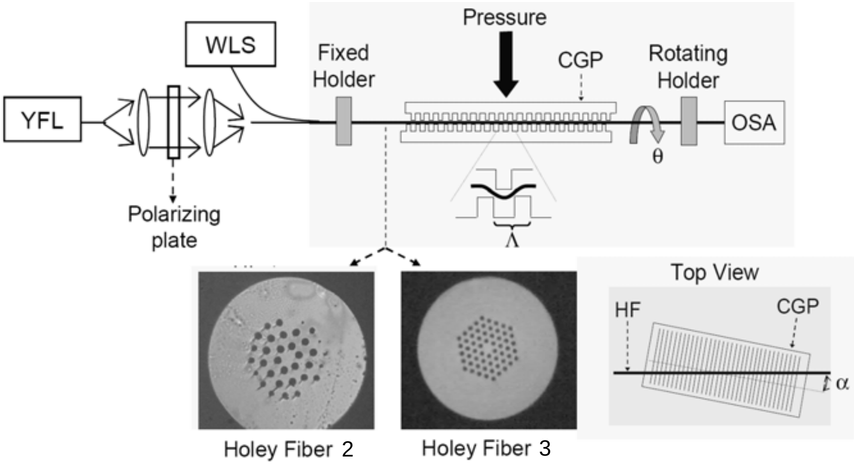

Figure 3.12: Scheme of the experimental mechanically induced LPHFG set up under torsion.

In the experiment, the rejection bands of the LPHFG inscribed in fiber 2 were first analyzed. In this case, the period was adjusted to 482 μm. Two rejection bands were obtained at 1121 and 1527 nm as it is shown in Figure (3.13)a. To characterize the twist effect in the LPHFG, the holey fiber was clockwise twisted in 22.5 cm length and then, it was pressed between both corrugated grooved plates. This process is repeated for different values of twist from 2 to 9 turns. The result is the spectral transmission illustrated in Figures (3.13)b-i. The same experiment process is repeated with the LPHFG inscribed in fiber 3. In this case, the period was adjusted to 460 μm and one rejection band at 1103 nm was obtained as is shown in Figure (3.14)a. The results of the spectral characterization for different values of twist from 9 to 16 turns are illustrated in Figures (3.14)b-i. For higher values of twist no more measurements were made due to that both holey fibers are usually broken. One can observe in Figures (3.13) and (3.14) that all rejection bands split in two shifted rejection bands that move symmetrically further apart as the twist is increased. Additionally, for both holey fibers, a clear splitting of rejection bands is observed after a specific amount of turns: after 1 turn for fiber 2 and after 9 turns for fiber 3. For lower values of turns, the twist perturbation is not sufficient to split each rejection band more than 0.1 nm which corresponds to the wavelength resolution of the OSA. In similar way to Section 3.2, the twist is the origin of the splitting.

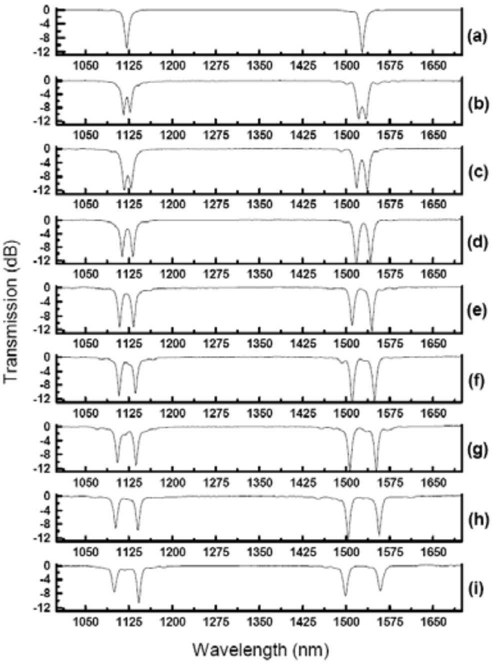

Figure 3.13: Splitting evolution for both rejection bands centered at 1121 and 1527 nm associated to fiber 2 and with a) 0, b) 2, c) 3, d) 4, e) 5, f) 6, g) 7, h) 8, and i) 9 turns per 22.5 cm.

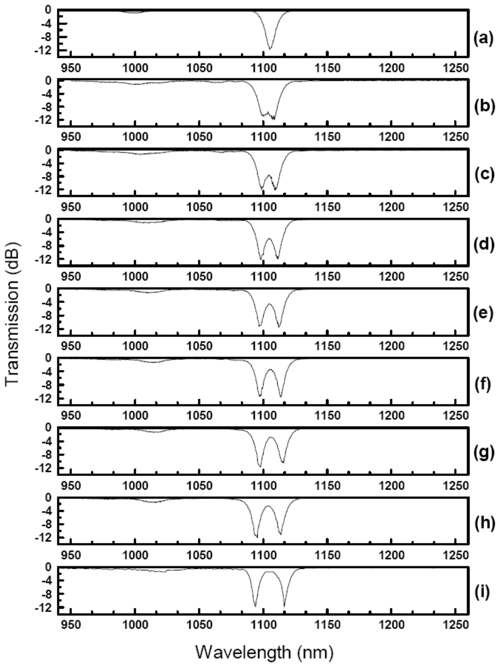

Figure 3.14: Splitting evolution for the rejection band centered at 1103 nm associated to fiber 3 and with a) 0, b) 9, c) 10, d) 11, e) 12, f) 13, g) 14, h) 15 and i) 16 turns per 22.5 cm.

Figure (3.15) shows a plot of the splitting as a function of the twist for each rejection band obtained with both holey fibers 2 and 3. The splitting values were obtained considering the wavelength separation of each rejection band observed in Figures (3.13) and (3.14). One can observe with more clarity that the splitting response of all rejection bands is near linear within the twist values used in the experiment and each one exhibits different twist sensitivity. In the case of fiber 2, the differences observed in the rejection bands localized at 1527 and 1121 nm are attributed to the different modes coupled in these resonance wavelengths. On the other hand, the different twist sensitivities observed in the rejection bands associated to each holey fiber are attributed principally to the different transversal structures of fibers 2 and 3 respectively. According to our results, for fiber 2 we can obtain a splitting of 62.5 nm corresponding to a maximum twist of 9 turns (twist rate of 2.5 rad/cm) and, for fiber 3 we can obtain a splitting of 22.5 nm for a maximum twist of 16 turns (twist rate of 4.5 rad/cm). These splitting values are higher than those reported in other works for LPHFGs induced mechanically in standard fibers where splits of $10 - 20$ nm are obtained for a twist rate of 10 rad/cm [93, 94].

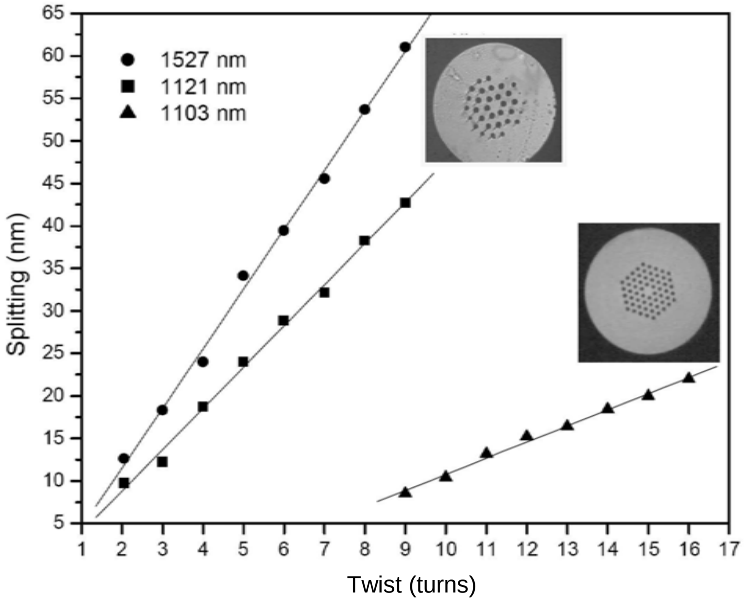

Figure 3.15: Splitting of rejection bands localized at 1527 and 1121 nm for fiber 2 and at 1103 nm for fiber 3. Solid symbols indicate measured data and solid lines are fitting lines.

To analyze the tuning of the LPHFG under twist, the split rejection bands of the grating inscribed in fibers 2 and 3 for different values of the grating period are plotted in Figures (3.16) and (3.17). For fibers 2 and 3, a twist of 7 and 16 turns are kept respectively. In these figures, one can observe that the splitting is not modified by tuning. It means that for both holey fibers the splitting does not depend of the grating period at least over a tuning range of 100 nm. This behavior is also observed for different values of twist. All these tuning characteristics are of great interest in the design of tunable band-pass filters, optical fiber switches and torsion fiber sensors.

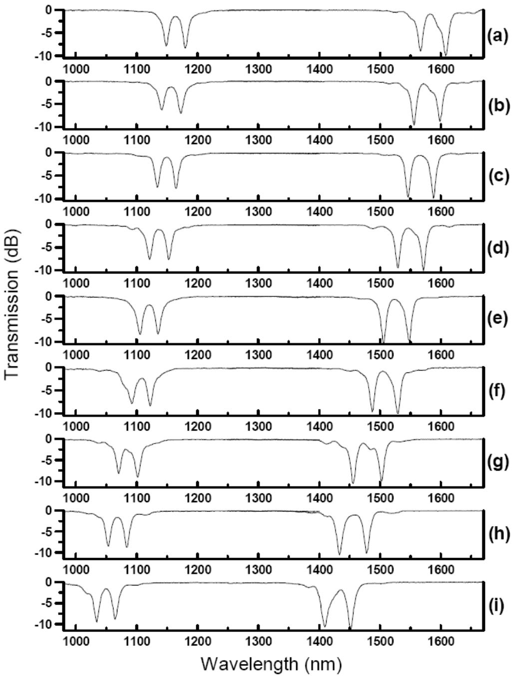

Figure 3.16: Tunable rejection bands of fiber 2 with 7 turns of twist at different grating periods: a) 0.465, b) 0.470, c) 0.475, d) 0.480, e) 0.485, f) 0.495, g) 0.505, h) 0.515 and i) 0.525 *mm*.

Finally, the polarization response of the mechanically-induced LPHFG was characterized. The rejection bands tuned at 1080 for fibers 2 and 3 were analyzed respectively. In this experimental part, the white light source in the setup of Figure (3.12) was replaced by the fluorescence of an ytterbium fiber laser. The polarization response of the rejection bands in both holey fibers without twist is shown in Figures (3.18)a and b. In these figures it is observed that when the input polarization is changed from vertical (V), which coincides with the pressure direction of the grooved plates, to horizontal (H), each resonant peak is shifted 1.3 and 0.6 *nm* for fibers 2 and 3. On the other hand, Figures (3.19)a and b show the polarization response of each split rejection band for fibers 2 and 3 maintaining a twist of 4 and 15 turns in each holey fiber respectively. In these figures, one can observe that both peaks of each split rejection band are shifted $1.2 - 1.3$ *nm* for fiber 2 and $0.8 - 0.7$ *nm*

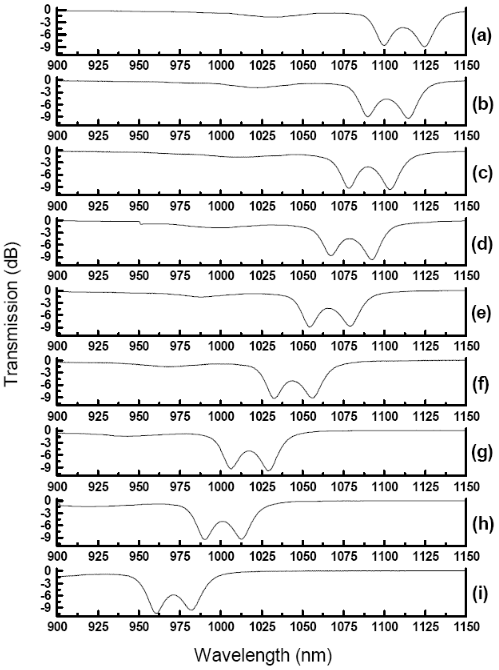

Figure 3.17: Tunable rejection band of fiber 3 with 16 turns of twist at different grating periods: a) 0.460, b) 0.465, c) 0.470, d) 0.475, e) 0.480, f) 0.485, g) 0.490, h) 0.495 and i) 0.500 *mm*.

for fiber 3. In all cases, the rejection bands obtained with fiber 2 show higher polarization response. It is worth to mention that both peaks of each split rejection band shown in Figures (3.19)a and b are shifted in different way. In Figure (3.19)a, both peaks are shifted in the same direction while, in Figure (3.19)b those peaks are shifted in opposite directions. This behavior can be attributed to a combination of the intrinsic linear birefringence of each holey fiber, the circular birefringence induced by twist and the linear birefringence generated by the pressure of both grooved plates. Nevertheless, due to its complexity, these parameters will be analyzed in a future work.

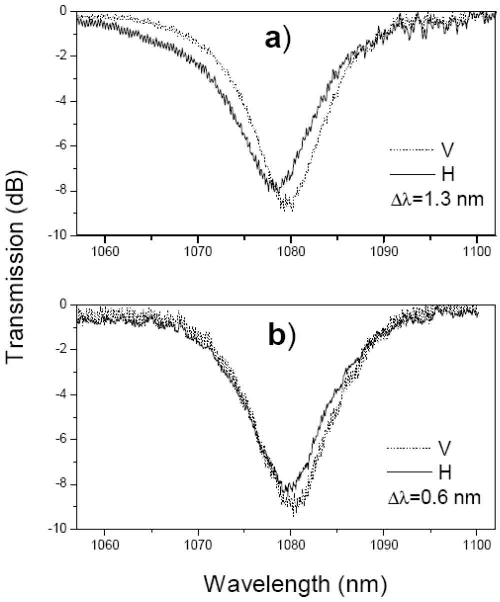

Figure 3.18: Polarization response of the rejection bands in: a) fiber 2 and b) fiber 3 with zero turns of twist.

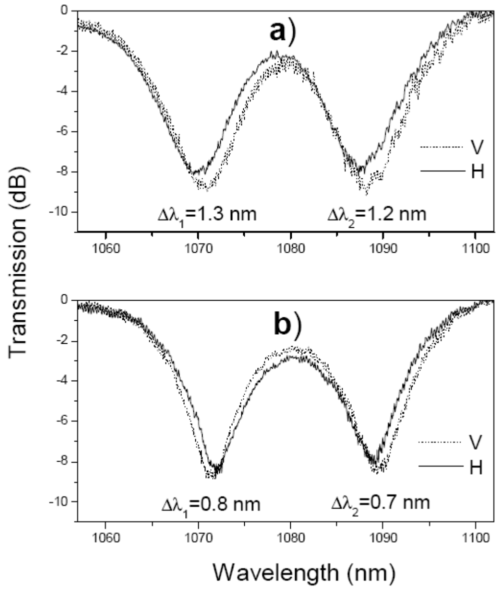

Figure 3.19: Polarization response of the rejection bands in: a) fiber 2 with 4 turns and b) fiber 3 with 15 turns of twist respectively.

3.3.2 Discussion

As presented above, the introduction of certain level of twist in two different holey fibers prior pressure application in a mechanically induced long-period holey-fiber grating generates the splitting of the usual rejection bands in two shifted bands that move symmetrically further apart as the twist is increased. The splitting can be explained if we consider that the coupled modes of the rejection bands in a mechanically induced LPHFG correspond to the LP_{01} core mode and the LP_{1n} cladding modes (where n is an integer number). The LP_{01} fundamental mode is degenerated by two circularly polarized modes ($HE_{\pm 11}$) whereas the LP_{1n} mode is degenerated by two circularly and one linearly polarized modes ($HE_{\pm 21}$, TM_{0n} or TE_{0n}). In this nomenclature, the sign ± in the azimuthal numbers indicates the right and left directions of the circularly polarized HE modes. Additionally, if a certain value of twist is applied to the fiber, a circular birefringence is induced. This birefringence shows opposite signs for both right- and left- circularly polarized HE modes [94]. Therefore, both right- and left- HE modes will have different propagation constants and the modal degeneration of the HE, TM and TE modes will be broken. As a result, the mode coupling between the fundamental core mode and the LP_{1n} cladding modes is modified. If one considers only the positive sign of the azimuthal number of the HE modes, one can infer that the HE_{+11} core mode is coupled with the HE_{+2n} cladding mode (which has the same circular polarization) and with the linear polarized cladding mode (TM or TE). Then, two mode couplings are formed instead of one. This behavior is also followed by the HE modes with negative azimuthal numbers; nevertheless, an overlapping with the previous case is presented and only two peaks corresponding to both mode couplings are observed.

On the other hand, the results show that the splitting observed in Figures (3.13) and (3.14) does not depend on the induced pressure. This independence indicates that the splitting is not result of the combined effects between microbending and twist perturbation. Therefore, the only origin of the splitting is the induced twist. Additionally, in Figure (3.15), the graphs show a linear behavior of the splitting within a wide twist range and it does not depend on the holey fiber used in the experiment. Also, if we consider the transversal structure of the holey fiber, one can infer qualitatively that the different twist sensitivities shown in Figure (3.15) for fibers 2 and 3 are attributed to the fact that in fiber 2 the modes are almost degenerated because it shows an imperfect hexagonal arrangement of holes [79] and, in this case, it is easier to remove the quasi-degeneracy by twist. Therefore, the fiber 2 can show higher twist sensitivity than that in fiber 3 or standard single mode fibers. On the other hand, in Figures (3.16) and (3.17), one can observe that the split resonant peaks can be tuned in a wavelength range of at least 100 nm for both holey fibers with negligible changes in their wavelength separation. It confirms that the splitting does not have a strong dependence with wavelength within this tuning range.

According to the splitting results shown in Figure (3.15), the maximum shift of the peaks at 1527 nm in the fiber 2 was 31 nm for a twist rate of 2.5 rad/cm. It corresponds to a twist sensitivity of 12.4 $nm/(rad/cm)$. This sensitivity is between 3 to 5 times higher than that obtained in LPFGs induced in standard fibers by mechanical pressure, CO_2, UV and arc electric [95, 24, 96, 97, 93]. In these works, twist sensitivities of $1-5$ $nm/(rad/cm)$ have been reported. On the other hand, if one considers corrugated LPFGs in standard fibers, the twist sensitivity of these gratings can be 10 times higher than that obtained in this work [98]. Nevertheless, as it is shown in Figure (3.15), an irregular cladding structure like the holey fiber 2 can increase the twist sensitivity of the LPHFG more than 10 times respect to fiber 3 with almost perfect cladding structure. Therefore, if an optimization process of the cladding structure is realized in order to obtain a higher value of twist sensitivity, one can expect to obtain similar values than those reported in corrugated LPFGs with the additional advantage of offering a more robust configuration.

Finally, the polarization response of the grating inscribed in both holey fibers were measured. The results in Figures (3.18) and (3.19) shows that the rejection bands in fiber 2 have higher polarization dependence than that in fiber 3. This behavior varies slightly for different values of twist and it does not depend on either if the fiber is twisted in clock- or anticlok-wise. This result agrees with the fact that the transversal structure of the fiber 2 shows an asymmetric microstructure cladding and, consequently, a higher linear intrinsic birefringence. On the other hand, it is worth to mention that, in some applications, this polarization dependence is not attractive in devices based in LPFGs; nevertheless, it is possible to find alternative experimental setups that can reduce or eliminate this polarization response [99].

3.3.3 Conclusions

The spectral behavior of two LPHFGs induced mechanically in different twisted holey fibers were analyzed. The results show a splitting of the rejection bands that grows linearly with the twist ratio. The splitting does not depend on the twist direction, the mechanical pressure and modifications of the grating period. This splitting is attributed to the removal of modal degeneracy by twist perturbation in both holey fibers. Additionally, the grating inscribed in fiber 2 shows higher twist sensitivity and polarization response than that of fiber 3 and it is caused by the asymmetry of its cladding structure. Moreover, the values of twist sensitivity obtained with fiber 2 is higher than that obtained with LPFGs induced in standard fibers by mechanical pressure, CO_2, UV radiation, and electric arc. These results are of great interest in the design of new torsion sensors based in long-period holey-fiber gratings.

$\boxed{4}$ Applications

In this Chapter, direct applications of the results described in Chapter 3 are given by means of three works. In these works, new schemes to perform fiber lasers and all-fiber devices are proposed. First, a bandpass filter with adjustable bandwidth is described, then, the performance of a tunable fiber laser and a simultaneous three-wavelength fiber laser are presented.

4.1 Band-pass filters with adjustable bandwidth

In this section, a bandpass filter with adjustable bandwidth based on a press-induced long-period grating in a twisted holey fiber is presented. By twisting the holey fiber prior to the application of spatial periodic pressure, each rejection band of the non-twisted induced long-period grating is split into two shifted rejection bands that move further apart as the twist ratio increases. This feature results in a wide bandpass filter with controllable bandwidth. A bandpass filter at 1523 nm with adjustable bandwidth from 15 to 65 nm with near-linear response and insertion loss lower than 0.7 dB is demonstrated. Additionally, the bandpass filter can be tuned over 100 nm.

4.1.1 Introduction

All-fiber bandpass filters are devices required in applications for spectral equalization or shaping [100, 101]. So far, two typical configurations have been demonstrated to obtain bandpass filters based on long period fiber gratings (LPFGs). One approach uses a pair of LPFGs in cascade with a core blocker between them; the first LPFG couples the light from the core to the cladding, and the second couples light back to the core; meanwhile, the core blocker intercepts the core mode transmission and ensures that the core signal after the cascade comes totally from the recoupled cladding modes [101, 102, 103]. The other option is the π-phase method, in which a π-phase shift is introduced during the LPFG periodicity inscription so that the destructive mode coupling is converted into constructive mode coupling and a bandpass filter is obtained [104]. The main limitation of the first proposal is the relative high insertion loss (> 1 dB); meanwhile, the other one has simple fabrication but shows poor flexibility in the bandpass filter parameters. To obtain flexible bandpass filters based on LPFGs it is important to explore and propose other novel configurations. Under this concept, a bandpass filter with controllable bandwidth based on a press-induced long-period holey fiber grating (LPHFG) is presented.

4.1.2 Experimental setup

A schematic diagram of the bandpass filter based on the press-induced long-period twisted holey-fiber (HF) grating is shown in Figure (4.1). This setup is similar to that described in Section 3.2. Two identical metallic corrugated plates of 70 $mm \times 25\ mm \times 10\ mm$ (length × width × thickness) with a grooved pattern were used to generate the periodic index modulation over the twisted HF by pressure (P). The grooved pattern has a period of $\Lambda = 460{\pm}10\ \mu m$, a duty circle of 48%, and a depth of $400{\pm}10\ \mu m$. The period of the grating may be adjusted by the rotary stage (RS) according to the expression $\Lambda = (460{\pm}10)/cos(\phi)$, where ϕ is the rotational angle of the grooved plates with respect to the fiber, while the length of the grating is determined by the interaction length of the plates. The HF under test was fixed to one side by a fixed fiber fastener (FFF), and the other fiber side was fixed to a rotational fiber fastener (RFF) with a separation length (L_τ), of 22 cm, where the HF can be twisted by turning the RFF. The inset in Figure (4.1) shows a photograph of the transversal structure of the HF used in the experiment which corresponds to the holey fiber 2 shown in Figure (2.9). To measure the transmission spectrum of the press-induced LPHFG under controlled twist, a white light source (WLS) and an optical spectral analyzer (OSA) were used.

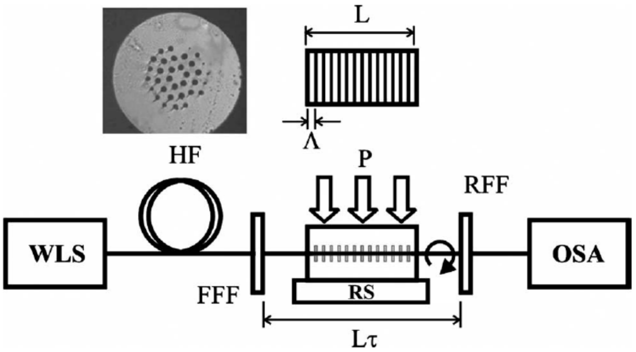

Figure 4.1: Experimental setup of the press-induced LPHFG under twist. Abbreviations defined in text.

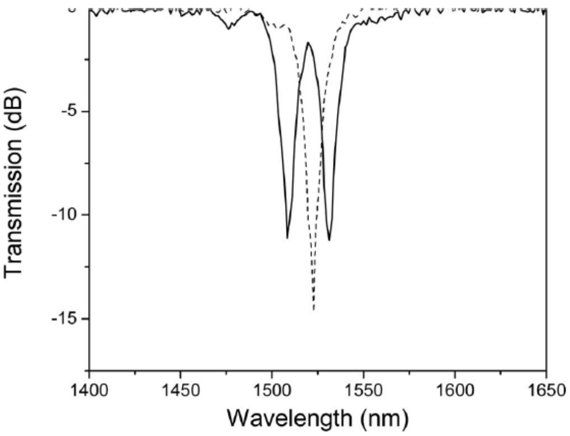

Figure 4.2: Transmission spectra of the rejection filter (dotted curve) and the bandpass filter (solid curve) induced by twist.

4.1.3 Results and discussion

First, the HF was placed between the plates and fixed with the fiber fasteners, and then a $485\mu m$ period was selected and the pressure between the metallic plates was adjusted until a rejection band filter at 1523 nm, with 15 dB notch depth and a bandwidth of 9 nm, was obtained (dotted curve in Figure (4.2)). Then, without applied pressure the HF was twisted 4 turns clockwise, and pressure was gently applied again. Afterwards, the normal rejection band filter was split into two symmetrically shifted rejection bands, which results in a bandpass filter with an insertion loss of 1.8 dB (solid curve in Figure (4.2)). It is worth mentioning that for a twist less than 3 turns, the separation between the shifted rejection bands was not enough to obtain a bandpass filter with insertion loss lower than 3 dB. This proof was repeated for a twist of 4 turns, and negligible differences in the split of the rejection band and wavelength separation of the shifted rejection bands were observed. In the same way, the other rejection band simultaneously obtained at 1118 nm exhibited similar splitting behavior as described above.

Figure (4.3) shows the evolution of the transmission spectrum of the bandpass filter when the twist ratio increases from 4 to 12 turns. The bandpass filter shows a broadening of the bandwidth and a reduction of the insertion loss as the twist ratio increases. The inset in Figure (4.3) shows a plot of the bandwidth broadening of the transmission bandpass as a function of the twist ratio, where we can observe a near-linear dependence. The bandwidth of the bandpass filter rises from 15 nm at 4 turns to 65 nm at 12 turns; meanwhile, the insertion loss decreases from 1.8 to 0.7 dB after 6 turns. For more than 12 turns the HF was regularly broken, and we cannot increase the bandwidth more than 65 nm. Moreover, the bandpass filter can be tuned by changing the period of the index modulation over the twisted HF, as it is shown in Figure (4.4), where the bandpass filter is tuned from 1565 to 1465 nm. Also, the transmission amplitude of the bandpass filter shown in Figure (4.5) can be controlled by adjusting the broadening of the shifted resonance bands by means of the interaction length of the grooved plates over the twisted HF. Figure (4.5) shows the attenuation of the transmission amplitude of the bandpass filter when the interaction length

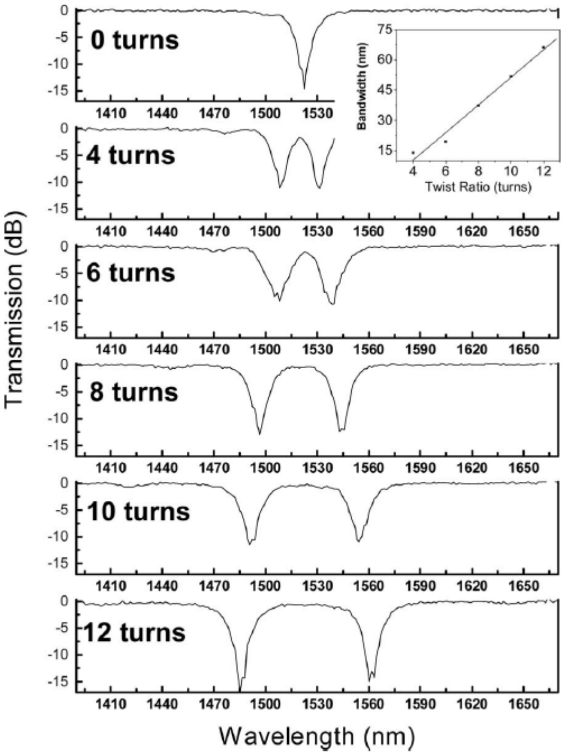

Figure 4.3: Spectral evolution of the bandpass filter for different twist ratios of the LPHFG.

decreases from 63.5 to 43 mm. The amplitude of the bandpass filter can be adjusted by this method; meanwhile, the bandwidth of the bandpass filter stays lower than two times the bandwidth of the split rejection bands. The inset in Figure (4.5) shows the transmission amplitude as a function of the length of the plates over the HF.

Experimental reports on corrugated and CO_2-impressed long-period gratings (LPGs) in standard fiber under slight twist ($< 0.2\ rad/cm$) have shown that their cladding mode resonances shift linearly to shorter or longer wavelengths depending of the twist direction [105, 106]. Recently, unexpected effects have been observed when the mechanically induced LPGs are under twist. The simultaneous application of lateral press and twist results in the shift of the cladding mode resonances to shorter wavelengths and after a certain level

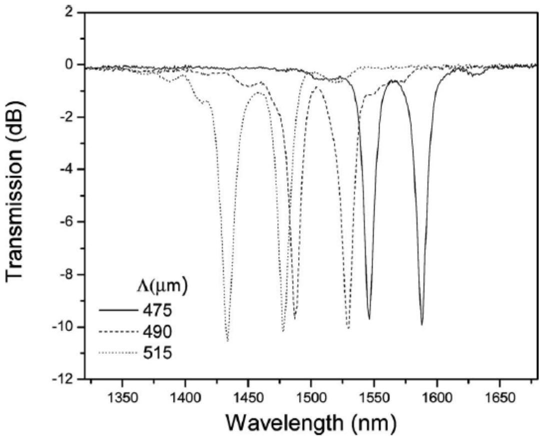

Figure 4.4: Wide tuning range of the bandpass filter for different grating periods of the LPFG.

of twist ($> 5\ rad/cm$) a split of the cladding mode resonances is observed [93]. In contrast, we have found that mechanically induced LPGs in the HF under twist exhibit a split of the cladding mode resonances for twist ratios $< 2\ rad/cm$, where the value of the split has a near linear dependence on the twist ratio applied to the HF.

Based on the coupling mode theory, Ivanov [94] demonstrated that the twist applied in LPGs in standard fiber removes the degeneracy of the hybrid modes of the long-period modes, and consequently splitting of the mode resonances is observed. The calculated and experimental split sensitivities to twist for standard single mode fibers are of the order of $12\ nm/(rad/cm)$ [93, 94], while in our case the split sensitivity is $\sim 18\ nm/(rad/cm)$, i.e., ~ 10 times larger than in standard fibers. This significant difference is expected since the magnitudes of the effective index changes in the core and the air silica microstructured cladding are different. In the case of LPGs based on standard fiber, under a slight twist, the index changes of the core and the cladding are approximately similar, and it is not enough to break the degeneracy of the hybrid mode of the corresponding cladding mode resonances so that only the wavelength shift is observed. Hence, the standard fiber requires a larger twist ratio to break the hybrid mode degeneracy and bring about the onset of mode

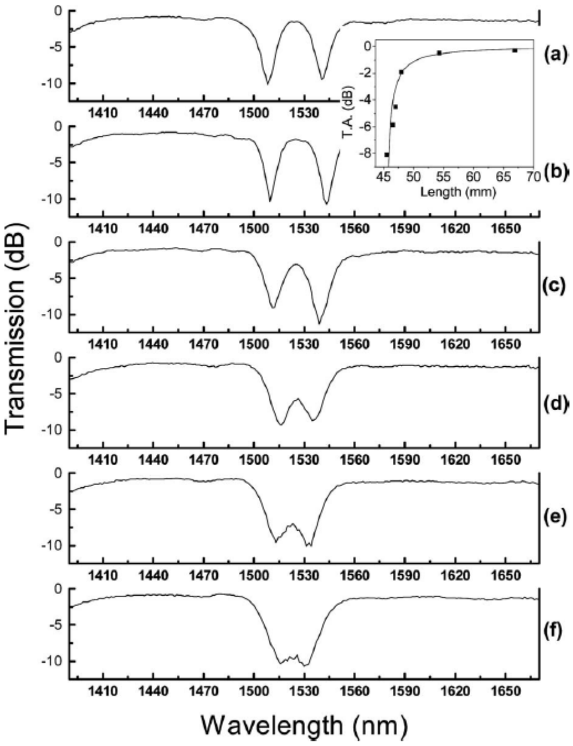

Figure 4.5: Transmission amplitude as a function of the wavelength for the following interaction length of the press-induced LPHFG: (a) 63.5, (b) 51.5, (c) 45.5, (d) 44.5, (e) 44, (f) 43 *mm*.

splitting. In addition, the HF presents irregularities in the photonic crystal structure that contribute to the reduction of the degeneracy of the hybrid modes.

4.1.4 Conclusions

In summary, a novel bandpass filter with adjustable bandwidth was presented based on the split of a rejection band of a press-induced LPFG over holey fiber when the fiber is subjected to controlled twist. We have demonstrated a bandpass filter with insertion loss less than 0.7 dB and adjustable transmission bandwidth from 15 to 65 *nm* that is tunable over a range of 100 *nm*. An important advantage of the proposed bandpass filter compared with other methods is the flexibility to independently adjust the bandwidth, the tunable range, and the transmission amplitude with relative low insertion loss.

4.2 Tunable Ytterbium-doped fiber laser

In this section, a tunable double-clad Ytterbium-doped fiber laser is described. It is based on a long-period fiber grating mechanically-induced in a section of a single mode holey fiber inserted into the laser cavity. The mechanically-induced long-period holey fiber grating acts as a wavelength-selective fiber filter whose central wavelength, linewidth, and strength can be tuned by changing the period, the length of the grating, and the applied pressure. This work was performed in collaboration with Dr. Gilberto Anzueto Sánchez during his PhD studies at CIO.

4.2.1 Introduction

The search for simple and cost effective techniques for wavelength tuning of fiber lasers is a subject of continued interest. Fiber lasers offer broad absorption and emission wavelengths, and the possibility of obtaining high output laser power when a double clad geometry is used. The wavelength tuning in fiber lasers can be realized by external dispersive bulk elements [107, 108], or in-line fiber elements [109, 110]. Tunable fiber lasers based on bulk elements require complicated arrangements which require expensive devices. Consequently, all-fiber systems are advantageous since they do not require free-space components. One of the techniques used for all-fiber wavelength tuning is based on the insertion of in-line band-rejection filters into the laser cavity. In this case, the position of the stop band is selected such that it precludes oscillation at that particular wavelength range, modifying the overall gain spectrum of the laser cavity and allowing lasing at the resultant preferential wavelength. On the other hand, long-period fiber gratings (LPFGs) have demonstrated their versatility as wavelength optical filters for applications where the equalization of the gain spectrum of doped fibers is required [111, 112]. Mechanically induced LPFGs that offer the advantages of broad tuning and the capability of being erased and reconfigured [113], are particularly useful for these applications. Several techniques of mechanically induced tunable LPFGs have been reported in standard communication fibers and holey fibers, where grooved plates (GPs), strings, and springs have been used to apply periodical mechanical stress on the optical single mode fiber to induce an effective index modulation [114, 115]. In this respect, holey fibers have shown an enhanced sensitivity to mechanical pressure that makes them suitable for implementation in tunable LPFGs. Consequently, a tunable double clad Ytterbium-doped fiber (DCYDF) laser is presented, where a mechanically induced band rejection filter in a holey fiber is inserted into the laser cavity as the wavelength selective element. The adjustment of the grating period allows a change in the spectral position of the notch, while the pressure variation provides control of the strength of the notch. By adjusting the period of the mechanical pattern and the applied pressure on the holey fiber respectively.

4.2.2 Experimental setup

Figure (4.6) shows the experimental setup of the tunable fiber laser. It consists of 30-m-long DCYDF with core/cladding dimensions of 6/125 mm, and 0.14/0.45 of numerical aperture, and absorbtion of 0.2 dB/m at 915 nm . Figure (4.7) shows the cross section of the DCYDF. This fiber is end-pumped by a 915 nm pigtailed diode laser connected to a fiber collimator via an SMA (SubMiniature version A) adapter. The collimated pump is coupled to the input end of the DCYDF by an aspheric lens. Between the fiber collimator and the aspheric lens there is a 45^0 dichroic mirror with a high transmission at the pump wavelength and a high reflection from $\sim$ 1050 to 1100 nm, which prevents back reflection to the pump diode and serves as output coupler for the laser signal. The other end of the DCYDF is spliced to a 60-cm-length single mode holey fiber which has a core/cladding diameter of 11/125 mm. The holey fiber and the LPHFG setup used in this work are the same described in Figure (3.1) of Section 3.1. According to the LPHFG design described in Section 3.1, it allows the change of the grating period (Λ) by adjusting the circular bending radius (R) of the holey fiber. Therefore, the center wavelength of the notch is adjusted by changing the period of the LPHFG and the depth of the notch depends directly on the pressure of the flat plate. In this way, the fiber laser cavity is defined by the DCYDF, the spliced holey fiber, and each of the two perpendicular cleaved ends at the sides of the cavity gives $\sim 4\%$ of Fresnel reflection. The output laser light is detected from the output end of the holey fiber and the reflected light at the dichroic mirror.

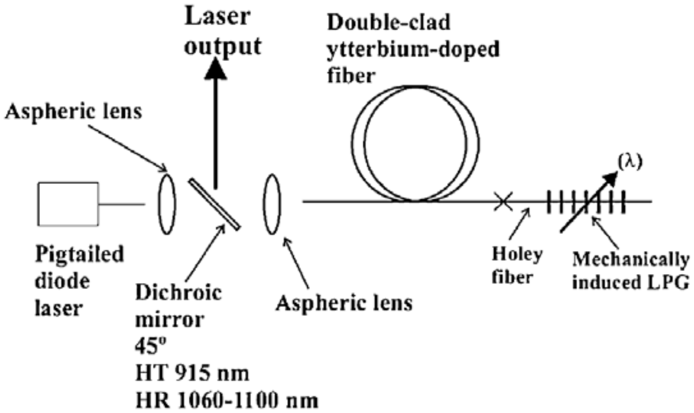

Figure 4.6: Experimental setup of the tunable laser based on a LPFG induced mechanically in a PCF.

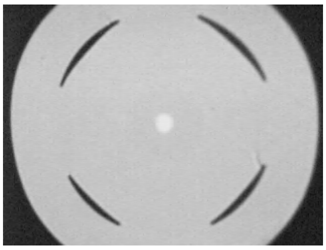

Figure 4.7: Cross-section of the double-clad Ytterbium-doped fiber used in the experiment. This fiber was fabricated with the participation of Dr. Alejandro Martínez in Lasersharp Inc.

4.2.3 Results and discussion

Figure (4.8) shows the experimental white light transmission spectra of the LPHFG at three different center wavelengths, 1080.6 (solid curve), 1084.8 (dashed curve), and 1091.4 *nm* (dotted curve), which corresponds to grating periods of approximately 603, 600, and 595 μm, respectively. As it was mentioned, the center wavelength of the notch is reduced as the grating period is increased, while a change in the number of periods varies the bandwidth of the notch and variation of the applied pressure changes the depth.

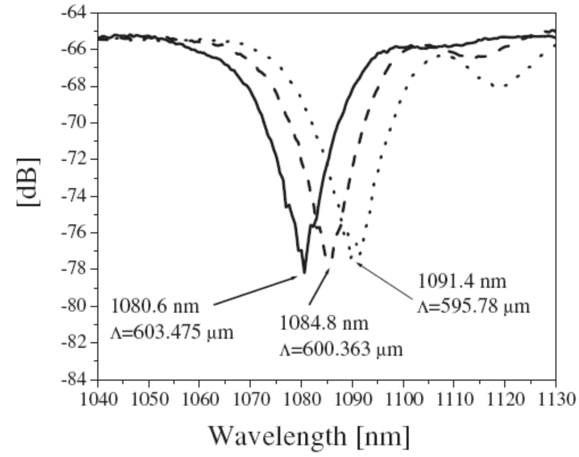

Figure 4.8: White light transmission spectra of the LPHFG for three different grating periods.

The fiber laser was first operated as a free-running fiber laser without the holey fiber spliced to the DCYDF. Under these conditions the laser operated at a wavelength of 1089 *nm* with a threshold pump power of 131 *mW* and 61.52% of slope efficiency with respect to the launched pump power. When we spliced the piece of holey fiber to the DCYDF, the threshold pump power increased up to 324 *mW*, while the slope efficiency decreased to 27.1%. From these data, we estimated the splice loss between the DCYDF and the holey fiber plus the intrinsic holey fiber losses as ≈ 3.97 dB. As we will see, when the holey fiber is under pressure, there is an increase in the loss which further reduces the laser efficiency.

The dotted line in Figure (4.9) shows the transmission spectrum of the LPHFG when the center wavelength and the depth of the notch are 1089.6 *nm* and 16 dB, respectively. As it can be observed, the effect of the LPHFG is to introduce an excess loss around the peak fluorescence, thus modifying the original spectrum (dashed line in Figure (4.9)), so that the wavelength at which the gain is maximum is altered. This results in a different free-running laser wavelength. By varying slightly the position of the center wavelength of the notch, we were able to tune the fiber laser in a range of 12.6 *nm*, from 1079.4 to 1092 *nm*.

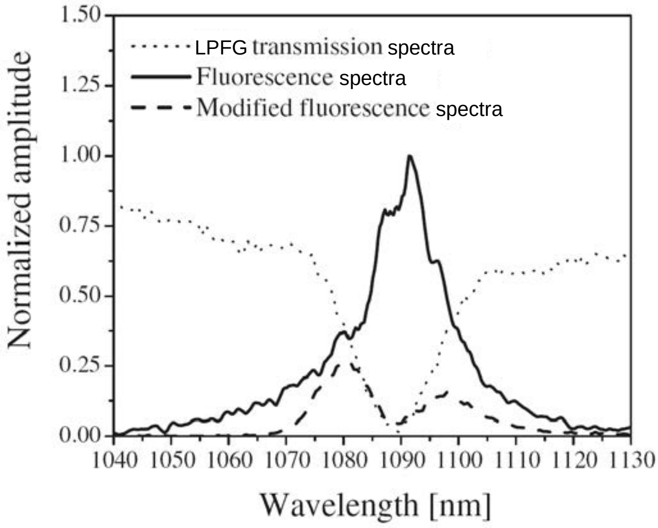

Figure 4.9: Modification in the fluorescence spectrum of the DCYDF laser induced by the LPFG spliced to the laser cavity.

Figure (4.10) shows the output laser spectra at four different wavelengths obtained by tuning the mechanically induced LPHFG, namely at 1079.4, 1084.8, 1087.8, and 1092 *nm*. It is worth mentioning that under certain conditions the laser can operate at multiple wavelengths where the laser is clearly unstable, mainly due to problems of mechanical stability of the device and to nonuniform pressure that results in slight variations in the position of the center wavelength of the notch that causes gain competition between different lasing lines due to homogeneous broadening. We have designed a mechanical fixture that in

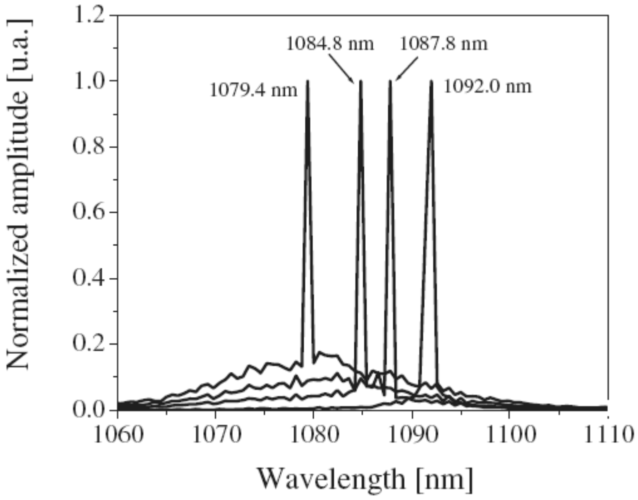

Figure 4.10: Output laser spectra at four different wavelengths tuned by the mechanically induced LPFG.

principle can improve the mechanical stability of our device and can provide a more uniform pressure on the holey fiber.

Figure (4.11) shows the total output laser power as a function of the launched pump power for the four laser wavelengths referred above. Their respective slope efficiencies are, 18.77, 21.52, 23.78, and 26.31%. As we approach to longer wavelengths, the slope efficiency increases, which can be explained by the fact that, without pressure on the microstructured fiber, the laser operates at 1089 *nm*. Further improvements in the laser efficiency can be obtained by inserting a low-loss microstructured fiber, and optimization of the splice loss between the DCYDF and the microstructured fiber through mode matching techniques.

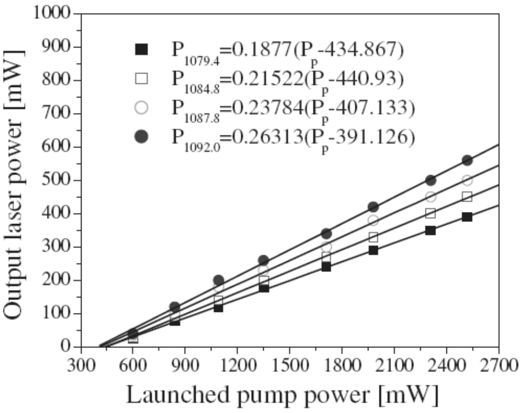

Figure 4.11: Output laser power as a function of the pump power for four different wavelengths.

4.2.4 Conclusions

In conclusion, we have reported a simple method for wavelength tuning of fiber lasers based on the use of a tunable mechanically-induced LPFG in a holey fiber. The center wavelength and depth of the notch are adjusted by changing the period and the applied pressure on the holey fiber. Using this approach, we have demonstrated a wavelength tuning range from 1079.4 to 1092 *nm*. In this wavelength range, slope efficiencies in the range of $18.7 - 26.3\%$ are obtained. The main advantage of this scheme for wavelength tuning of fiber lasers is the simplicity and low cost of the device.

4.3 Simultaneous three-wavelength Yb-doped fiber laser

In this section, a three-wavelength Ytterbium-doped fiber laser based on a long-period fiber grating (LPFG) induced mechanically in a twisted holey fiber is proposed and demonstrated. The scheme used to perform this fiber laser is a modification of the scheme shown previously in Section 4.2 where the LPFG is not under twist. The LPFG is inserted into the laser cavity to introduce inhomogeneous loss in order to obtain up to three output laser wavelengths at room temperature. The lasing wavelengths are localized at 1081.5 nm, 1090.5 nm, and 1100.7 nm with an average wavelength separation of 9.6 nm which can be slightly modified by changing the twist rate of the holey fiber into the laser cavity.

4.3.1 Introduction

Multiwavelength fiber lasers are being subject of continuous interest as an alternative source for applications in wavelength division multiplexed (WDM) optical fiber communications systems, optical instruments, spectroscopy, microwave signal processing, fiber sensors, optical instrument testing, microwave photonic systems and so on. Several approaches have been used to obtain a stable multiwavelength oscillation [116, 117]. The main limitation to obtain multiwavelength laser generation in fiber lasers is the homogeneous gain broadening of the rare-earth dopants which leads strong unstable mode competition and cross-gain saturation. For instance, in Ref. [118] a section of a highly-nonlinear photonic crystal fiber is inserted into the cavity to provide the gain inhomogeneity via four wave mixing between the generated wavelengths, while in Ref. [119] the gain inhomogeneity is induced via stimulated Brillouin scattering in a loop mirror fiber. Other approaches include the utilization of a Fiber Bragg Grating (FBG) as one of the cavity mirrors to increase the number of Brillouin-Stokes lines in a laser cavity [120], cascaded FBGs as a wavelength selection filter [121], wavelength-dependent polarization rotation mechanism with a phase modulator [122], and by controlling the effective length of a polarization maintaining fiber in an intracavity filter [123]. On the other hand, LPFG's have demonstrated their utility in the generation of multiwavelength lasing in rare-earth doped-fiber lasers [124, 125, 126]. LPFGs have been used as band-rejection filters and several applications including gain flattening, variable attenuators, and strain sensors have been explored [18, 127]. In particular, LPFGs induced in holey fibers can lead different behaviors than those observed in conventional fibers, for example, the resonant wavelength can be decreased by increasing the period of the LPFG or they can offer a major power transfer from the core to the cladding modes. LPFGs induced in holey fibers have been reported using corrugated plates, strings and springs. These mechanical methods produce a stress on the optical fiber that induces the periodical index modulation required in order to produce the grating. Recently, it has been demonstrated that the introduction of a certain value of twist in a press-induced long-period holey fiber grating (LPHFG) can be used in order to split any rejection band of the grating in two shifted rejection bands that move symmetrically further apart as the twist is increased [128]. With this method, a band pass filter with controllable bandwidth and low insertion loss is generated. This behavior is unique in LPFGs induced in holey fibers and the twist sensitivity varies according to the holey fiber used in the experiment [92]. Additional characteristics of the LPFG under torsion like the change of the spectral position of the rejection band by the adjustment of the grating period and the control of the depth of the rejection bands by the pressure variation can be exploited in order to obtain a multiwavelength lasing in a Yb-doped fiber laser. Under this concept, a new design that allows generating up to three lasing wavelengths is presented. The design is based on the insertion of a tunable and erasable long-period grating mechanically induced in a section of a twisted holey fiber spliced to a double-clad Yb-doped fiber (DCYDF). The LPFG under torsion acts as an intracavity band-pass filter which spectrum can be modified by changing the twist rate of the holey fiber. The LPFG under torsion modifies the overall gain spectrum of the laser cavity in such way that three controllable peaks on the gain can be obtained. In this way, as the pump is increased, three stable lasing wavelengths are generated. The main advantage of the proposed design is the simplicity and low cost of the device due to that only a single LPFG is used. Also, this scheme offers the possibility to manipulate the separation of the lasing wavelengths controlling the twist rate of the holey fiber.

4.3.2 Experimental setup

Figure (4.12) shows schematically the experimental setup of the three-wavelength fiber laser. It consists of ~ 30 m long DCYDF with a core/cladding diameter of 6/125 μm and a 0.14/0.45 numerical aperture. This fiber is the same used in section 4.1. The DCYDF

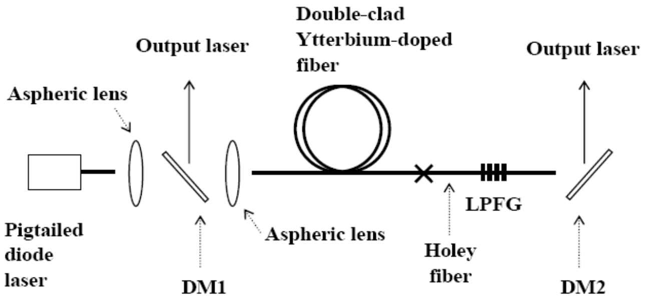

Figure 4.12: Experimental setup of the three-wavelength fiber laser based in a mechanically induced LPHFG.

is end-pumped by a 915 *nm* pigtailed diode laser connected to a fiber collimator via a SMA adapter. The collimated pump is coupled to the cleaved input end of the DCYDF by a focusing aspheric lens. A 45^0 dichroic mirror DM1 between the aspheric lenses and the SMA adapter protects the pump diode laser from back reflection and serves as output coupler for the laser signal. The another end of the DCYDF is spliced to 30 *cm* long of a holey fiber where the mechanical LPHFG is induced. Additionally, another 45^0 dichroic mirror DM2 was placed against the distal end of the holey fiber. The fiber laser cavity is defined by the DCYDF, the spliced holey fiber, and each of the two perpendicular cleaved ends at the sides of the cavity which give 4% of Fresnel reflection allowing a free running operation. The output laser light is detected from the reflected light of both dichroic mirrors. On the other hand, a schematic diagram of the band-pass filter based on a press induced LPHFG under torsion is shown in Figure (4.13) which is similar to setup of Section 3.2 but with another holey fiber. In this setup, the LPHFG was induced by pressing a section of twisted holey fiber (HF) between two corrugated grooved plates (CGPs). The dimensions of both grooved plates were 70 *mm* long and 24 *mm* wide and each one had a square groove pattern with 460 μm of period (Λ). The holey fiber was placed between the CGP by a fixed and rotational holder (H1 and H2). In this way, the fiber can be twisted when the

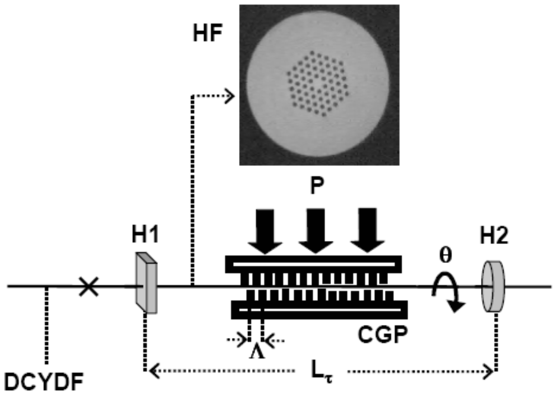

Figure 4.13: Sketch of the device used to mechanically induce the LPHFG in the twisted holey fiber.

rotational holder is turned by an angle (θ). The separation between both holders (L_τ) is 12.5 *cm*. Once the holey fiber is twisted, the holey fiber is pressed between both CGPs and the band-pass filter is generated. The inset in Figure (4.13) shows a photograph of the holey fiber transverse section which correspond to the holey fiber 3 analyzed in Section 2.5.1. This fiber has a core/cladding diameter of 10/125 μm.

4.3.3 Results and discussion

The first step in the implementation of the fiber laser was the characterization of the LPHFG under torsion using only the piece of holey fiber. In this part, the fluorescence of the Yb-doped fiber was used as a light source and an optical spectral analyzer (OSA) was used for the spectrum measurements. A section of the holey fiber was twisted in 12.5 *cm* of length and then, it was pressed between both corrugated grooved plates. This process is repeated for different values of twist: 0, 4 and 5 turns which correspond to values of twist rate (τ) of 0, 0.4 and 0.5 rad/cm respectively. The result is the spectrum transmission illustrated in Figure (4.14) where one can observe that the single rejection band obtained without twist splits in two shifted rejection bands that move symmetrically further apart as the twist is increased. In this way, different band-pass filters with controllable bandwidth are obtained. This result does not depend if the fiber is twisted in clock- or anticlockwise.

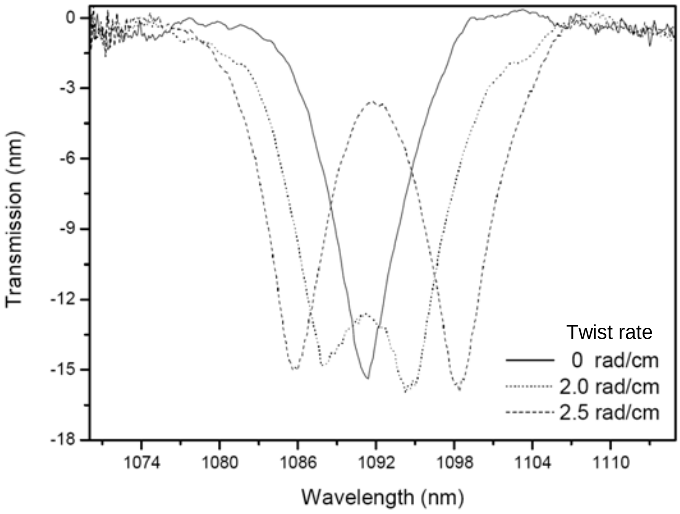

Figure 4.14: Transmission spectra of the LPHFG for different twist rates of the holey fiber.

Once the twist behavior of the LPHFG is controlled, we characterized the fiber laser as a free running fiber laser without the holey fiber spliced to the DCYDF. Under these conditions the laser operated at a wavelength of 1090.5 nm with a threshold pump power of 192 mW and 67% of slope efficiency with respect to the launched pump power. When we spliced the piece of holey fiber to the DCYDF, the threshold pump power increased up to 468 mW, while the slope efficiency decreased to 15%. From these data, the splice loss between the DCYDF and the holey fiber plus the intrinsic holey fiber loss is estimated as $\sim$ 4 dB. The next step was to generate the press-induced LPHFG in the piece of holey fiber spliced to the DCYDF. Once the grating is produced, we modified the gain spectrum of the laser cavity as is it shown in Figures (4.15) and (4.16) where the holey fiber is untwisted and twisted five turns respectively. In Figure (4.15), one can observe that if the single rejection band is tuned adequately, the gain spectrum can be modified in such way that two lasing wavelengths at 1085.2 *nm* and 1098.2 *nm* are obtained. On the other hand, when a certain value of twist is applied to the holey fiber, a band-pass filter is formed as it is shown in Figure (4.16), and three controllable peaks on the gain spectrum can be observed. Consequently, as the pump is increased, three lasing wavelengths are generated. The lasing wavelengths are localized at 1081.5 *nm*, 1090.5 *nm*, and 1100.7 *nm* respectively. In this case, the average wavelength separation between lasing wavelengths is 9.6 *nm* and can be slightly modified ±1.5 *nm* by changing the twist rate of the holey fiber ±0.04 rad/cm. If we exceed this value of twist, the three wavelength laser emission disappears. It is due to the fact that the gain spectrum of the laser cavity is not flat. For example, if the peaks of the gain spectrum shown in Figure (4.16) are separated by increasing the distance between rejection bands in the band-pass filter, these peaks will not have the same gain and only the central peak on the gain spectrum will lead the generation of a wavelength lasing. In this case, only a single wavelength laser emission is obtained. On the other hand, the opposite situation which corresponds to the reduction of the peak separation generates a different result. In this case, the lateral peaks in the gain spectrum will have a higher gain than that in the central peak and only two-wavelength laser emission can be generated.

Figure (4.17) shows the total output laser power as a function of the launched pump power for the laser cavity in the following cases: 1) without LPHFG where only one wavelength lasing at 1090.5 *nm* is obtained, 2) using the LPHFG without twist which corresponds to the dual wavelength lasing shown in Figure (4.15), and 3) using the LPHFG under twist which corresponds to the three-wavelength lasing observed in Figure (4.16). The output laser power for different wavelength lasing were measured together. In Figure (4.17) one can observe that the slope efficiency decreases as the LPHFG is induced on the holey fiber without twist and under twist respectively. These results can be inferred if we consider that when the holey fiber is twisted or under pressure, there is an increase in the loss which reduces the laser efficiency. Additionally, in the case of the LPHFG under twist, we have the presence of two rejection bands on the gain spectrum. These simultaneous bands reduce the level of the gain spectrum to a value lower than that when only one rejection band is used. Then, there is an increment of the loss when a band-pass filter is generated. This characteristic is one of the reasons why the efficiency of the three-wavelength lasing is lower than that of the case of a dual wavelength lasing. It is also important to mention that in a similar way to Section 4.2, further improvements in the laser efficiency can be obtained by inserting a low-loss microstructure fiber into the laser cavity and optimizing the splice loss between the DCYDF and the microstructure fiber through mode matching techniques.

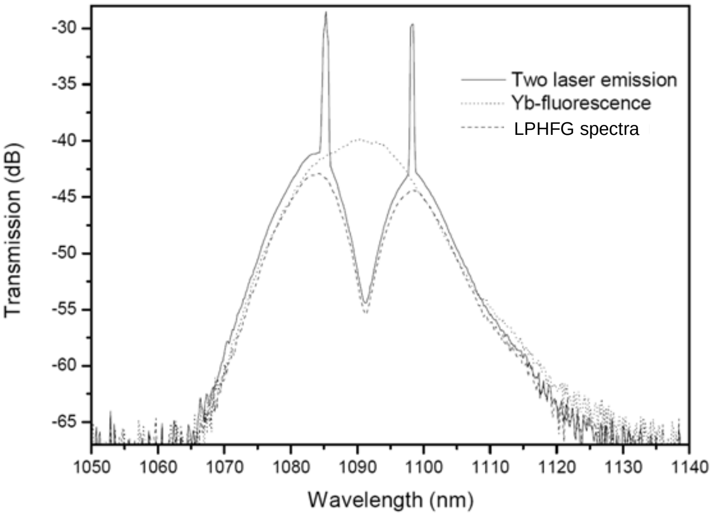

Figure 4.15: Dual-wavelength lasing induced by the LPHFG without twist spliced to the laser cavity.

On the other hand, we observed that the lasing wavelengths are always conditioned to the localization of the peaks formed in the gain spectrum in such way that the laser does not operate at multiple aleatory wavelengths. Nevertheless, the laser emission generated in each one of these peaks is not stable due to the fact there is a gain-competition between the three laser emissions observed in Figure (4.16). Also, the pressure of the mechanical device is non-uniform resulting in slight variations in the LPFG spectra. In similar way to section 4.2, further improvements of the mechanical device have to be performed in order to provide a more uniform pressure on the holey fiber, and in this way to obtain a laser stability.

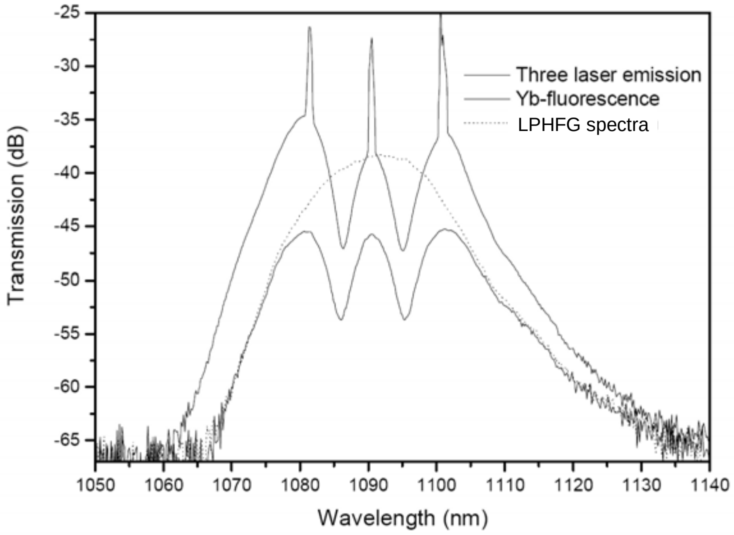

Figure 4.16: Three-wavelength lasing induced by the LPHFG with twist spliced to the laser cavity.

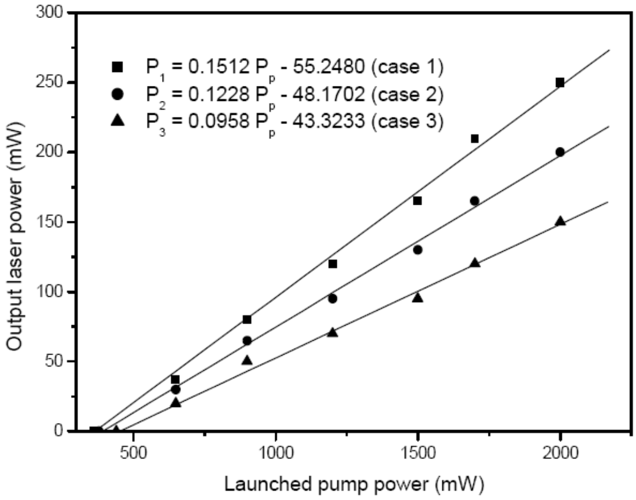

Figure 4.17: Output laser power (P_1, P_2, P_3) as a function of the pump power (P_P) for three different cavity cases: 1) without LPHFG, 2) using LPHFG without twist, and 3) using LPHFG with twist.

4.3.4 Conclusions

We have reported a new method in order to obtain a simultaneous three-wavelength Yb-doped fiber laser based on a single long period fiber grating induced mechanically in a twisted holey fiber. The lasing wavelengths were obtained at 1081.5 nm, 1090.5 nm, and 1100.7 nm with an average wavelength separation of 9.6 nm. Additionally, with this design, one can choose between a dual- or three-wavelength laser operation depending on if the holey fiber is twisted or not into the laser cavity. The main advantage of the proposed design is the simplicity and low cost of the device due to that only a single LPFG is used. Additionally, this scheme offers the possibility to manipulate slightly the separation of the lasing wavelengths controlling the twist rate of the holey fiber.

5 Conclusions

In this thesis, a characterization of three different schemes based in a mechanically-induced long-period fiber grating (LPFG) inscribed in a photonic criystal fiber was presented. These schemes allow the obtention of novel LPFG properties not reported, to our knowledge in the literature. These properties can be summarized as follows,

- The tuning range of mechanically induced LPFGs in PCFs has been improved. This improvement was obtained by considering a mechanical setup with radial grooved plates. In this way, varying the bend of the holey fiber, the grating period can be modified in a more extended range compared with other mechanical methods. An interesting characteristic observed in this setup was the fact that the bend radius does not modify the typical behavior of the attenuation bands in LPFGs. As an example, the modification of the bandwidth with respect to the number, N, of grooved plates follows the typical behavior, $1/N$, and the tuning measurements of the LPFG show the typical redshift of the resonance wavelength as the grating period is increased.
- The couplings of the fundamental LP_{01} core mode and the even and odd LP_{11} higher-order core modes have been reported and analyzed, to our knowledge for first time in mechanically-induced LPFGs in PCFs. These couplings occur due to the fact that the asymmetry in the cladding structure of the holey fiber allows the propagation of the even- and odd-LP_{11} higher-order core modes. Additionally, the attenuation bands of these couplings depend strongly on the fiber orientation with respect to the pressure direction of the mechanical setup. This dependency is very useful in the design of

all-fiber devices based on LPFGs that involves couplings of even and odd LP_{11} core modes.

- The analysis of the twist effect in mechanically induced LPFGs in PCFs was reported to our knowledge for first time. The results show that the rejection bands for each holey fiber split in two shifted rejection bands that move symmetrically further apart as the twist is increased. The LPFG shows higher twist sensitivity if the holey fiber presents a higher imperfect cladding structure. Also, the splitting of the rejection bands shows a linear behavior within an extended twist range which is ideal for the design of torsion fiber sensors. Additionally, the twist sensitivities reported in this work show higher values than those reported in literature where other types of LPFGs in standard optical fibers are used.

With these properties, three direct applications have been performed. These applications consist in new schemes to obtain tunable Ytterbium-doped fiber lasers, new band-pass filters, and simultaneously generation of three-wavelength Yb-doped fiber lasers respectively. The principal results of these applications can be summarized as follows:

- A new scheme to tune a Ytterbium-doped fiber laser based in a mechanically induced LPFG in a PCF is suggested and demonstrated. The main advantage of this scheme is the simplicity and low cost of the device. With this method, a tuning range from 1079.4 to 1092 nm, with slope efficiencies of 18.7-26.3% with respect to the launched pump power is obtained.
- A new efficient method to perform a band-pass filter based in a mechanically induced LPFG is reported. The band-pass filter is generated due to the splitting of the attenuation bands of a LPFG induced in a PCF under twist. According to the twist applied to the fiber and the interaction length of the grooved plates, one can control the bandwidth of the band-pass filter. With this scheme, one can obtain a higher flexibility in the band-pass filter parameters than that shown in band-pass filters generated with other methods.

- A new method to obtain a simultaneous three-wavelength Ytterbium-doped fiber laser based on a LPFG induced mechanically in a PCF is reported. A long-period grating induced mechanically in a PCF under twist is inserted into the laser cavity to introduce inhomogeneous loss in order to obtain up to three output laser wavelengths at room temperature. The lasing wavelengths are localized at 1081.5 *nm*, 1090.5 *nm*, and 1100.7 *nm* with an average wavelength separation of 9.6 *nm*. With this design, one can choose between a dual- or three-wavelength laser operation depending if either the PCF is twisted or not into the laser cavity. The main advantage of the proposed design is the simplicity and low cost of the device since only a single LPFG is used. Additionally, this scheme offers the possibility to manipulate slightly the separation of the lasing wavelengths controlling the twist rate of the holey fiber.

Additionally, according to the numerical method performed in this thesis, the following results can be summarized,

- A FFT-mode solver method to modelate PCFs is generated. With this method, one can modelate different transversal structures of the microstructured cladding with periodic or aperiodic distribution of holes using circular or elliptic air holes respectively. The precision of this method in the calculations of the effective index value is around 1×10^{-6}, although further improvements can be realized in order to obtain precision values around 1×10^{-7}.

- The FFT-mode solver implemented in this work, can modelate photonic crystal fibers with no perfect arrangement of holes in their cladding structure. These characteristics are typical in the majority of microstructured fibers.

- Besides, the FFT-mode solver can be used to design PCFs with specific properties. As an example, PCFs with flat dispersion or shifted zero dispersion for supercontinuum applications can be studied.

- Finally, the FFT-mode solver performed in this work can modelate the mode solutions of PCFs in the linear and the nonlinear regime. In the nonlinear regime, a Kerr-nonlinearity is considered and also a self-consistent method is added to the algorithm. Nevertheless, to solve completely the nonlinear modes in PCFs, a propagation algorithm based on perturbative methods have to be performed in order to study the stability of these solutions.

5.1 Future work

Additional properties of LPFG in PCFs have to be analyzed in future work; for example, a systematic study of polarization in LPFGs induced mechanically in twisted PCFs. In this case, the linear birefringence of the fiber caused by the mechanical setup and the circular birefringence induced by twist have to be considered. In a similar way, the same systematic study for LPFGs induced in PCFs under bending have to be analyzed. Also, the characterization of LPFGs realized in this work can be extended to LPFGs induced in PCFs with other fabrication methods. For example, with electric-arc discharges.

In general, the tools and skills developed in this work have given a platform to design new all-fiber devices based on photonic crystal fibers. This platform also allows the beginning of other research lines in the future, for example, the modelling of PCFs for supercontinuum applications, the performance of three-wavelength Raman fiber lasers, and the modelling of advanced systems such as the propagation of solitons in PCFs and its interactions with plasmons respectively.

A FFT-mode solver algorithm

In order to modelate the photonic crystal fibers shown in Figure (2.9), first we have to modify their images in order to obtain a binary version of them. As example, in Figure (A.1) the modified binary image of holey fiber 2 is shown respectively.

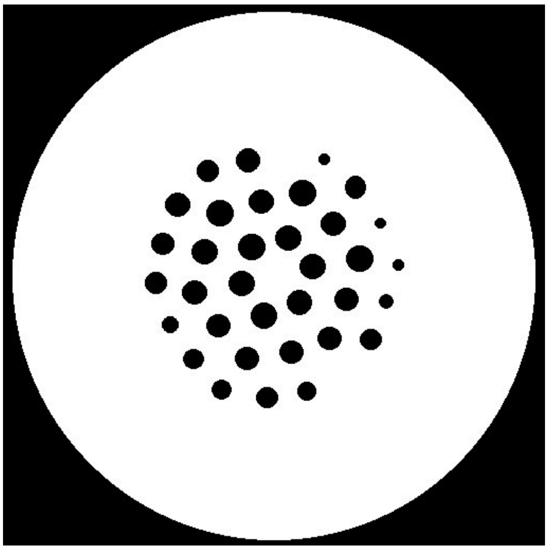

Figure A.1: Binary image of the transversal refractive index profile of the microstructured holey fiber 2 of Figure (2.9)b.

Once the PCF image is modified, this is introduced to the FFT-mode solver algorithm coded in Matlab. This algorithm is given in Figures (A.2)-(A.6).

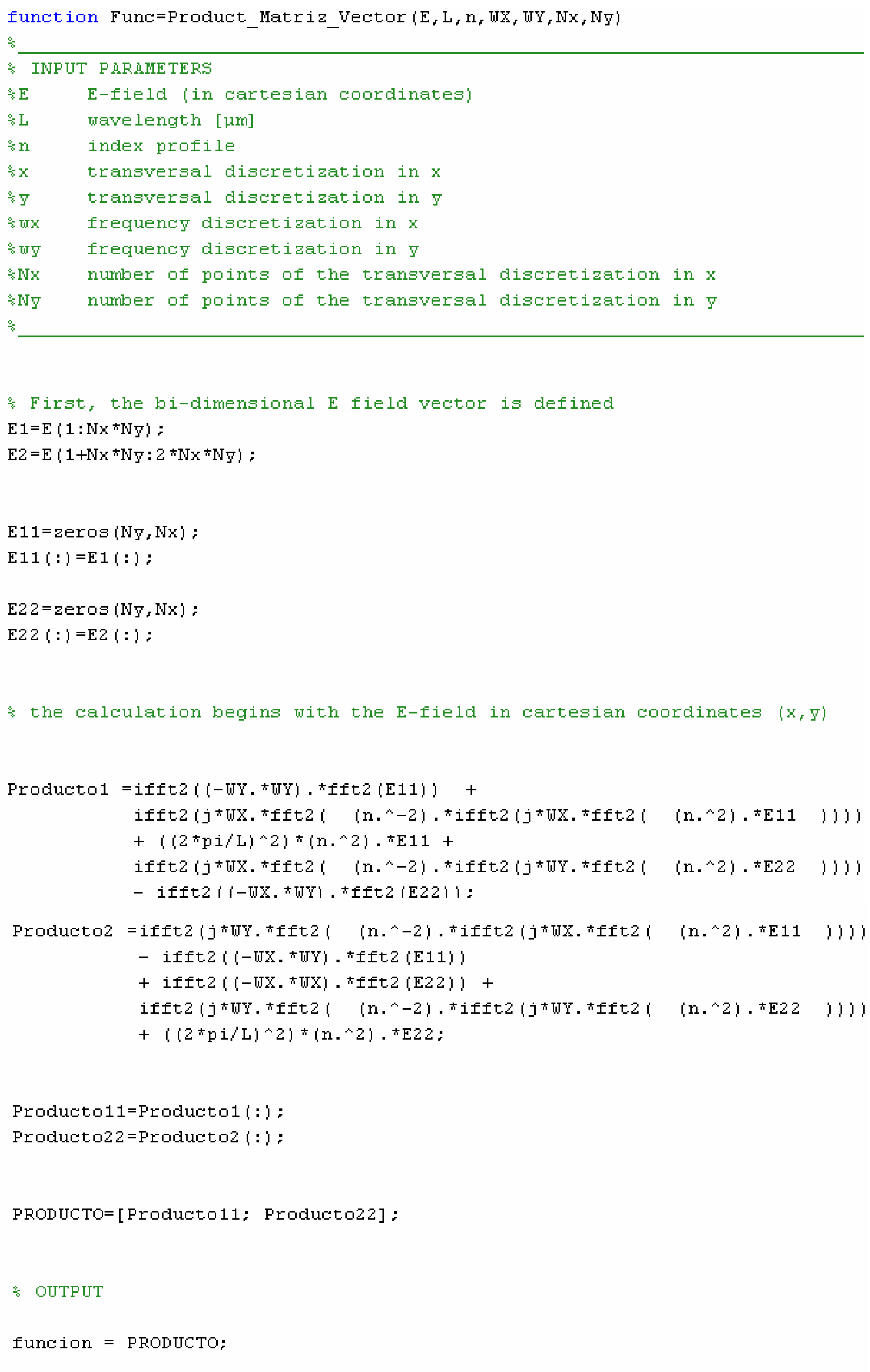

```
function Func=Product_Matriz_Vector(E,L,n,WX,WY,Nx,Ny)
%__________________________________________________________________________
% INPUT PARAMETERS
%E     E-field (in cartesian coordinates)
%L     wavelength [µm]
%n     index profile
%x     transversal discretization in x
%y     transversal discretization in y
%wx    frequency discretization in x
%wy    frequency discretization in y
%Nx    number of points of the transversal discretization in x
%Ny    number of points of the transversal discretization in y
%__________________________________________________________________________


% First, the bi-dimensional E field vector is defined
E1=E(1:Nx*Ny);
E2=E(1+Nx*Ny:2*Nx*Ny);


E11=zeros(Ny,Nx);
E11(:)=E1(:);

E22=zeros(Ny,Nx);
E22(:)=E2(:);


% the calculation begins with the E-field in cartesian coordinates (x,y)


Producto1 =ifft2((-WY.*WY).*fft2(E11))  +
           ifft2(j*WX.*fft2(  (n.^-2).*ifft2(j*WX.*fft2(  (n.^2).*E11  ))))
           + ((2*pi/L)^2)*(n.^2).*E11 +
           ifft2(j*WX.*fft2(  (n.^-2).*ifft2(j*WY.*fft2(  (n.^2).*E22  ))))
           - ifft2((-WX.*WY).*fft2(E22));

 Producto2 =ifft2(j*WY.*fft2(  (n.^-2).*ifft2(j*WX.*fft2(  (n.^2).*E11  ))))
            - ifft2((-WX.*WY).*fft2(E11))
            + ifft2((-WX.*WX).*fft2(E22)) +
            ifft2(j*WY.*fft2(  (n.^-2).*ifft2(j*WY.*fft2(  (n.^2).*E22  ))))
            + ((2*pi/L)^2)*(n.^2).*E22;


 Producto11=Producto1(:);
 Producto22=Producto2(:);


 PRODUCTO=[Producto11; Producto22];


 % OUTPUT

 funcion = PRODUCTO;
```

Figure A.2: Part 1. FFT-mode solver algorithm. This part corresponds to the product of the left side of equation (2.6) respectively.

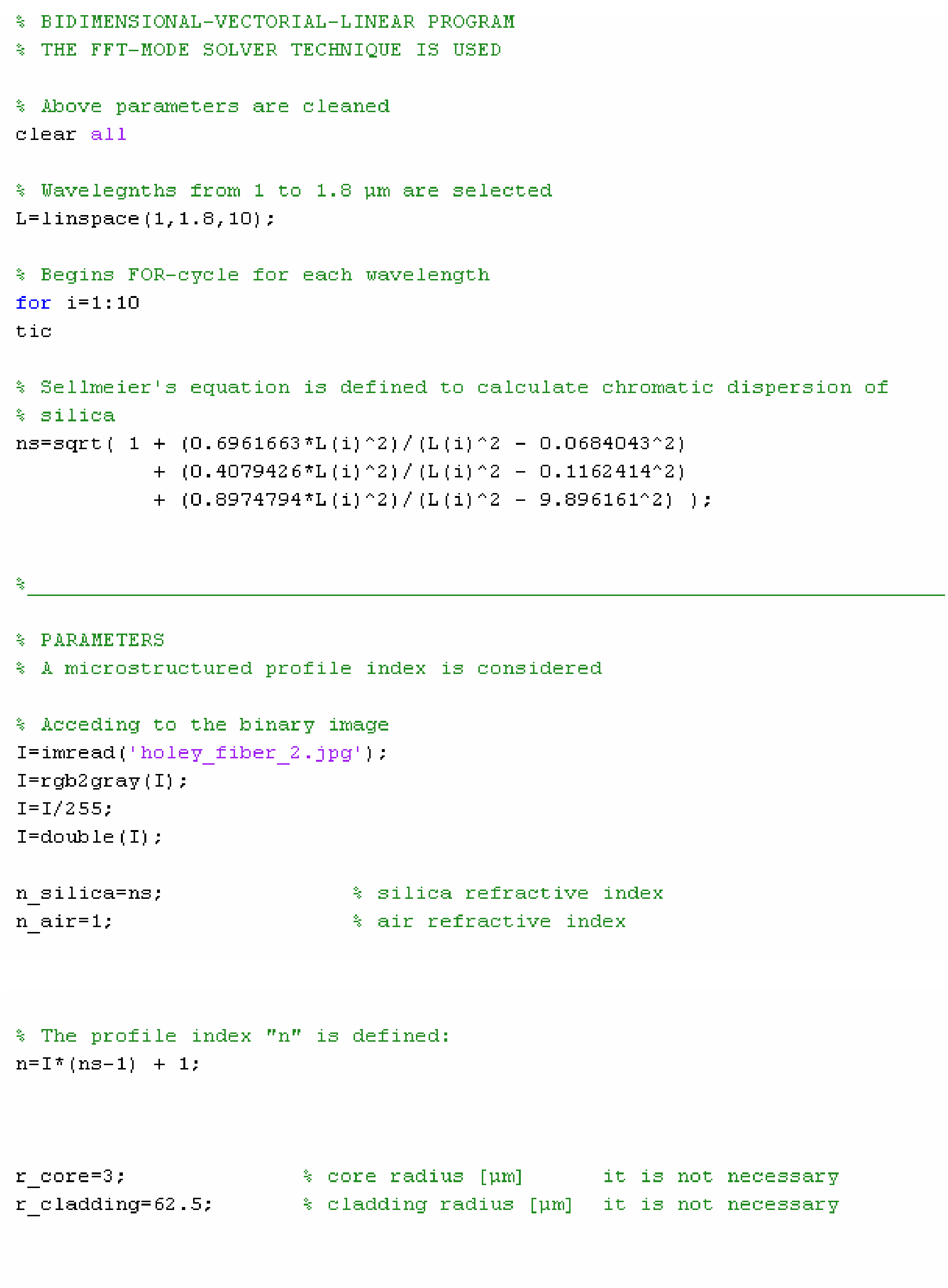

```
% BIDIMENSIONAL-VECTORIAL-LINEAR PROGRAM
% THE FFT-MODE SOLVER TECHNIQUE IS USED

% Above parameters are cleaned
clear all

% Wavelegnths from 1 to 1.8 µm are selected
L=linspace(1,1.8,10);

% Begins FOR-cycle for each wavelength
for i=1:10
tic

% Sellmeier's equation is defined to calculate chromatic dispersion of
% silica
ns=sqrt( 1 + (0.6961663*L(i)^2)/(L(i)^2 - 0.0684043^2)
           + (0.4079426*L(i)^2)/(L(i)^2 - 0.1162414^2)
           + (0.8974794*L(i)^2)/(L(i)^2 - 9.896161^2) );


%

% PARAMETERS
% A microstructured profile index is considered

% Acceding to the binary image
I=imread('holey_fiber_2.jpg');
I=rgb2gray(I);
I=I/255;
I=double(I);

n_silica=ns;                % silica refractive index
n_air=1;                    % air refractive index



% The profile index "n" is defined:
n=I*(ns-1) + 1;



r_core=3;               % core radius [µm]      it is not necessary
r_cladding=62.5;        % cladding radius [µm]  it is not necessary
```

Figure A.3: Part 2. FFT-mode solver algorithm. This part corresponds to the solution of eigenvalues and eigenvectors of the holey fiber 2.

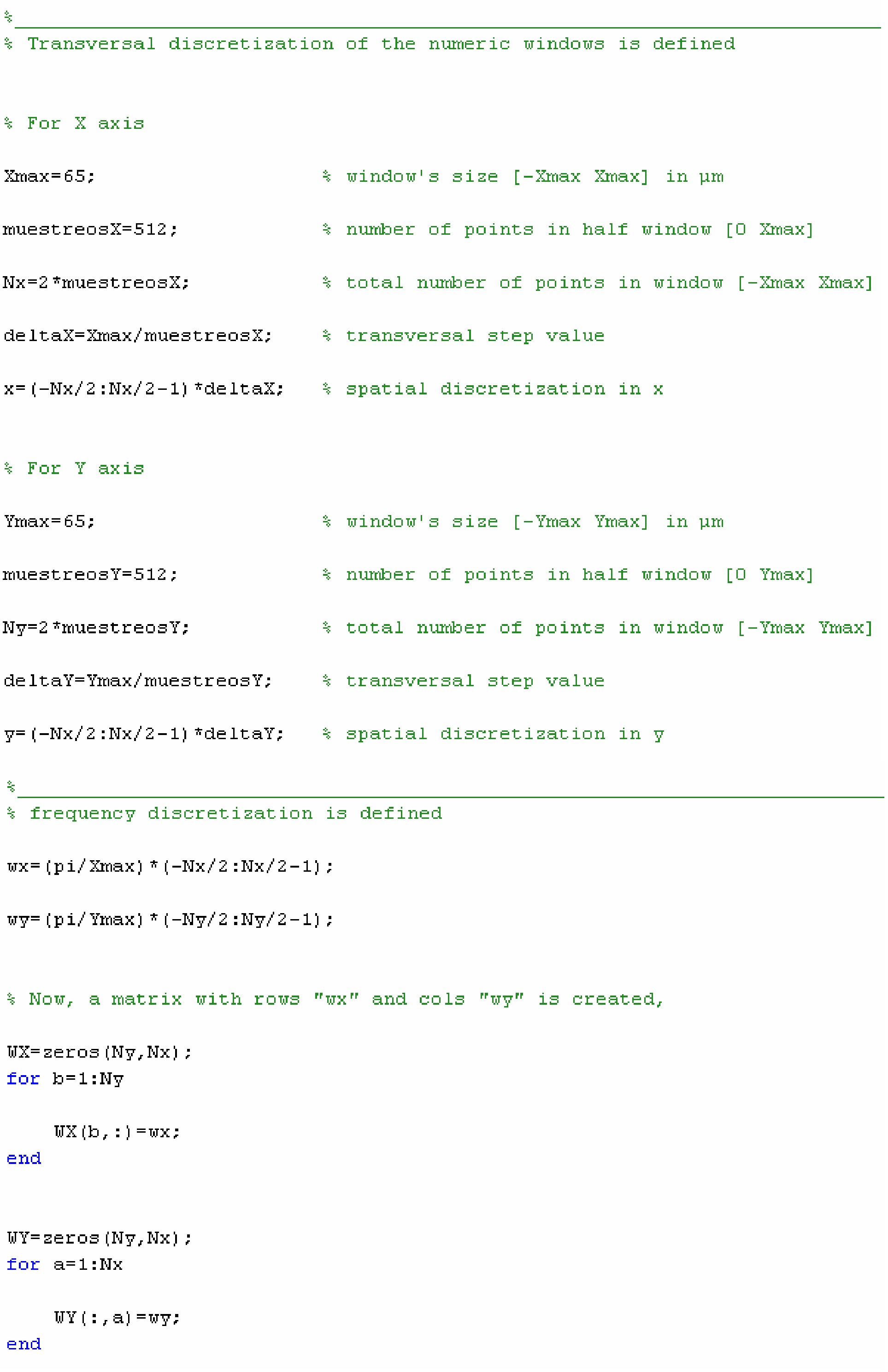

```
%________________________________________________________________________
% Transversal discretization of the numeric windows is defined


% For X axis

Xmax=65;                    % window's size [-Xmax Xmax] in µm

muestreosX=512;             % number of points in half window [0 Xmax]

Nx=2*muestreosX;            % total number of points in window [-Xmax Xmax]

deltaX=Xmax/muestreosX;     % transversal step value

x=(-Nx/2:Nx/2-1)*deltaX;    % spatial discretization in x


% For Y axis

Ymax=65;                    % window's size [-Ymax Ymax] in µm

muestreosY=512;             % number of points in half window [0 Ymax]

Ny=2*muestreosY;            % total number of points in window [-Ymax Ymax]

deltaY=Ymax/muestreosY;     % transversal step value

y=(-Nx/2:Nx/2-1)*deltaY;    % spatial discretization in y

%________________________________________________________________________
% frequency discretization is defined

wx=(pi/Xmax)*(-Nx/2:Nx/2-1);

wy=(pi/Ymax)*(-Ny/2:Ny/2-1);


% Now, a matrix with rows "wx" and cols "wy" is created,

WX=zeros(Ny,Nx);
for b=1:Ny

    WX(b,:)=wx;
end


WY=zeros(Ny,Nx);
for a=1:Nx

    WY(:,a)=wy;
end
```

Figure A.4: Part 3. FFT-mode solver algorithm. Continuation of the solution of eigenvalues and eigenvectors of the holey fiber 2.

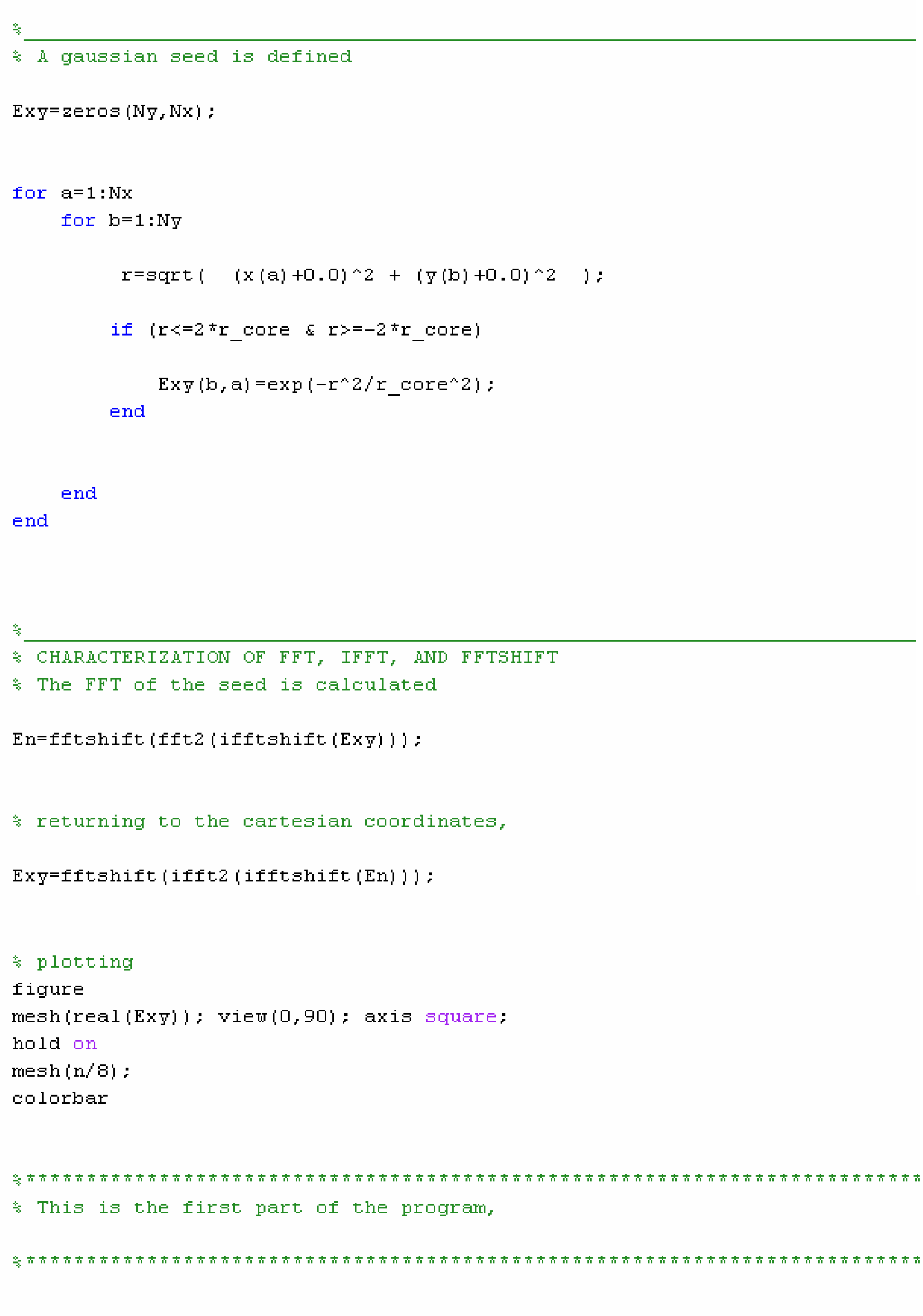

```
%___________________________________________________________________________
% A gaussian seed is defined

Exy=zeros(Ny,Nx);


for a=1:Nx
    for b=1:Ny

         r=sqrt(  (x(a)+0.0)^2 + (y(b)+0.0)^2  );

        if (r<=2*r_core & r>=-2*r_core)

            Exy(b,a)=exp(-r^2/r_core^2);
        end


    end
end



%___________________________________________________________________________
% CHARACTERIZATION OF FFT, IFFT, AND FFTSHIFT
% The FFT of the seed is calculated

En=fftshift(fft2(ifftshift(Exy)));


% returning to the cartesian coordinates,

Exy=fftshift(ifft2(ifftshift(En)));


% plotting
figure
mesh(real(Exy)); view(0,90); axis square;
hold on
mesh(n/8);
colorbar


%***************************************************************************
% This is the first part of the program,

%***************************************************************************
```

Figure A.5: Part 4. FFT-mode solver algorithm. Continuation of the solution of eigenvalues and eigenvectors of the holey fiber 2.

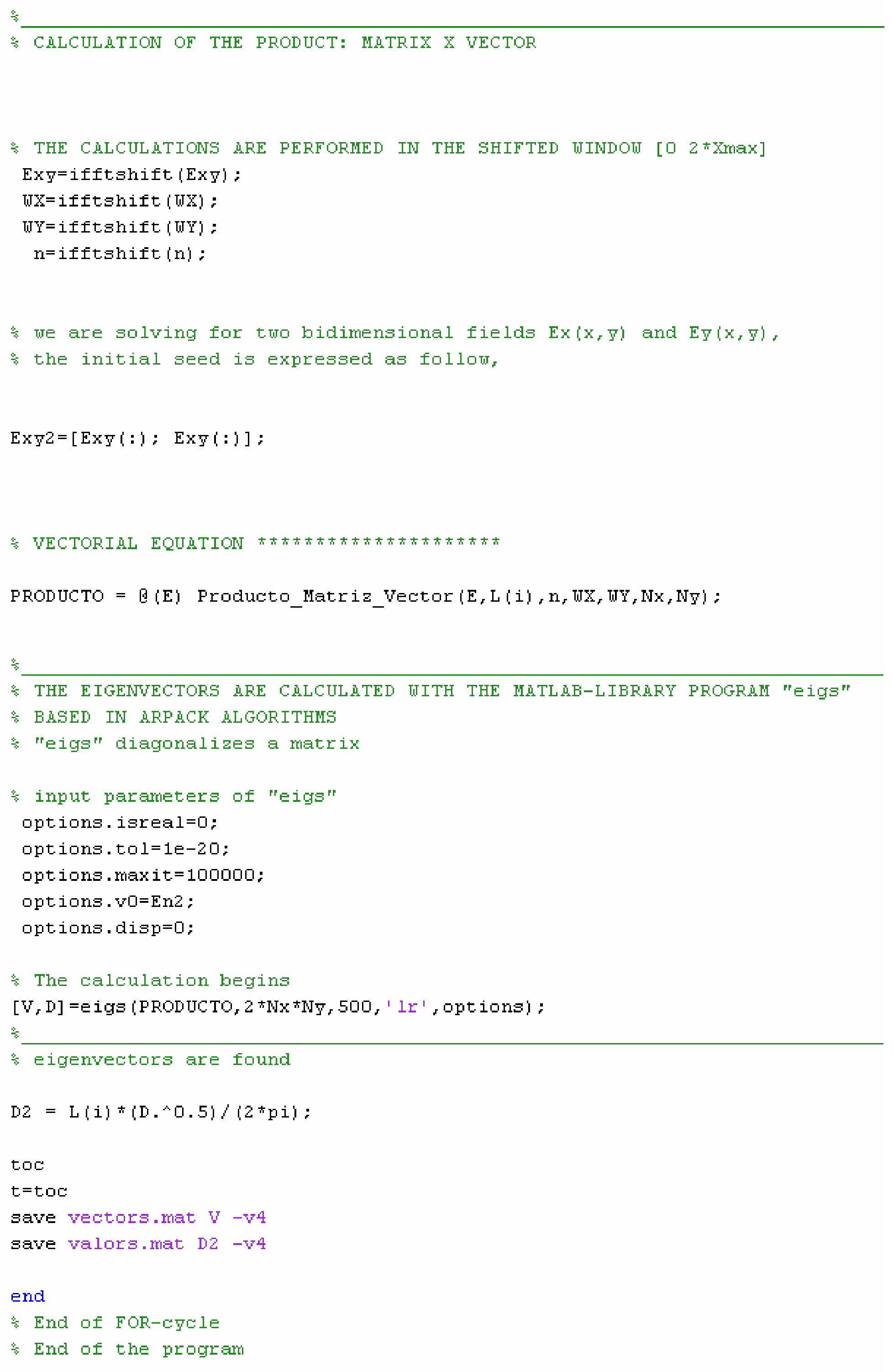

```
%________________________________________________________________________
% CALCULATION OF THE PRODUCT: MATRIX X VECTOR



% THE CALCULATIONS ARE PERFORMED IN THE SHIFTED WINDOW [0 2*Xmax]
 Exy=ifftshift(Exy);
 WX=ifftshift(WX);
 WY=ifftshift(WY);
  n=ifftshift(n);


% we are solving for two bidimensional fields Ex(x,y) and Ey(x,y),
% the initial seed is expressed as follow,


Exy2=[Exy(:); Exy(:)];



% VECTORIAL EQUATION *********************

PRODUCTO = @(E) Producto_Matriz_Vector(E,L(i),n,WX,WY,Nx,Ny);


%________________________________________________________________________
% THE EIGENVECTORS ARE CALCULATED WITH THE MATLAB-LIBRARY PROGRAM "eigs"
% BASED IN ARPACK ALGORITHMS
% "eigs" diagonalizes a matrix

% input parameters of "eigs"
 options.isreal=0;
 options.tol=1e-20;
 options.maxit=100000;
 options.v0=En2;
 options.disp=0;

% The calculation begins
[V,D]=eigs(PRODUCTO,2*Nx*Ny,500,'lr',options);
%________________________________________________________________________
% eigenvectors are found

D2 = L(i)*(D.^0.5)/(2*pi);

toc
t=toc
save vectors.mat V -v4
save valors.mat D2 -v4

end
% End of FOR-cycle
% End of the program
```

Figure A.6: Part 5. FFT-mode solver algorithm. Continuation of the solution of eigenvalues and eigenvectors of the holey fiber 2.

References

[1] S. James and R. Tatam, *Optical fibre long-period grating sensors: characteristics and application*, Meas. Sci. Technol. **14**, 49 (2003).

[2] J. C. Knight, T. A. Birks, P. S. J. Russell, and D. M. Atkin, *All-silica single-mode optical fiber with photonic crystal cladding*, Opt. Lett. **21**, 1547 (1996).

[3] P. Russell, *Photonic crystal fibers*, Science **299**, 358 (2003).

[4] A. Ortigosa-Blanch, J. C. Knight, W. J. Wadsworth, J. Arriaga, B. J. Mangan, T. A. Birks, and P. S. J. Russell, *Highly birefringent photonic crystal fibers*, Opt. Lett. **25**, 1325 (2000).

[5] A. Ferrando, E. Silvestre, P. Andres, J. J. Miret, and M. V. Andres, *Designing the properties of dispersion-flattened photonic crystal fibers*, Opt. Express **9**, 687 (2001).

[6] G. Kakarantzas, G. Birks, and P. Russell, *Structural long-period gratings in photonic crystal fibers*, Opt. Lett. **27**, 1013 (2002).

[7] T. Erdogan, *Cladding-mode resonances in short- and long-period fiber grating filters*, J. Opt. Soc. Am. A **14**, 1760 (1997).

[8] A. Othonos and K. Kyriacos, *Fiber Bragg Gratings, Fundamental and applications in Telecommunications and sensing* (Artech House Inc., 1991), 1st ed.

[9] R. Kashyap, *Fiber Bragg Gratings* (Optics and Photonics, 1999), 1st ed.

[10] A. Ghatak and K. Thyagarajan, *Introduction to fiber optics* (Cambridge University press, 1998), 1st ed.

[11] F. Poli, A. Cucinotta, and S. Selleri, *Photonic crystal fibers, properties and applications* (Springer, 2007), 1st ed.

[12] A. W. Snyder and J. D. Love, *Optical waveguide theory* (Chapman and Hall, 1983), 2nd ed.

[13] R. K. Wangsness, *Campos electromagnéticos* (Limusa, 1998), 12th ed.

[14] D. Kumar and P. K. Choudhury, *Introduction to modes and their designation in circular and elliptical fibers*, Am. J. Phys. **75**, 546 (2007).

[15] I. Gómez-Castellanos and R. M. Rodríguez-Dagnino, *Intensity distributions and cutoff frequencies of linearly polarized modes for a step-index elliptical optical fiber*, Opt. Eng. **46**, 1 (2007).

[16] C. Tsao, *Optical fibre waveguide analysis* (Oxford University Press, 1991), 10th ed.

[17] V. Bhatia, *Applications of long-period gratings to single and multi-parameter sensing*, Opt. Express **4**, 457 (1999).

[18] A. Vengsarkar, P. Lemaire, J. Justin, V. Bhatia, T. Erdogan, and J. Sipe, *Long-period fiber gratings as band-rejection filters*, J. Lightwave Technol. **14**, 58 (1996).

[19] Y. J. He, Y. L. LO, and J. F. Huang, *Bandwidth analysis of long-period fiber grating for high-order cladding mode and its application to an optical add-drop multiplexer*, Opt. Eng. **45**, 1 (2006).

[20] G. Meltz, W. Morey, and W. Glenn, *Formation of bragg gratings in optical fibers with a trasnverse holographic method*, Opt. Lett. **14**(15), 823 (1989).

[21] K. Hill, B. Malo, V. Vineberg, F. Bilodeau, D. Johnson, and J. Albert, *Bragg gratings fabricated in monomode photosensitive optica fiber by UV exposure through a phase mask*, Appl. Phys. Lett. **62**, 1035 (1993).

[22] K. Hill, B. Malo, V. Vineberg, F. Bilodeau, D. Johnson, and I. Skinner, *Efficient mode conversion in telecommunication fibre using externally written gratings*, Electron. Lett. **26**, 1270 (1990).

[23] K. Hill, Y. Fuji, D. Johnson, and B. Kawasaki, *Photosensitivity in optical fiber waveguides: Application to reflection filter fabrication*, Appl. Phys. Lett. **32**, 647 (1978).

[24] W. Yi-Ping, C. Jian-Ping, and R. Yun-Jiang, *Torsion characteristics of long-period fiber gratings induced by high-frequency CO_2 laser pulses*, J. Opt. Soc. Am. B **22**, 1167 (2005).

[25] D. Davis, T. Gaylord, E. Kosinski, S. Mettler, and A. Vengsarkar, *Long-period fibre grating fabrication with focused CO_2 laser pulses*, Electron. Lett. **34**, 302 (1998).

[26] S. Yamasaki, M. Akiyama, K. Wada, and R. Yamauchi, *Characteristics on long-period grating utilizing periodic stress relaxation*, IEICE Transactions on Electronics **E83**, 440 (2000).

[27] L. Drozin, P. Fonjallaz, and L. Stensland, *Long-period fibre gratings written by CO_2 exposure of H_2-loaded standard fibres*, Electron. Lett. **36**(8), 742 (2000).

[28] P. Palai, M. Das, K. Thyagarajan, and B. Pal, *Characterization and simulation of long-period gratings fabricated using electric discharge*, Opt. Commun. **193**, 181 (2001).

[29] G. Humbert and A. Malki, *Electric-arc-induced gratings in non-hydrogenated fibres: fabrication and high-temperature characterizations*, J. Opt. A: Pure Appl. Opt. **4**, 194 (2002).

[30] G. Rego, E. Dianov, and V. Sulimov, *High-temperature stability of long-period fiber gratings produced using an electric arc*, J. Lightwave Technol. **19**, 1547 (2001).

[31] A. Yariv and P. Yeh, *Optical waves in crystals* (John Wiley and Sons, Inc., 1984), 1st ed.

[32] S. Savin, M. J. F. Digonnet, G. S. Kino, and H. J. Shaw, *Tunable mechanically induced long-period fiber gratings*, Opt. Lett **25**, 710 (2000).

[33] G. Rego, J. R. A. Fernandez, J. L. Santos, H. M. Salgado, and P. V. S. Marques, *New technique to mechanically induce long-period fiber gratings*, Opt. Commun. **220**, 111 (2003).

[34] T. Yokouchi, Y. Suzaki, K. Nakagawa, M. Yamauchi, M. Kimura, Y. Mizutani, S. Kimura, and S. Ejima, *Thermal tuning of mechanically induced long-period fiber grating*, Appl. Opt. **44**, 5024 (2005).

[35] A. A. Abramov, A. Hale, R. S. Windeler, and T. A. Strasser, *Widely tunable long-period fibre gratings*, Electron. Lett. **35**, 81 (1999).

[36] G. D. V. Wiggeren, T. K. Gaylord, D. Davis, M. I. Braiwish, E. N. Glytsis, and E. Anemogiannis, *Tuning, attenuating, and switching by controlled long-period fiber gratings*, Opt. Lett. **26**, 61 (2001).

[37] B. J. Eggleton, C. Kerbage, P. S. Westbrook, R. S. Winderler, and A. Hale, *Microstructured optical fiber devices*, Opt. Express **9**, 698713 (2001).

[38] I. B. Sohn, N.-K. Lee, H.-W. Kwon, and J.-W. Song, *Tunable gain-flattening filter using microbending long period fiber gratings*, Opt. Eng. **41**, 14651466 (2002).

[39] Y. G. Han, C.-S. Kim, J. U. Kang, U. Peak, and Y. Chung, *Multi-wavelength raman fiber-ring laser based on tunable cascaded long-period fiber gratings*, IEEE Photon. Technol. Lett. **15**, 383385 (2003).

[40] J. H. Iim, H. S. Jang, K. S. Lee, J. C. Kim, and B. H. Lee, *Mach-Zehnder interferometer formed in a photonic crystal fiber based on a pair of long-period fiber gratings*, Opt. Lett. **29**, 346348 (2004).

[41] D. Lee, Y. Jung, Y. S. Jeong, K. Oh, J. Kobelke, K. Schuster, and J. Kirchhof, *Highly polarization-dependence periodic coupling mechanically induced long period grating over air-silica fiber*, Opt. Lett. **31**, 296298 (2006).

[42] P. Steinvurzel, E. D. Moore, E. C. Magi, and B. J. Eggleton, *Tuning properties of long period gratings in photonic bandgap fibers*, Opt. Lett. **31**, 21032105 (2006).

[43] P. Kaiser, E. A. J. Marcatili, and S. E. Miller, *A new optical fiber*, Bell Syst. Tech. J **52**, 265 (1973).

[44] L. Tartara, I. Cristiani, V. Degiorgio, F. Carbone, D. Faccio, and M. Romagnoli, *Nonlinear propagation of ultrashort laser pulses in a microstructured fiber*, J. Nonlinear Opt. Phys. Mater. **11**, 409 (2002).

[45] N. G. R. Broderick, T. M. Monro, P. J. Bennett, and D. J. Richardson, *Nonlinearity in holey optical fibers: measurement and future opportunities*, Opt. Lett. **24**, 1395 (1999).

[46] N. A. Mortensen and J. R. Folkenberg, *Low-loss criterion and effective area considerations for photonic crystal fibres*, J. Opt. A: Pure Appl. Opt. **5**, 163 (2003).

[47] J. C. Knight, T. A. Birks, R. F. Cregan, P. S. J. Russell, and J.-P. de Sandro, *Large mode area photonic crystal fiber*, Electron. Lett. **34**, 1347 (1998).

[48] N. A. Mortensen, J. R. Folkenberg, P. M. W. Skovgaard, and J. Broeng, *Numerical aperture of single mode photonic crystal fibers*, IEEE Photonics Technol. Lett. **14**, 1094 (2002).

[49] M. Midrio, M. Singh, and C. Someda, *The space filling mode of holey fibers: an analytical vectorial solution*, J. Lightwave. Technol. **18**, 1031 (2000).

[50] T. Ritari, J. Tuominen, J. C. Petersen, T. Srensen, T. P. Hansen, H. Simonsen, and H. Ludvigsen, *Gas sensing using air-guiding photonic bandgap fibers*, Opt. Express **12**, 4080 (2004).

[51] T. M. Monro and D. J. Richardson, *Holey optical fibres: Fundamental properties and device applications*, C. R. Phys. **4**, 175 (2003).

[52] J. C. Knight, J. Arriaga, T. A. Birks, A. Ortigosa-Blanch, W. J. Wadsworth, and P. S. Russell, *Anomalous dispersion in photonic crystal fiber*, IEEE Photonics Technol. Lett. **12**, 807 (2000).

[53] J. C. Baggett, T. M. Monro, K. Furusawa, and D. J. Richardson, *Comparative study of large-mode holey and conventional fibers*, Opt. Lett. **26**, 1045 (2001).

[54] T. P. Hansen, J. Broeng, S. E. B. Libori, E. Knudsen, A. Bjarklev, J. R. Jensen, and H. Simonsen, *Highly birefringent index-guiding photonic crystal fibers*, IEEE Photonics Technol. Lett. **13**, 588 (2001).

[55] K. Saitoh and M. Koshiba, *Single-polarization single-mode photonic crystal fibers*, IEEE Photonics Technol. Lett. **15**, 1384 (2003).

[56] A. B. Fedotov, S. O. Konorov, Y. N. Kondrat'ev, S. N. Bagayev, V. S. Shevandin, K. V. Dukel'skii, D. A. Sidorov-Biryukov, A. V. Khokhlov, V. B. Smirnov, and A. M. Zheltikov, *Measurement of optical losses for a family of microstructure fibers with a sequentially increasing number of hexagonal cycles of air holes*, Laser Phys. **13**, 856 (2003).

[57] T. P. White, R. C. McPhedran, C. M. de Sterke, L. C. Botten, and M. J. Steel, *Confinement losses in microstructured optical fibers*, Opt. Lett. **26**, 1660 (2001).

[58] R. Wolinski, A. Czapla, S. Ertman, M. Tefelska, A. Domanski, E. Nowinowski-Kruszelnicki, and R. Dabrowski, *Tunable highly birefringent solid-core photonic liquid crystal fibers*, Opt. Quantum Electron. **39**, 10211032 (2007).

[59] T. A. Birks, J. C. Knight, and P. S. J. Russell, *Endlessly single-mode photonic crystal fiber*, Opt. Lett. **22**, 961 (1997).

[60] R. K. Sinha and S. K. Varshney, *Dispersion properties of photonic crystal fibers*, Microw. Opt. Technol. Lett. **37**, 129 (2003).

[61] J. E. Sharping, M. Fiorentino, P. Kumar, and R. S. Windeler, *Optical parametric oscillator based on four-wave mixing in microstructure fiber*, Opt. Lett. **21**, 1675 (2002).

[62] M. Lehtonen, *Applications of microstructured fibers*, Ph.D. thesis, Helsinki University of Technology, Department of Electrical and Communications Engineering, Finland (2005).

[63] G. Genty, *Supercontinuum generation in microstructured fibers and novel optical measurement techniques*, Ph.D. thesis, Helsinki University of Technology, Department of Electrical and Communications Engineering, Finland (2004).

[64] M. D. Nielsen, C. Jacobsen, N. A. Mortensen, J. R. Folkenberg, and H. R. Simonsen, *Low-loss photonic crystal fibers for transmission systems and their dispersion properties*, Opt. Express **12**, 1372 (2004).

[65] T. Ritari, T. Niemi, H. Ludvigsen, M. Wegmuller, N. Gisin, J. R. Folkenberg, and A. Pettersson, *Polarization-mode dispersion of large mode-area photonic crystal fibers*, Opt. Commun. **226**, 233 (2003).

[66] J. Limpert, T. Schreiber, S. Nolte, H. Zellmer, A. Tnnermann, R. Iliew, F. Lederer, J. Broeng, G. Vienne, A. Pettersson, *et al.*, *High-power air-clad large-mode-area photonic crystal fiber laser*, Opt. Express **11**, 818 (2003).

[67] A. Bjarklev, J. Broeng, and A. S. Bjarklev, *Photonic Crystal Fibres* (Kluwer Academic Publishers, 2003), 1st ed.

[68] M. D. Nielsen, N. A. Mortensen, M. Albertsen, J. R. Folkenberg, A. Bjarklev, and D. Bonacinni, *Predicting macrobending loss for large-mode area photonic crystal fibers*, Opt. Express **12**, 1775 (2004).

[69] M. D. Nielsen, G. Vienne, J. R. Folkenberg, and A. Bjarklev, *Investigation of microdeformation induced attenuation spectra in a photonic crystal fibers*, Opt. Lett. **28**, 236 (2003).

[70] M. Koshiba and K. Saitoh, *Structural dependence of effective area and mode field diameter for holey fibers*, Opt. Express **11**, 1746 (2003).

[71] K. N. Park, T. Erdogan, and K. S. Lee, *Cladding mode coupling in long-period gratings formed in photonic crystal fibers*, Opt. Commun. **266**, 541 (2006).

[72] T. M. Monro, D. J. Richardson, N. Broderick, and P. J. Bennett, *Holey optical fibers: An efficient modal model*, J. Lightwave Technol. **17**, 1093 (1999).

[73] J. Arriaga, J. Knight, and P. J. Russell, *Modeling the propagation of light in photonic crystal fibers*, Physica D **189**, 100 (2004).

[74] B. T. Kuhlmey, T. P. White, G. Renversez, D. Maystre, L. C. Botten, C. M. de Sterke, and R. C. McPhedran, *Multipole method for microstructured optical fibers. II. implementation and results*, J. Opt. Soc. Am. B **19**, 2331 (2002).

[75] M. Koshiba, S. Maruyama, and K. Hirayama, *A vector finite element method with the high-order mixed-interpolation-type triangular elements for optical waveguiding problems*, J. Lightwave Technol. **12**, 495 (1994).

[76] A. Ortega-Monux, J. G. Wanguemert-Pérez, and I. Molina-Fernández, *Accurate analysis of photonic crystal fibers by means of the fast-fourier-based mode solver*, IEEE Photonics Technol. Lett. **19**, 414 (2007).

[77] A. Ortega-Monux, J. G. Wanguemert-Pérez, I. Molina-Fernández, E. Silvestre, and P. Andres, *Enhanced accuracy in fast-fourier-based methods for full-vector modal analysis of dielectric waveguides*, IEEE Photonics Technol. Lett. **18**, 1128 (2006).

[78] M. Szpulak, W. Urbanczyk, E. Serebryannikov, A. Zheltikov, A. Hochman, Y. Leviatan, R. Kotynski, and K. Panajotov, *Comparison of different methods for rigorous modeling of photonic crystal fibers*, Opt. Express **14**, 5699 (2006).

[79] M. J. Steel, T. P. White, C. M. de Sterke, R. C. McPhedran, and L. C. Botten, *Symmetry and degeneracy in microstructured optical fibers*, Opt. Lett. **26**, 488 (2001).

[80] M. Zacarés, *Métodos modales para el análisis de la propagación no lineal en fibras ópticas*, Ph.D. thesis, Universidad de Valencia (2005).

[81] A. Ferrando, M. Zacarés, P. F. de Córdoba, D. Binosi, and J. Monsoriu, *Spatial soliton formation in photonic crystal fibers*, Opt. Express **11**, 452 (2003).

[82] A. Ferrando, M. Zacarés, P. F. de Córdoba, D. Binosi, and J. Monsoriu, *Vortex solitons in photonic crystal fibers*, Opt. Express **5**, 817 (2004).

[83] F. Drouard, *Kerr Nonlinearity in Microstructured Optical Fibers*, Ph.D. thesis, Institut Fresnel CNRS, Marseille (2008).

[84] D. Lee, Y. Jung, Y. S. Jeong, K. Oh, J. Kobelke, K. Schuster, and J. Kirchhof, *Highly polarization-dependence periodic coupling mechanically induced long period grating over airsilica fiber*, Opt. Lett. **31**, 296 (2006).

[85] D. E. Ceballos-Herrera, I. Torres-Gómez, A. Martínez-Rios, G. Anzueto-Sánchez, R. S.-A. J. A. Álvarez-Chávez, and J. J. Sánchez-Mondragón, *Ultra-widely tunable long-period holey-fiber grating by the use of mechanical pressure*, Appl. Opt. **46**, 307 (2007).

[86] J. H. Lim, K. S. Lee, J. C. Kim, and B. H. Lee, *Gain flattened and improved edfa using microbending long-period fibre gratings*, Electron. Lett. **38**, 1324 (2002).

[87] K. Morishita and Y. Miyake, *Fabrication and resonance wavelengths of long-period gratings written in a pure-silica photonic crystal fiber by the glass structure change*, J. Lightwave Technol. **22**, 625 (2004).

[88] R. Guobin, W. Zhi, L. Shuqin, and J. Shuisheng, *Full-vectorial analysis of complex refractive index photonic crystal fibers*, Opt. Express **11**, 1310 (2003).

[89] S. D. Lim, H. C. Park, I. K. Hwang, and B. Y. Kim, *Combined effects of optical and acoustic birefringence on acousto-optic mode coupling in photonic crystal fiber*, Opt. Express **16**, 6125 (2008).

[90] N. A. Mortensen, M. D. Nielsen, J. R. Folkenberg, K. P. Hansen, and J. Laegsgaard, *Small-core photonic crystal fibres with weakly disordered air-hole claddings*, J. Opt. A: Pure Appl. Opt. **6**, 221 (2004).

[91] I. Torres-Gómez, A. Martínez-Rios, D. E. Ceballos-Herrera, E. Mejía-Beltrán, and R. Selvas-Aguilar, *Bandpass filter with adjustable bandwidth based on a press-induced long-period twisted holey-fiber grating*, Opt. Lett. **32**, 3385 (2007).

[92] D. E. Ceballos-Herrera, I. Torres-Gómez, A. Martínez-Rios, and J. J. Sanchez-Mondragón, *Torsion sensing characteristics of mechanically induced long period holey fiber gratings*, submitted to IEEE Sens. J. (2009).

[93] O. Ivanov, *Wavelength shift and split of cladding mode resonances in microbend long-period fiber gratings under torsion*, Opt. Commun. **232**, 159 (2004).

[94] O. V. Ivanov, *Propagation and coupling of hybrid modes in twisted fibers*, J. Opt. Soc. Am. A **29**, 716 (2005).

[95] Z. Zhang, W. Shi, R. Gao, and Z. Fang, *Twist characteristics of the ultraviolet-written long-period fiber gratings*, Chin. Opt. Lett. **2**, 565 (2005).

[96] C. Chung and H. Lee, *The resonance wavelength-tuning characteristic of the arc-induced LPFGs by diameter modulation*, in Proc. OFS p. 131 (2002).

[97] B. U. Nair, V. P. S. Kumar, V. P. M. Pillai, and V. U. Nayar, *Wavelength shift of cladding mode resonances in a mechanically induced LPFG by twisting the fiber*, Fiber Integrated Opt. **26**, 159 (2007).

[98] C. Lin, L. Wang, and G. Chern, *Corrugated long-period fiber gratings as strain, torsion, and bending sensors*, J. Lightwave Technol. **19**, 1159 (2001).

[99] J. Yong and K. Lee, *A birefringence compensation method for mechanically induced long-period fiber gratings*, Opt. Commun. **213**, 281 (2002).

[100] O. Deparis, R. Kiyan, O. Pottiez, M. Blondel, I. G. Korolev, S. A. Vasiliev, and E. M. Dianov, *Bandpass filters based on π-shifted long-period fiber gratings for actively mode-locked erbium fiber lasers*, Opt. Lett. **26**, 1239 (2001).

[101] D. S. Starodubov, V. Grubsky, and J. Feinberg, *All-fiber bandpass filter with adjustable transmission using cladding-mode coupling*, IEEE Photon. Technol. Lett. **10**, 1590 (1998).

[102] S. Choi, T. J. Eom, Y. Jung, B. H. Lee, J. W. Lee, and K. Oh, *Broad-band tunable all-fiber bandpass filter based on hollow optical fiber and long-period grating pair*, IEEE Photon. Technol. Lett. **17**, 115 (2005).

[103] S. Suzuki, H. Ito, Y. Takata, and H. Sakata, *Cladding-mode extraction from long-period fibre grating using self-aligned core-mode blocker*, Electron. Lett. **43**, 330 (2007).

[104] Y. Zhu, P. Shum, H. W. Bay, X. Chen, C. H. Tan, and C. Lu, *Wide-passband, temperature-insensitive, and compact* π*-phase-shifted long-period gratings in endlessly single-mode photonic crystal fiber*, Opt. Lett. **29**, 2608 (2004).

[105] C. Y. Lin, L. A. Wang, and G. W. Chern, *Corrugated long-period fiber gratings as strain, torsion, and bending sensors*, J. Lightwave Technol. **19**, 1159 (2001).

[106] Y. P. Wang, J. P. Chen, and Y. J. Rao, *Torsion characteristics of long-period fiber gratings induced by high-frequency* CO_2 *laser pulses*, J. Opt. Soc. Am. B **22**, 1167 (2005).

[107] J. Nilsson, W. A. Clarkson, R. Selvas, J. K. Sahu, P. W. Turner, S. U. Alam, and A. B. Grudini, *High-power wavelength-tunable cladding-pumped rare-earth-doped silica fiber lasers*, Opt. Fiber Technol. **10**, 5 (2004).

[108] M. Auerbach, P. Adel, D. Wandt, C. Fallnich, S. Unger, S. Jetschke, and H. R. Muller, *10 W widely tunable narrow linewidth double-clad fiber ring laser*, Opt. Express **10**, 139 (2002).

[109] X. Feng, L. Sun, L. Xiong, Y. Liu, S. Yuan, G. Kai, and X. Dong, *Switchable and tunable dual-wavelength erbium-doped fiber laser based on one fiber bragg grating*, Opt. Fiber Technol. **10**, 275 (2004).

[110] A. Gloag, N. Langford, K. Mccallion, and W. Johnstone, *Tunable erbium fiber laser using a novel overlay bandpass filter*, Opt. Lett. **19**, 801 (1994).

[111] A. Vengsarkar, J. R. Pedrazzani, J. B. Judkins, P. J. Lemaire, N. S. Bergano, and C. R. Davidson, *Long-period fiber-grating-based gain equalizers*, Opt. Lett. **21**, 336 (1996).

[112] P. L. Swart, T. J. Nhlapo, and A. A. Chtcherbakov, *Long-period grating filter with tunable attenuation for spectral equalization of erbium-doped fiber broadband light sources*, Opt. Eng. **43**, 280 (2004).

[113] S. Savin, M. Digonet, G. Kino, and H. Shaw, *Tunable mechanically induced long-period fiber gratings*, Opt. Lett. **25**, 710 (2000).

[114] G. Rego, J. Fernandez, J. L. Santos, H. M. Salgado, and P. Marques, *New technique to mechanically induce long-period fibre gratings*, Opt. Commun. **220**, 111 (2003).

[115] T. Yokouchi, Y. Suzaki, K. Nakagawa, M. Yamauchi, M. Kimura, Y. Mizutani, S. Kimura, and S. Ejima, *Thermal tuning of mechanically induced long-period fiber grating*, Appl. Opt. **44**, 5024 (2005).

[116] G. Sun, Y. chung, and D. S. Moon, *L-band tunable multiwavelength fiber laser using an unpumped polarization maintaining and erbium-ytterbium double-clad fiber-loop mirror*, Laser Physics **18**, 1196 (2008).

[117] H. Ahmad, A. H. Sulaiman, S. Shahi, and S. Harun, *SOA-based multi-wavelength laser using fiber bragg gratings*, Laser Physics **19**, 1002 (2009).

[118] X. Liu, X. Yang, F. Lu, J. Nang, and X. Zhou, *Stable and uniform dual-wavelength erbium-doped fiber laser based on fiber bragg gratings and photonic crystal fibers*, Opt. Express **13**, 142 (2005).

[119] M. P. Fok and C. Shu, *Spacing-adjustable multi-wavelength source from a stimulated brillouin scattering assisted erbium-doped fiber laser*, Opt. Express **14**, 2618 (2006).

[120] M. N. M. Nasir, M. H. Al-Mansoori, H. A. A. Rashid, P. K. Choudhury, and Z. Yusoff, *Multi-wavelength brillouin-erbium fiber laser incorporating a fiber bragg grating filter*, Laser Phys. **18**, 446 (2008).

[121] H. Wang, Y. G. Li, X. D. Chen, B. Huang, F. Y. Lu, and K. C. Lu, *Highly efficient dual-wavelength ytterbium-doped fiber linear cavity laser based on cascaded fiber bragg gratings*, Laser Phys. **19**, 1257 (2009).

[122] A.-P. Luo, Z.-C. Luo, and W.-C. Xu, *Multi-wavelength erbium-doped fiber ring laser based on wavelength-dependent polarization rotation with a phase modulator and an in-line comb filter*, Laser Phys. **19**, 1034 (2009).

[123] T. Chartier, A. Mihaescu, G. Martel, A. Hideur, and F. Sanchez, *Multi-wavelength fiber laser with an intracavity polarizer*, Opt. Comm. **256**, 98 (2005).

[124] P. Peterka, J. Maria, B. Dussardier, R. Slavik, P. Honzatko, and V. Kubecek, *Long-period fiber grating as wavelength selective element in double-clad yb-doped fiber-ring lasers*, Laser Phys. Lett. **6**, 732 (2009).

[125] C. D. Su and L. A. Wang, *Multi-wavelength fiber sources based on double-pass superfluorescent fiber sources*, J. Lightwave Technol. **18**, 708 (2000).

[126] Y.-G. Han, C.-S. Kim, J. U. Kang, U.-C. Paek, and Y. Cheng, *Multi-wavelength raman fiber-ring laser based on tunable cascaded long-period fiber gratings*, IEEE Phot. Technol. Lett. **15**, 383 (2003).

[127] M. A. van Eijkelenborg, W. Padden, and J. A. Besley, *Mechanically induced long-period gratings in microstructured polymer fibre*, Opt. Commun. **236**, 75 (2004).

[128] I. Torres-Gómez, A. Martínez-Rios, D. E. Ceballos-Herrera, E. Mejía-Beltrán, and R. Selvas-Aguilar, *Bandpass filter with adjustable bandwidth based on press induced long period twisted holey fiber grating*, Opt. Lett. **33**, 3385 (2007).